Title
A Transdimensional Inversion Method for Multi-mode Surface Waves and Its Application to Antarctica and Mars

Author
Xu, Haotian

Publication Date
2021

Peer reviewed|Thesis/dissertation

UNIVERSITY OF CALIFORNIA
Los Angeles

A Transdimensional Inversion Method for Multi-mode Surface Waves and Its Application to Antarctica and Mars

A dissertation submitted in partial satisfaction
of the requirements for the degree
Doctor of Philosophy in Earth, Planetary and Space Sciences

by

Haotian Xu

2021

ABSTRACT OF THE DISSERTATION

A Transdimensional Inversion Method for Multi-mode Surface Waves
and Its Application to Antarctica and Mars

by

Haotian Xu
Doctor of Philosophy in Earth, Planetary and Space Sciences
University of California, Los Angeles, 2021
Professor Caroline Beghein, Chair

The study of seismic surface waves provides important constraints on the Earth interior and potentially other celestial objects. In this thesis, we present a novel hierarchical transdimensional Bayesian approach to extract phase velocity dispersion and shear-wave velocity (V_S) models from a single seismogram. Monte Carlo Markov Chains (MCMC) seek an ensemble of one dimensional (1-D) V_S models between a seismic source and a receiver that can explain the observed waveform. The models obtained are used to represent the posterior V_S distribution of the 1-D path, which can then be used to invert for three dimensional (3-D) models. An advantage of our approach is that it can also fit unknown data noise, which reduces the risk of overfitting the data in the seismic inversion problem. A 3-D azimuthally anisotropic V_S model is obtained by applying the proposed method to Antarctica. The results show distinct patterns between East Antarctica and West Antarctica in both isotropic and anisotropic terms. We also demonstrate the feasibility to apply our method to Mars using the Mars Structure Service (MSS) blind test data and our own synthetic data, which included realistic noise levels based on the noise recorded by InSight.

The dissertation of Haotian Xu is approved.

Seulgi Moon

Lingsen Meng

Paul Davis

Caroline Beghein, Committee Chair

University of California, Los Angeles

2021

To my family ...

TABLE OF CONTENTS

1 Introduction **1**

2 Methodology **3**

2.1 Overview of Previous Higher Modes Surface Wave Studies 3

2.2 1-D Waveform Modeling 6

2.3 Selection of Frequency-Time Windows 8

2.4 Bayesian Inference 11

2.5 The rj-MCMC method 14

2.6 MCMC Sampling Steps and Parametrization 17

2.7 Reliability Analysis 19

2.8 Synthetic Test 21

2.9 Real Data Test 35

2.10 Summary 44

3 Antarctica **49**

3.1 Introduction 49

3.2 Data Selection 54

3.3 Method 55

3.3.1 MCMC Inversion Scheme and Waveform Fitting 57

3.3.2 Phase Velocity Maps and Inversion of 1-D Path-Averaged Models . . 60

3.4 Results 63

3.4.1 1-D Path-Averaged Profiles 63

3.4.2 Significance of the Anisotropy 65
3.4.3 Isotropic Model 67
3.4.4 Azimuthal Anisotropy 74
3.4.5 Synthetic Tests 75
3.4.6 Phase Velocity Maps 77
3.5 Discussion 80
3.6 Conclusion 87

4 Mars (InSight) 90
4.1 Introduction 90
4.2 Method 94
4.2.1 Waveform Modeling 94
4.2.2 Source Parameter and Cycle Skipping Considerations 95
4.2.3 Misfit Function 97
4.2.4 Bayesian Inference 98
4.2.5 rj-MCMC Inversion Scheme 99
4.3 Tests and Results 100
4.3.1 Blind Test 101
4.3.2 Waveform Modeling: Effects of the Source Parameters 102
4.3.3 Effects of Reference Crustal Thickness 107
4.3.4 Effect of Envelopes and Group Velocities 111
4.4 Additional Synthetic Test with Realistic Martian Noise 113
4.4.1 Results and Reliability Analysis 116
4.5 Conclusions 122

5 Summary and Conclusion 124

LIST OF FIGURES

2.1 Comparison between synthetic seismograms calculated with normal mode summation using Mineos without linearization (blue) and with our linearized method (red) in three different period ranges: 100 s-200 s (top), 50 s-100 s (middle), and 30 s-50 s (bottom). The shear-velocity model used to compute the seismograms is shown in Figure 2.3. 9

2.2 An example of our automatic time window selection for a path across North America. The waveform is for the observed data. The station, HRV, is located in northeastern America. The event was in Chiapas, Mexico and occurred on 6 July, 2007. The time window in the upper panel is window 1 as defined in Table 2.1. The time window on the right side of the lower panel is for the fundamental mode (window 2) and the time window on the left of the lower panel is the higher modes window (window 3). 10

2.3 Example of model parametrization. The red squares denote the points at which the velocity model is perturbed. The complete dV_S profile is obtained by linear interpolation between those points. 18

2.4 (A) Color density plot representing the ensemble of solutions obtained by inversion of the synthetic seismogram that was calculated with the input model shown in (B); The posterior mean model resulting from this distribution of solutions is also displayed in (B) 23

2.5 (A) Posterior distribution for the number of parameters in the synthetic test of Figure 2.4; (B) Posterior distribution for the data noise level for each of the three time windows considered. 24

2.6 Comparison between input synthetic waveform and the waveform predicted by PREM (top) and by the mean model resulting from our inversion (bottom). The seismograms shown here represent the velocity of the ground motion. The input seismogram was calculated for the true model shown in Figure 2.4. Two frequency bands, as indicated in table 2.1, are considered separately. The waveforms match is much improved after inversion. 25

2.7 (A) Comparison between the output and input synthetic data in the time domain filtered in the 50s-200s period range; (B): Spectrogram of the waveform fit f(ω, t), as defined in equation 2.18. The regions with warmer colors correspond to better waveform fit in the F-T domain. 26

2.8 Inverted fundamental mode (A) and first overtone (B) phase velocity dispersion and uncertainties (blue) compared to the dispersion curve calculated for the true model (red). The uncertainties shown here correspond to 2σ obtained from the posterior distribution. 27

2.9 (A) Synthetic waveform of the first overtone calculated from the inverted 1-D Vs profile and filtered in the 50s-200s period range; (B): Spectrogram $P_1(\omega, t)$ of the relative weight of the first overtone in the synthetic test, as defined in equation 2.19. The regions with warmer colors in the figure represent larger weights in the F-T domain. 28

2.10 Reliability parameters as a function of frequency for the fundamental mode (n=0) and the first five overtones in the synthetic test. The thresholds we defined for each mode are denoted by the red dashed lines. Only periods at which the reliability parameters are above the threshold are kept as reliable inversion results. 29

2.11 (A) V_S posterior distribution for a synthetic test with uncorrelated noise. Both noise levels and model dimensions are variable during the inversion. The red line in panel (B) is the true model. The grey curve is the mean of the distribution of panel (A). Panel (C) represents the inverted fundamental mode (top) and first overtone (bottom) phase velocity dispersion curves and uncertainties (blue) compared to the dispersion curve calculated for the true model (red). The uncertainties shown here correspond to two standard deviation obtained from the posterior distribution. 31

2.12 V_S posterior distribution (A) for the a synthetic test with uncorrelated noise and fixed depth parametrization. We fixed the number of depth nodes to nine and we fixed their depths at 5 km, 20 km, 80 km, 140 km, 210 km, 310 km, 430 km, 550 km and 690 km. Only the noise level and amplitude of dV_S/V_S are allowed to vary during the inversion. The red line in panel (B) is the true model and the grey curve is the mean of the distribution of panel (A). Panel (C) represents the inverted fundamental mode (top) and first overtone (bottom) phase velocity dispersion curves and uncertainties (blue) compared to the dispersion curve calculated for the true model (red). The uncertainties shown here correspond to two standard deviation obtained from the posterior distribution. 32

2.13 (A) V_S posterior distribution for the a synthetic test with fixed, uncorrelated and underestimated noise and fixed depth parametrization. The transdismentionality of the algorithm was turned off and the depths of the nodes were the same as in Fig. 2.12. We assumed the fixed noise level was underestimated in the inversion by a factor 100 compared to the synthetic input data noise level. Only the amplitude of dV_S/V_S was allowed to vary during the inversion. The red line in panel (B) is the true model and the grey curve is the mean of the distribution of panel (A). Panel (C) represents the inverted fundamental mode (top) and first overtone (bottom) phase velocity dispersion curves and uncertainties (blue) compared to the dispersion curve calculated for the true model (red). The uncertainties shown here correspond to two standard deviation obtained from the posterior distribution. 33

2.14 (A) V_S posterior distribution for the a synthetic test with fixed, uncorrelated and overestimated noise and fixed depth parametrization. The transdismentionality of the algorithm was turned off and the depths of the nodes were the same as in Fig. 2.12. We assumed the fixed noise level was overestimated in the inversion by a factor 10 compared to the synthetic input data noise level. Only the amplitude of dV_S/V_S was allowed to vary during the inversion. The red line in panel (B) is the true model and the grey curve is the mean of the distribution of panel (A). Panel (C) represents the inverted fundamental mode (top) and first overtone (bottom) phase velocity dispersion curves and uncertainties (blue) compared to the dispersion curve calculated for the true model (red). The uncertainties shown here correspond to two standard deviation obtained from the posterior distribution. 34

2.15 Locations of events (stars) and stations (triangles) used for the real data test. The yellow lines show the great circle paths from sources to receivers for western and eastern Australia. 36

2.16 (A) Posterior distribution of relative velocity perturbations with respect to Debayle et al. [2016] for the western Australia path; (B) Resulting mean dV_S/V_S model 37

2.17 (A) Posterior distribution of the number of velocity parameters for the western Australia path; (B) Posterior data error distribution for each of the three time windows. Note the different scales on the horizontal axes. 38

2.18 The same as Figure 2.7 but for the western Australia path. (A) Real data and synthetic seismogram filtered in the 50 s-200 s period range and calculated using the inverted mean model of Figure 2.16; (B) F-T analysis of the misfit as defined in equation 2.18. 39

2.19 Reliability parameters for the western Australia path. See Figure 2.10 for details. 40

2.20 Measured phase velocities anomalies for the western Australia path and the modes and periods that were estimated to be reliable (Fig. 2.19). The measurements were converted from perturbations with respect to the average version of the 3-D reference model into perturbations with respect to PREM. Uncertainties correspond to 2σ. 41

2.21 Posterior ensemble of solutions for the eastern Australia path. See Fig. 2.4 for details. 42

2.22 (A) Posterior ensemble for the number of parameters for the eastern Australia path; (B) Posterior noise distribution for each the the three time windows. Note the different horizontal scales. 42

2.23 Real data and synthetic seismogram filtered in the 50 s-200 s period range and calculated using the inverted mean model of Figure 2.21 (top); F-T analysis of the misfit as defined in equation 2.18 (bottom). 43

2.24 Reliabiliy test for the eastern Australia path. See Fig. 2.10 for details 44

2.25 Reliable measured phase velocities expressed as perturbations with respect to PREM for the eastern Australia path and the modes and periods that were estimated to be reliable (Fig. 2.24). The red curve represents measurements performed using the model of Debayle et al. [2016] as a reference model. The blue curve are measurements performed using model S40RTS of Ritsema et al. [2011] as reference. The phase velocities were converted from perturbations with respect to the 3-D reference model into perturbations with respect to PREM. Uncertainties correspond to 2σ. 45

2.26 The mean V_S solution and one standard deviation for the western (A) and Eastern (B) Australia paths compared to PREM. 46

3.1 Topographic map of Antarctica. The bathymetry and topography of Antarctica and surrounding areas are based on model SRTM15+ [Tozer et al., 2019]. Abbreviations: AP = Antarctica Peninsula; DML = Dronning Maud Land; EMW = Ellsworth Whitmore Mountains; GSM = Gamburtsev Subglacial Mountains; LG = Lambert Graben; MBL = Marie Byrd Land; WARS = West Antarctic rift system. 50

3.2 Maps of selected event locations (red circles) and stations (blue triangles). The background bathymetry and topography of Antarctica and surrounding areas are based on model SRTM15+ [Tozer et al., 2019]. 56

3.3 Ray-path coverage (red curves) and the 2-D triangular grid (black circles) used in the V_S modeling. 62

3.4 Ray-path coverage of all event-station pairs which pass all quality control steps. 64

3.5 The distribution of path-specific V_{SV} standard deviations at different depths. All paths shown in Fig. 3.4 are included to estimate the distribution and the standard deviation for each path is calculated from the ensemble of V_{SV} models sampled in the MCMC step. 66

3.6 An example of damping parameter selection based on the L-curve method. The L-curves illustrate the trade-offs between the variance reduction (y-axis) and the amount of damping added (x-axis). The optimal damping parameters are selected as the elbow points (orange triangles) of the curves. We first searched for the damping parameters of isotropic terms, and then based on the selected damping parameters for isotropic terms, we further searched for the 2Ψ terms, and finally the 4Ψ terms. 68

3.7 An example of reduced χ^2 as a function of the trace of resolution matrix $\mathbf{R}$ for inversions of Vs at depth 150 km. The blue curve is for cases where only the isotropic terms are included in the inversion. Different values of the trace of resolution matrix were obtained by applying different levels of damping. The preferred model selected by the L-curve method is marked as red star. The orange curve represents the inversion with both isotropic and 2Ψ anisotropic terms, and the damping parameters for the isotropic terms were fixed at the preferred values. The green curve is further based on the orange curve, with isotropic, 2Ψ and 4Ψ terms all included in the inversion. The red triangle and red square correspond to the preferred models in the isotropic + 2Ψ and isotropic + 2Ψ + 4Ψ inversions, respectively. 69

3.8 Isotropic part of our 3-D V_{SV} model at different depths. Velocity perturbations are calculated relative to PREM. 71

3.9 Vertical slices of the 3-D model. V_{SV} structure along transects A-A'(a), B-B'(b) and C-C'(c). Profile locations are marked in the upper-left map. Abbreviations: AP = Antarctica Peninsula; DML = Dronning Maud Land; GSM = Gamburtsev Subglacial Mountains; MBL = Marie Byrd Land; TAMs = Transantarctic Mountains; VL = Victoria Land. 73

3.10 2Ψ anisotropy at different depths (black bars). The background color represents the isotropic part of the model. Directions of black bars represent the fast directions and the length of black bars are proportional to the amplitude of the anisotropy.The purple arrows represent the APMs based on NUVEL-1A with no-net rotation reference frames [Gripp and Gordon, 2002]. The red line at bottom represents the Pacific-Antarctic Ridge. 76

3.11 Synthetic tests at 150 km depth. Isotropic checkerboard test (top): (A) is the input V_{SV} model and (B) is the recovered isotropic model. The middle panels are for an anisotropic inversion with an isotropic input model (C). The recovered output model with 2Ψ terms included in the inversion is shown in (D). The bottom panels are for an anisotropic resolution test. (E) is the input model and (F) is the recovered model. The length of black bars represents the amplitudes of the anisotropy. 78

3.12 Horizontal cross sections of the 2Ψ anisotropic terms (black bars) for phase velocities at selected modes and periods.. Directions of black bars represent the fast directions and the length of black bars are proportional to the anisotropic strengths. 81

3.13 Topographic map of the Antarctic plate LAB depth calculated using the middle point of the interval over which V_S decreases in the isotropic model. 82

3.14 Comparison of observed (red) and predicted (blue) SKS splitting measurements for Antarctica. The red bar and red circle in EANT roughly describe the SKS measurements and seismic station distribution of AGAP network [Hernandez et al., 2009]. Lengths of the bars are proportional to the SKS splitting delayed time while the directions represent fast directions. Abbreviations: AP = Antarctica Peninsula; DML = Dronning Maud Land; EMW = Ellsworth Whitmore Mountains; GSM = Gamburtsev Subglacial Mountains; LG = Lambert Graben; MBL = Marie Byrd Land; WARS = West Antarctic rift system. 86

4.1 Sensitivity kernels $\partial \ln c / \partial V_s$ at different periods for fundamental mode surface waves (left), the first overtone (middle), and the second overtone (right) at periods between 5s and 200s. They were calculated using software package Mineos [Masters et al., 2011]. The model of Zheng et al. [2015] with no low velocity zone was used as reference. 92

4.2 Comparison of the MSS blind test waveform (A) and synthetic waveforms predicted by three different reference models: (B) model LVZ by Zheng et al. [2015], which included a low velocity zone; (C) model noLVZ by Zheng et al. [2015] without Low Velocity Zone; (D) Sohl and Spohn [1997]'s model A. All traces were bandpass-filtered between 25 s and 50 s. 103

4.3 Inversion results with fixed source parameters (left) and free source parameters (right). The gray dashed line represents the reference model used for MCMC sampling and partial derivative calculations. The red line is the 1-D base model used to compute the blind test data. The gray shaded area is for the maximum and minimum V_S and Moho depth along the source-receiver path based on the 3-D crust model used to generate the blind test data. The color scale represents the likelihood of a given model parameter. 104

4.4 Posterior distributions of Moho depth in the fixed-source test (left) and in the free-source test (right). The dark blue dashed lines represent the Moho depth in the 1-D base model used to generate the MSS blind test data. The light blue dotted line represents one of the best fitting values. 105

4.5 Waveform fitting misfits as a function of iteration number for free source MCMC sampling (top) v.s. fixed source MCMC sampling (bottom). 107

4.6 Posterior distributions of strike, dip, slip, and focal depth (red shaded area) for the inversion with free source parameters shown in the right panel of Fig. 4.3. The prior distributions used for each of those parameters are represented by the shaded grey areas. The true values used to generate the MSS blind test data are shown by the dark blue dashed lines, including the strike, dip and slip for both planes calculated from the true source moment tensor. The best fitting parameters obtained by the MCMC sampling are indicated by the dotted line. . 108

4.7 Ensemble of models resulting from inversions with waveform envelopes and starting models of different crustal thickness: 50 km (left) and 75 km(right). The color scale and different curves are described in Fig. 4.3. 110

4.8 Best fitting waveforms for the test with Moho depth at 50 km 111

4.9 Ensemble of models resulting from inversions with group velocities and starting models of different crustal thickness: 50 km (left) and 75 km(right). The color scale and different curves are described in Fig. 4.3 112

4.10 Measured phase velocity dispersion curves for the fundamental mode Rayleigh wave with two standard deviations obtained from the posterior distributions, and dispersion curve for the 1-D base model (purple dashed curve) used in the blind test. M50 and M75 represents the inversions with Moho depth at 50 km and 75 km, respectively. 'Env' stands for envelope and 'Grv' stands for group velocity. 114

4.11 Probabilistic power spectral density (PPSD) measured during the "quiet" time (less windy) on Mars (18:00 – 23:00 LMST) in July 2019. The dashed lines mark the 10th and 90th percentiles. The PPSD was calculated using the method of McNamara and Buland [2004]. 115

4.12 Vertical component waveform calculated using Zheng et al. [2015]'s model noLVZ and filtered at 25 s - 50 s. Realistic Martian noise was added to the synthetic waveform (thick black line) 116

4.13 Ensemble of V_S solutions obtained from the MCMC sampling. The thin black dashed line represents the true model and the thick white line is for the starting model. The color scale represents the likelihood of a given model parameter. . . 118

4.14 Reliability scores for the fundamental mode (n = 0) and first 3 overtones (n = 1, 2, or 3) as a function of periods. The horizontal red dashed lines indicate the empirical thresholds we defined for each mode. Only periods with reliability scores higher than the thresholds will be kept. 119

4.15 Measured phase velocity dispersion curves for the fundamental mode Rayleigh wave (n = 0) and the first 3 overtones (n = 1, 2, 3) with two standard deviations as error bars. The dispersion curves from the 1-D true model (dashed curve) were plotted for comparison. 120

4.16 Similar as Fig. 4.6 but is for the synthetic test. (Red) The posterior distributions of strike, dip, slip, focal depth as well as Moho depth. The prior distributions used for each of those parameters are represented by the shaded grey areas. The true values used to generate the synthetic waveform are shown by the blue dashed lines. 121

LIST OF TABLES

2.1 Selection of frequency-time windows. The first and second window indices correspond to the fundamental mode and the third window is for higher modes. The start and end times for the fundamental mode are determined by the group velocities U indicated in the table and the event epicentral distance Δ. For the higher modes, the beginning of the time window is determined by the S- or SS-wave arrival times. The end of the window is determined by Δ/U. 11

2.2 Source parameters from GCMT Catalog. Event 200503021042A was used for the synthetic test. 200910151211A was for the western Australia path and 201004172315A for the eastern Australia path. 22

3.1 Selection of frequency-time windows. The first and second window indices correspond to the fundamental mode and the third window is for higher modes. The first and third windows share the same start time, which is determined by the S- or SS- wave arrival times. All other start/end times are determined by Δ/U, where Δ is the event epicentral distance and the values of the group velocities U are indicated in the table. 65

3.2 Significance of 2Ψ and 4Ψ terms at different depths from F-test analysis. A lower probability means that the model with more parameters has significantly lower misfits compared to the model with fewer parameters, and thus those extra parameters are needed to explain the data. 70

3.3 Significance of 2Ψ terms in the phase velocity map modeling for different modes and periods using a F-test analysis. A lower probability means that the model with more parameters has significantly lower misfits compared to the model with fewer parameters, and thus those extra parameters, i.e. anisotropy, are needed to explain the data. 79

4.1 Comparison between MQS-estimated and true source parameters. 102

4.2 Prior (uniform) distributions of source parameters used for the rj-MCMC sampling. 105

ACKNOWLEDGMENTS

First of all, I would like to express my deep sense of thanks and gratitude to my Ph.D advisor, Dr. Caroline Beghein, for her continuous support of my Ph.D work, for her encouragement and motivation, and for her timely guidance.

I also want to thank my thesis committee members: Prof. Paul Davis, Prof. Lingsen Meng, and Prof. Seulgi Moon, for their insightful comments and helpful suggestions on my research.

I want to thank my past labmate and roommate, Dr. Zheng Xing, for his kind help during my early years at UCLA.

I want to thank my past and current colleagues, including Erik Weidner, Jiaqi Li, Ailin Zhang, Hui Huang, Tian Feng, Yuqing Xie and Han Bao, for the interesting discussions and happy moments we had in the past six years.

Last but not least, I would like to thank my family for their moral support throughout my life.

VITA

2011–2015 B.S. (Geophysics), University of Science and Technology of China (USTC), Hefei, China

2015–2017 M.S. (Geophysics), University of California, Los Angeles (UCLA)

PUBLICATIONS

Xu, H., Beghein, C., Panning, M.P., Drilleau, M., Lognonné, P., van Driel, M., Ceylan, S., Böse, M., Brinkman, N., Clinton, J., Euchner, F., Giardini, D., Horleston, A., Kawamura, T., Kenda, B., Murdoch, N., and Stähler, S. (2020), Measuring Fundamental and Higher Mode Surface Wave Dispersion on Mars From Seismic Waveforms, Earth and Space Science, 8, e2020EA001263, doi:10.1029/2020EA001263

Drilleau, M., Beucler, E., Lognonné,P., Panning, M.P., Knapmeyer-Endrun, B. Banerdt, W.B., Beghein, C., Ceylan, S., van Driel, M., Joshi, R., Kawamura,T., Khan, A., Menina, S., Rivoldini, A., Samuel, H., Stahler, S., Xu, H., Bonnin, M., Clinton, J., Giardini, D., Kenda, B., Lekic, V., Mocquet, A., Murdoch, N., Schimmel, M., Smrekar, S.E., Stutzmann, E., Tauzin, B., Tharimena, S. (2020), MSS/1: Single-station and single-event marsquake inversion, J. Geophys. Res.-ESS, doi:10.1029/2020EA001118

Xu, H. and Beghein, C. (2019), Measuring Higher-Mode Surface Wave Dispersion Using a Transdismensional Bayesian Approach, Geophys. J. Int., 218 (1), 333-353, doi:10.1093/gji/ggz133

CHAPTER 1

Introduction

Surface wave data are widely used in seismic tomography, mainly due to their good signal-to-noise ratio (SNR) and better depth resolution than body waves. The dispersion of surface waves describes the relationship between their frequencies and phase or group velocities. Such variations of surface wave velocities are due to the fact that surface waves at different periods sample the Earth structure at different depths, with longer period data being more sensitive to deeper structure than shorter period data. Surface wave dispersion primarily constrains the path-averaged shear-wave velocity structure between a station and a seismic event. The effects of other factors, such as P-wave speed and density, are almost negligible compared to the effect of shear-wave velocity. On Earth, fundamental mode surface waves, with their usually high SNR, are the most commonly used types of surface waves in seismic tomography. Measurements at intermediate periods (between $\sim$30 s and 200 s) can resolve structure down to 200-300 km. Higher mode surface waves carry unique, independent constraints on structure at greater depths than commonly used fundamental modes, and thus enhance the vertical resolution of surface wave tomographic models in the deep upper mantle, transition zone, and uppermost lower mantle. However, most surface wave tomography studies are still limited to fundamental mode surface waves to which traditional measurement techniques can only be readily applied. Measuring higher modes is more complicated, mainly due to the fact that their group velocities overlap significantly in a broad frequency range and thus they do not appear as a clear wave train on the seismogram.

In this thesis, I focus on the development of a waveform fitting method that extracts the

one-dimensional (1-D) path-average structural information of planets from both fundamental and higher modes Rayleigh waves, and then discuss two applications based on this method. For the waveform fitting, we take advantage of a hierarchical transdimensional Bayesian approach [Bodin and Sambridge, 2009; Bodin et al., 2012], which efficiently and parsimoniously samples the model space. The generated Monte Carlo Markov Chains (MCMC) save an ensemble of shear-wave velocity (V_S) and associated phase velocity models, and thus enables us to quantitatively assess the uncertainties of each of the model parameters. Those path-average results can be combined to generate 2-D phase velocity maps and 3-D V_S models for the study areas.

In Chapter 2, I present the waveform fitting method based on a transdimensional MCMC approach. This part is based on Xu and Beghein [2019] and is the theoretical background of our research.

Chapter 3 presents a 3-D anisotropic V_S model of Antarctica obtained using our method.

Chapter 4 discusses the possibility of measuring higher modes on Mars or other planetary bodies using our method.

Chapter 5 concludes this thesis.

CHAPTER 2

Methodology

In this chapter, we explain the waveform fitting method we used to measure surface wave dispersion and to obtain 1-D path-averaged profiles for Rayleigh waves, and discuss the tests we did for validation purpose.

2.1 Overview of Previous Higher Modes Surface Wave Studies

The measurement of higher modes surface waves is challenging in that their group velocities overlap significantly in a broad frequency range. Consequently, the direct measurement methods that work for fundamental mode surface waves cannot be applied to higher modes due to the difficulties in separating different modes. Only in very specific and rare cases has it been possible to isolate and measure the dispersion of the first higher mode Rayleigh wave using single mode dispersion methods [Crampin, 1964; Roult and Romanowicz, 1984].

One way to take advantage of the information contained in higher-mode surface waves is to retrieve velocity structure directly, without extracting dispersion curves first. Most of these techniques involve determining path-averaged shear-wave velocity structure for multiple station-receiver pairs and combining them to obtain three-dimensional (3-D) models of Earth's internal structure. Cara and Lévêque [1987] determined path-averaged V_S models from a single seismogram using mode branch cross-correlation functions [Lerner-Lam and Jordan, 1983] as secondary observables. This method, which was designed to minimize the dependence on the starting model, was later automated and combined with a regionalization

scheme [Montagner and Nataf, 1986] to model 3-D velocities [Debayle, 1999] and anisotropy [Maggi et al., 2006]. Nolet Nolet [1990] developed a two-step non-linear Partitioned Waveform Inversion (PWI) technique that was automated by Lebedev and Nolet [2003]. Using synthetic seismogram calculations, the PWI finds along-path velocity models that fit recorded waveforms and inverts the velocity models obtained for all paths to constrain 3-D structure. citetLi1995,Li1996 were also able to obtain the averaged structure along the great circle between the source and receiver using a waveform modeling technique that included non-linear asymptotic coupling theory and coupling across different branches.

Despite the difficulty, several attempts have been made to separate higher modes. Some methods operate in the frequency-wavenumber ($\omega - k$) domain and use seismic arrays [Nolet, 1975; Cara, 1973, 1978, 1979]. While this kind of direct measurement is fast to implement, there are a few limitations: (i) the method can only be applied in regions with dense arrays and thus cannot be applied at the global scale, (ii) it requires the usage of linear regional seismic arrays approximately aligned with the epicenter, which reduces the geographical ray coverage, and (iii) variations within an array cannot be assessed [Laske and Widmer-Schnidrig, 2015].

Another method, based on mode branch stripping, was developed by van Heijst and Woodhouse [1997a]. The principle behind this technique is that the signals of overtone branches can be isolated by fitting the cross-correlation function of a single mode using mode branch cross-correlation functions. However, while this method does not rely on arrays and thus can be used in global tomography, it does not work well with epicentral distances shorter than 30° [van Heijst and Woodhouse, 1999a] since individual higher modes cannot be separated from others in a seismogram when the path is too short. Additionally, it might be difficult to separate one single mode from observed seismograms when that mode is contaminated by interference from other modes.

Other researchers have utilized waveform fitting techniques to extract higher-mode dispersion. Stutzmann and Montagner [1993] and Montagner et al. [1994] developed a wave-

form fitting technique to invert phase velocity dispersion and velocity structure at depth in successive steps. Beucler et al. [2003] proposed a roller-coaster technique, in which the phase velocity perturbation is obtained by fitting the synthetic seismogram to the real data. Yoshizawa and Kennett [2002, 2004] and Yoshizawa and Ekström [2010] used the Neighborhood Algorithm [Sambridge, 1999a] to search the model space for multimode dispersion in a nonlinear waveform inversion. Visser et al. [2007] developed a method similar to that of Yoshizawa and Kennett [2002] to estimate multimode dispersion curves for global tomography, though they were additionally able to obtain quantitative uncertainties on the phase speed measurements by performing a Bayesian appraisal of the models sampled [Sambridge, 1999b]. Uncertainties were determined from the whole ensemble of dispersion models obtained instead of taking the standard deviation of the 1,000 best models as in Yoshizawa and Kennett [2002].

In our study, we developed a waveform modeling method using a reversible jump Markov Chain Monte Carlo (rj-MCMC) inversion [Bodin and Sambridge, 2009] to extract higher mode dispersion curves and their uncertainties at periods between 50 s and 200 s. Like the methods of Yoshizawa and Kennett [2002], Yoshizawa and Ekström [2010], and Visser et al. [2007]; Visser [2008], our technique has the advantage of sampling the model space instead of choosing one model among many possible solutions with a strong regularization scheme. It therefore provides more reliable posterior model uncertainties than regularized inversions. Additionally, contrary to those previous studies in which the authors adopted a fixed dimension model space chosen a priori, the rj-MCMC sampler offers a way to treat the dimension of the model space as variable. In addition, because we use a Hierarchical Bayes approach, data noise parameters are treated as unknowns in the inversion, which accounts for the part of the signal that we are not able to explain with our forward theory and the chosen parametrization. This allows the model to explain the data without overfitting them.

2.2 1-D Waveform Modeling

Our goal is to measure phase velocity dispersion for fundamental and higher mode Rayleigh waves using waveform modeling. To do this, we seek a large number of path-averaged 1-D shear-velocity models that can fit the filtered waveform, and the resulting models are employed to calculate dispersion curves. These path-specific 1-D models represent the average fundamental and higher-mode dispersion curves for the chosen source-receiver path as in Yoshizawa and Kennett [2002], Yoshizawa and Ekström [2010], and Visser et al. [2007]; Visser [2008]. Our method thus requires a fast forward modeling method to compute synthetic seismic waveforms.

A synthetic seismogram (s) can be calculated by summation of normal modes (m) of amplitude A_m in the frequency domain (ω) for a 1-D model as follows (e.g. Dahlen and Tromp [2021]):

$$s(\omega) = \sum_m A_m(\omega) exp[i\omega\Delta/c_m(\omega)] \tag{2.1}$$

where $c_m(\omega)$ is the phase velocity of the mode m at angular frequency ω and Δ is the epicentral distance. The relationship between seismograms and their corresponding velocity model is thus highly non-linear. A fully non-linear approach, which does not require any partial derivatives with respect to model parameters or any strong constraints on parametrization, is therefore desirable to perform waveform inversion.

FORTRAN code Mineos [Masters et al., 2011] can be used to compute synthetic seismograms for a reference 1-D model of Earth's interior by normal mode summation. The advantage of such formulation is that it builds a direct connection between seismic waveforms and phase velocities. However, the calculation of normal mode eigenfunctions and eigenfrequencies for a given mantle model is very time-consuming and thus we cannot use the fully non-linear formulation that is Eq. 2.1 at each iteration of a MCMC scheme. We decided instead to linearize the forward modeling problem in order to overcome the computational speed limitation. As in Yoshizawa and Kennett [2002], we obtained a first synthetic

seismogram for a reference model using fully non-linear calculations (Eq. 2.1). We then used perturbation theory to update the seismogram for other models generated at each iteration of the Markov Chain. For a small perturbation, the change in mode eigenfrequency can be calculated assuming unperturbed eigenfunctions:

$$\delta \ln(\omega) = \int_0^a (\frac{\delta\alpha}{\alpha}(r)K_\alpha(r,\omega) + \frac{\delta\beta}{\beta}(r)K_\beta(r,\omega) + \frac{\delta\rho}{\rho}(r)K_\rho^{'}(r,\omega))dr + \sum_d \delta d[K_d(\omega)]_-^+ \quad (2.2)$$

where $\delta \ln(\omega) = \delta\omega/\omega$, a is the radius of the Earth, and α, β, ρ and d are P-wave velocity, S-wave velocity, density, and radius of discontinuities, respectively. $K_\alpha, K_\beta, K_\rho^{'}$ and K_d are the Fréchet derivatives, which relate the change in wave velocities, density, and depth of discontinuity from the reference model to changes in the eigenfrequencies. The Fréchet derivatives can be calculated for each mode using the eigenfunctions determined for the reference model [Woodhouse, 1980].

In principle, all parameters could be included as free parameters in inversions. Nevertheless, strong trade-offs can affect them, and only shear-wave perturbations are generally well resolved (e.g., Montagner and Nataf [1986]; Meier et al. [2009]). Previous endeavors to invert for δV_P, δV_S, $\delta\rho$, δd, and/or anisotropic parameters in Earth's mantle have been done, either with regularized inversions (e.g., Panning and Romanowicz [2006]) or model space search techniques (e.g., Beghein and Trampert [2006]; Beghein [2010]). The resulting V_S models do not generally depend on the inclusion of the other unknowns in the inversions, but the less well-resolved parameters have large uncertainties and are dependent on the prior information introduced [Beghein, 2010]. In addition, a larger number of free parameters in a model space search significantly increases the convergence time and adds to the computational costs. We therefore decided to scale δV_P and $\delta\rho$ to δV_S using relations derived for Earth: $\delta \ln V_P = m_\alpha \delta \ln V_S$ and $\delta \ln \rho = m_\rho \delta \ln V_S$. For the P-wave speed scaling, we used a linearly varying scaling relation, with $m_\alpha = 0.8$ at Earth surface and $n_\alpha = 0.565$ at 800 km depth. For the density scaling, we set m_ρ to 0.3 [Anderson et al., 1968]. These choices do not typically affect the V_S models in Earth applications so we do not expect it to play an important role here either. Correctly accounting for the Moho depth has been shown

to be important as it can have strong non-linear effects on waveform modeling and phase velocity calculations [Montagner and Jobert, 1988]. We decided to account for deviations from Preliminary Reference Earth Model (PREM) [Dziewonski and Anderson, 1981] in Moho depth by adopting a reference model that includes crustal constraints from model CRUST1.0 [Laske et al., 2013], averaged over the length of the chosen path, and calculating the corresponding shear-wave sensitivity kernels. The updated frequency can then be converted into phase velocity for a normal mode of angular order l using [Jeans, 1923; Dahlen and Tromp, 2021]:

$$c(\omega^*) = \frac{\omega^* a}{l + 0.5} \tag{2.3}$$

where ω^* is the updated eigenfrequency for the mode considered. In Figure 2.1, we compare synthetic seismograms calculated using the the normal mode summation without linearization (Eq. 2.1) and the linearized method based on perturbation theory described above (Eq. 2.2). The results show that the phase velocity information from the linearized perturbation method and the non-linear formulation match well, especially in the period range we are interested in (50 s-200 s).

2.3 Selection of Frequency-Time Windows

The rj-MCMC method described below performs a guided Monte Carlo sampling of the model space using the values of the misfit between the real and the synthetic seismograms. The data and the synthetics are compared in different time and frequency windows, which are chosen such that they include the fundamental and several higher modes. We used different time and frequency windows to compare the fundamental and higher mode waveforms. We employed group velocities to choose the beginning and the end of the time windows for the fundamental mode and we employed S- or SS-wave arrival times and group velocities to choose the higher mode time window as in Lebedev and Nolet [2003]. For epicentral distance shorter than 35° the higher mode window start time is set just before the arrival of the S

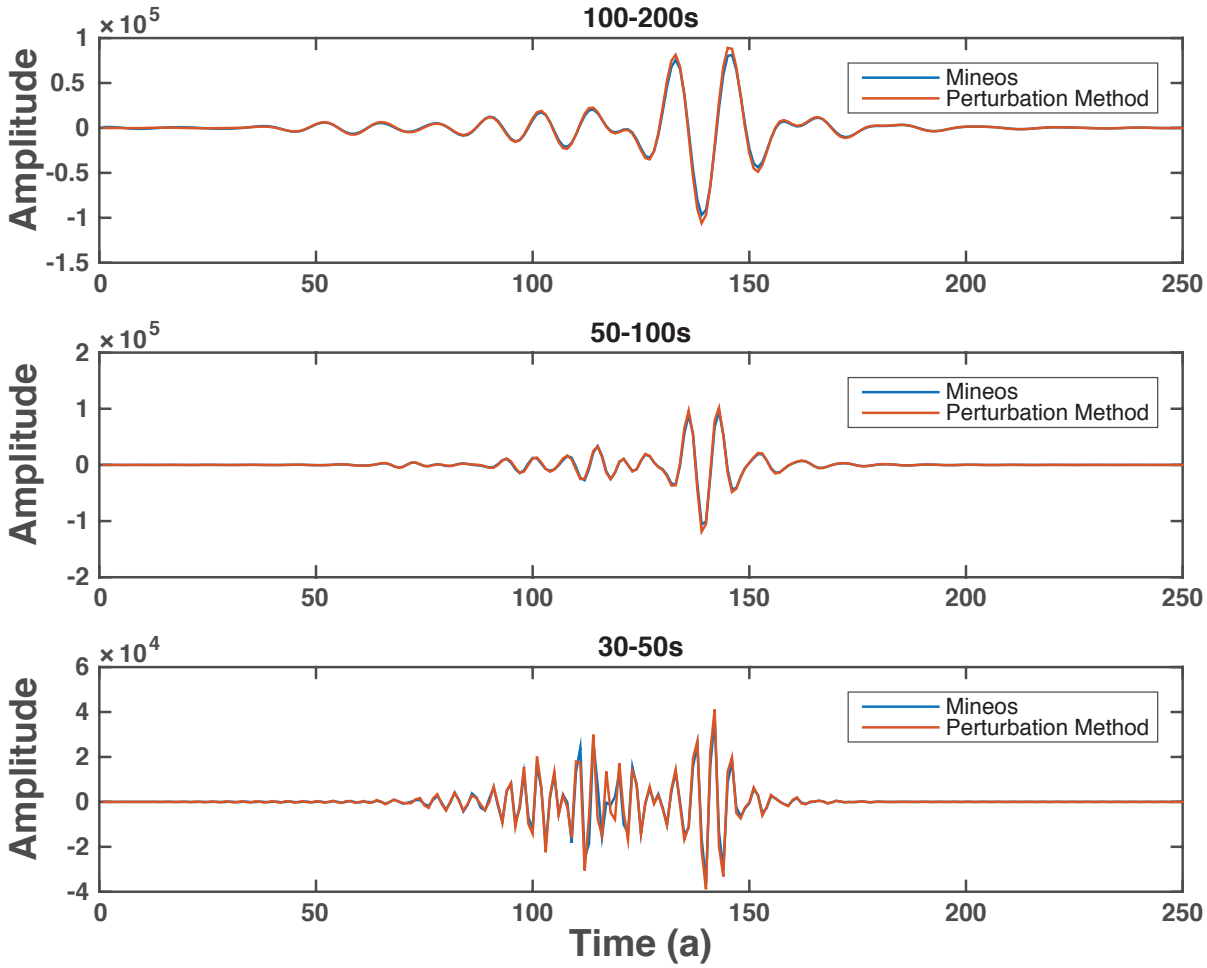

Figure 2.1: Comparison between synthetic seismograms calculated with normal mode summation using Mineos without linearization (blue) and with our linearized method (red) in three different period ranges: 100 s-200 s (top), 50 s-100 s (middle), and 30 s-50 s (bottom). The shear-velocity model used to compute the seismograms is shown in Figure 2.3.

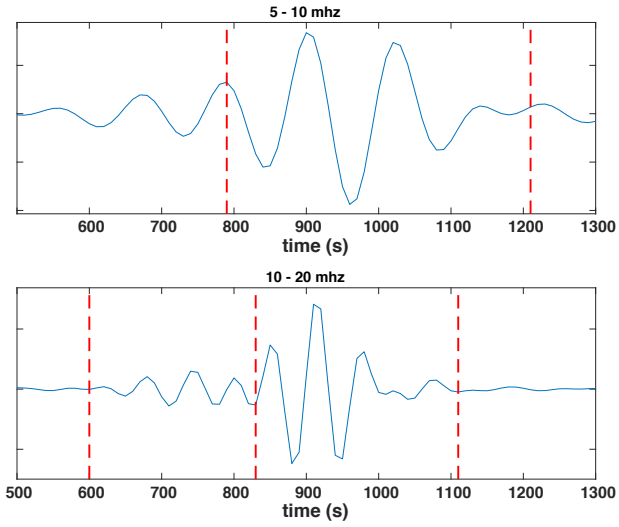

Figure 2.2: An example of our automatic time window selection for a path across North America. The waveform is for the observed data. The station, HRV, is located in northeastern America. The event was in Chiapas, Mexico and occurred on 6 July, 2007. The time window in the upper panel is window 1 as defined in Table 2.1. The time window on the right side of the lower panel is for the fundamental mode (window 2) and the time window on the left of the lower panel is the higher modes window (window 3).

wave train. For epicentral distance between 35° and 70° the start time is just after the S and before the SS wave train. Group velocities can be picked manually by inspection of the waveform or using a frequency-time analysis [Dziewonski et al., 1969]. Those windows are summarized in Table 2.1. An example of time window selection on real data is shown in Fig 2.2 for an event in Chiapas, Mexico and station HRV in north eastern America.

Because the amplitude of the synthetic seismograms depends on the scalar moments of the event, and because inaccurate scalar moments in catalogues might cause an increase in the data misfit, we implemented an energy equalization method [Lebedev et al., 2005] before calculating the misfit between observed and synthetic seismograms (defined in section 2.4). The aim is to equalize the energy of the synthetic with that of the data by multiplying the

Table 2.1: Selection of frequency-time windows. The first and second window indices correspond to the fundamental mode and the third window is for higher modes. The start and end times for the fundamental mode are determined by the group velocities U indicated in the table and the event epicentral distance Δ. For the higher modes, the beginning of the time window is determined by the S- or SS-wave arrival times. The end of the window is determined by Δ/U.

Window index	**Frequency(mHz)**	**Start**	**End**
1	5-10	$U = 4.45\ km/s$	$U = 2.95\ km/s$
2	10-20	$U = 4.30\ km/s$	$U = 3.20\ km/s$
3	10-20	S or SS	$U = 4.30\ km/s$

amplitude of the synthetics by the following constant:

$$f^{eq} = \sqrt{\frac{\sum_{t=t_1}^{t=t_2} d^2(t)}{\sum_{t=t_1}^{t=t_2} s^2(t)}} \tag{2.4}$$

where $d(t)$ and $s(t)$ are the observed and synthetic seismograms, respectively, filtered in the frequency range considered (5mHz - 20mHz). t_1 indicates the beginning of the overtone time window (window 3 defined in Table 2.1) and t_2 is the end of the first fundamental mode time window (window 1 in Table 2.1).

2.4 Bayesian Inference

In a Bayesian formulation, model parameters are described by probability density functions (PDFs), which effectively indicate the uncertainty associated with these parameters. The aim of a Bayesian inference is to quantify the *a posteriori* probability distribution of all model parameters given some prior information and the data. Bayes' theorem [Bayes and Price, 1763] gives the posterior as:

$$p(\mathbf{m}|\mathbf{d}_{obs}) \propto p(\mathbf{d}_{obs}|\mathbf{m})p(\mathbf{m}) \tag{2.5}$$

where $A|B$ means A given (or conditional on) B, i.e. the probability of having A when B is fixed. $\mathbf{m}$ is the vector of model parameters and $\mathbf{d}_{obs}$ is the observed data. The term $p(\mathbf{d}_{obs}|\mathbf{m})$ is called likelihood function, which shows the probability of observing data $\mathbf{d}_{obs}$ given a particular model $\mathbf{m}$. The *a priori* probability of model, $p(\mathbf{m})$, contains what we assume about the model $\mathbf{m}$ before having the observed data. Accordingly, the posterior distribution represents the probability of the model, given the observed data. The parts of the model space that are more frequently required by the data than others manifest with greater posterior probability, and hence are more likely to reflect properties of the Earth [Backus, 1988].

The likelihood function $p(\mathbf{d}_{obs}|\mathbf{m})$ describes the probability of data given the current model. In this study, we compared the waveform fit in three different frequency-time windows, and we assumed the data noise in each window follows a multivariate normal distribution with zero mean and covariance matrix $\mathbf{C}_{d_i}$, where i is the window index. The likelihood term for each frequency-time window is thus written in this form:

$$p_i(\mathbf{d}_i|\mathbf{m}) = \frac{1}{\sqrt{(2\pi)^n|\mathbf{C}_{d_i}|}} \times \exp[-\frac{\Phi_i(\mathbf{m})}{2}] \tag{2.6}$$

where d_i is the data in window i, $\Phi_i(\mathbf{m})$ is the function describing the distance between real data and synthetics predicted by the current model. The general expression for $\Phi_i(\mathbf{m})$ considering correlated noise is [Bodin et al., 2012]:

$$\Phi_i(\mathbf{m}) = (G(\mathbf{m}) - \mathbf{d}_i)^T \mathbf{C}_{d_i}^{-1} (G(\mathbf{m}) - \mathbf{d}_i) \tag{2.7}$$

where $\mathbf{d}$ represents the measured data vector and $G(\mathbf{m})$ is for the synthetic data predicted by model $\mathbf{m}$.

For simplicity, we assumed Gaussian and uncorrelated noise, in which case the covariance matrix is diagonal. Then the equation above becomes:

$$\Phi_i(\mathbf{m}) = M_i(\mathbf{m})/\sigma_i^2 \tag{2.8}$$

where σ_i is the standard deviation of the Gaussian uncorrelated noise in the i-th frequency-time window, i.e., the diagonal element of the covariance matrix, and M_i is defined by:

$$M_i(\mathbf{m}) = \sum_{j=1}^{L_i} (d_i^j - f^{eq} s_i^j)^2 \tag{2.9}$$

where L_i is the length of the selected time window, d_i is the observed data, s_i is the synthetics calculated for model $\mathbf{m}$, and f^{eq} is the energy equalization factor defined in Eq. 2.4. The expression for the likelihood becomes:

$$p(\mathbf{d}_i|\mathbf{m}) = \frac{1}{(\sqrt{2\pi}\sigma_i)^n} \times \exp[-\frac{M_i(\mathbf{m})}{2\sigma_i^2}] \tag{2.10}$$

The total likelihood function is then the product of the likelihood functions of three frequency-time windows:

$$p(\mathbf{d}_{obs}|\mathbf{m}) = p(\mathbf{d}_1|\mathbf{m})p(\mathbf{d}_2|\mathbf{m})p(\mathbf{d}_3|\mathbf{m}) \tag{2.11}$$

As shown in Eq. 2.6, the level of noise accounts for theoretical errors, that is, the part of the signal that we are not able to explain with the forward theory and with the chosen parametrization, which is a simplified and discretized representation of reality. Unlike traditional inversion methods in which the noise level is fixed at a presumed level, we use a Hierarchical Bayesian approach, treating noise parameters σ_1, σ_2, σ_3 as unknowns in the inversion. These noise parameters therefore determine the width of the Gaussian likelihood function and the relative weight given to different frequency-time windows during the inversion. The diagonal element σ_i is given by a uniform prior distribution, which is explored during the Monte Carlo search. An advantage of this approach is that the weights of the different frequency-time windows are constrained by the data, thereby avoiding an arbitrary choice of noise levels by the user and the risk of overfitting the data. In addition, windows with better waveform fit will naturally have higher weights since the relative weight between different windows is controlled by the data error levels σ_1, σ_2, σ_3.

Following Bodin et al. [2012], a uniform prior distribution with relatively wide bounds is adopted here so that the final model will be dominated by the data rather than by prior

information. When only independent parameters are considered, the prior probability distribution can be written as the product of three terms:

$$p(\mathbf{m}) = p(\mathbf{c}, \mathbf{v}|k)p(k)p(\mathbf{h}), \tag{2.12}$$

where **c,v** are vectors containing the depth and velocity of each interpolation point, $p(k)$ is the prior on the number of layers, and $p(\mathbf{h})$ is the prior on noise hyper-parameters. Details of the derivation for the expression of $p(\mathbf{m})$ can be found in Bodin et al. [2012]. Here, we only show the expression for velocity priors at the ith interpolation point v_i:

$$p(\mathbf{v}|k) = \begin{cases} \frac{1}{\Delta v} & \text{if } V_{min} \leq v_i \leq V_{max} \\ 0 & \text{otherwise,} \end{cases} \tag{2.13}$$

where V_{max} and V_{min} are the upper and lower bounds of velocity, and Δv is equal to $(V_{max} - V_{min})$. Any velocity that falls outside this pre-defined boundaries leads to a null prior. For our study, we chose $\Delta v = 10\%$ of the velocity in the reference model at a given depth.

2.5 The rj-MCMC method

The goal of the rj-MCMC method is to generate an ensemble of Earth models distributed according to a target distribution. In our case, we want to find the 1-D shear velocity models that best fit the waveform data to represent the dispersion of multiple modes along a specific source-receiver path.

Most inversion schemes adopt a fixed dimension model space. However, we do not know the complexity of the V_S profile, i.e. the dimension of the model space, a priori. One potential drawback of fixing the depth parametrization is that different seismograms may require different number of model parameters to improve the fit and the results could potentially depend on the chosen prior parametrization. Here, we adopted a transdimensional Bayesian inversion, which consists in a sampling-based algorithm that include the number of parameters in the set of unknowns and hence the constraints added on the uncertain parametrization

or uncertain data errors can be released. The transdimensional approach lets the data themselves constrain the allowable model complexity instead of having the user choose a model parametrization (e.g., number of layers, or cells) a priori. It is well-known, however, that increasing the complexity of the model parametrization often results in better data fit and introduces parameter trade-offs. One difficulty in inverse problems is to determine which parameters are well resolved and how much complexity is really needed by the data. To avoid this problem, the rj-MCMC sampler, first proposed by Geyer and Møller [1994], is designed to find a parsimonious solution [Malinverno, 2002], i.e. it naturally discourages high dimensional (many layers) models and the least complex explanation or model for an observation is preferred to avoid over-fitting the data.

The rj-MCMC method has been explained in detail in Bodin and Sambridge [2009] and Bodin et al. [2012]. Our method is based on theirs except that we used a different depth parametrization. The nodes in the two different parametrizations have, nevertheless, a similar meaning and the derivations are similar to theirs. The main difference comes from the way the velocity models are constructed. In Bodin et al. [2012], each Voronoi nucleus defines its nearest neighbor region as one layer, which has the same velocity as the nucleus within it. By contrast, in our model the shear-wave velocity perturbation at a given depth is interpolated from its two nearby nodes.

In the rj-MCMC method, every new model is generated by iteratively perturbing the last one according to some chosen proposal distribution. There are five types of perturbation based on the parametrization we chose:

- Change the velocity of one interpolation point;
- Birth: create a new interpolation point;
- Death: remove one interpolation point at random;
- Move: Randomly pick one interpolation point and move it to a new depth;

- Change the noise level;

Here we have employed a slightly different model proposal for Birth than Bodin et al. [2012] due to the different parametrization used here. The other proposals are the same. For the birth step, we added a new interpolation point at depth $c_{k+1}^{'}$, and then assigned a new velocity perturbation value $v_{k+1}^{'}$ to this new node. This is drawn from a Gaussian proposal probability density:

$$q(v_{k+1}^{'}|v_*) = \frac{1}{\theta_{birth}\sqrt{2\pi}}\exp\left\{-\frac{(v_{k+1}^{'}-v_*)^2}{2\theta_{birth}^2}\right\} \tag{2.14}$$

where v_* is the current velocity perturbation value at the depth $c_{k+1}^{'}$ where birth takes place. The value of v_* can be calculated by a simple interpolation between its two nearest nodes. The standard deviation θ_{birth} of the Gaussian distribution is a parameter to be chosen. We refer the reader to Bodin et al. [2012] for the proposal distributions of other types of perturbation.

New models generated from those perturbations are then randomly accepted or rejected according to the acceptance ratio. In order to converge to the target distribution $p(m|\mathbf{d}_{obs})$, the acceptance probability from the current model $\mathbf{m}$ to the proposed model $\mathbf{m}^{'}$, $\alpha(\mathbf{m}^{'}|\mathbf{m})$, has to meet the following requirement:

$$\alpha(\mathbf{m}^{'}|\mathbf{m}) = min\Big[1, \frac{p(\mathbf{m}^{'})}{p(\mathbf{m})}\cdot\frac{p(\mathbf{d}_{obs}|\mathbf{m}^{'})}{p(\mathbf{d}_{obs}|\mathbf{m})}\cdot\frac{q(\mathbf{m}|\mathbf{m}^{'})}{q(\mathbf{m}^{'}|\mathbf{m})}\cdot|\mathbf{J}|\Big], \tag{2.15}$$

where the matrix $\mathbf{J}$ is the Jacobian of the transformation from $\mathbf{m}$ to $\mathbf{m}^{'}$.

The derivations of acceptance probability in rj-MCMC method were given by Bodin et al. [2012], Appendix C. Here we will only describe the ideas briefly and show the equations that differ from theirs. For moves without change of dimension, both the Jacobian term and the ratio of proposal distributions are 1 and the reader can find the same results as Bodin et al. [2012] by inserting Eqs. 2.10 and 2.12 into Eq. 2.15. For the birth and death steps which involve a change of dimension, it can be shown that the Jacobian term is equal to 1. However, due to the different birth proposal distribution we selected, the expression for the

acceptance term for the birth and death steps are different from Bodin et al. [2012]. For the birth step:

$$\alpha(\mathbf{m}^{'}|\mathbf{m}) = min\Big[1, \frac{\theta_{birth}\sqrt{2\pi}}{\Delta v} \cdot \exp\left\{\frac{(v_{k+1}^{'} - v_*)^2}{2\theta_{birth}^2}\right\} \cdot \frac{p(\mathbf{d}_{obs}|\mathbf{m}^{'})}{p(\mathbf{d}_{obs}|\mathbf{m})}\Big], \tag{2.16}$$

The meaning of $v_{k+1}^{'}$ and v_* is the same as in (2.14). For the death step:

$$\alpha(\mathbf{m}^{'}|\mathbf{m}) = min\Big[1, \frac{\Delta v}{\theta_{birth}\sqrt{2\pi}} \cdot \exp\left\{-\frac{(v_j^{'} - v_i^{'})^2}{2\theta_{birth}^2}\right\} \cdot \frac{p(\mathbf{d}_{obs}|\mathbf{m}^{'})}{p(\mathbf{d}_{obs}|\mathbf{m})}\Big], \tag{2.17}$$

where v_i is the velocity of the i-th interpolation point to be removed at depth c_i and v_* is the velocity at depth c_i in the new structure after the removal of the i-th node.

If the newly proposed model is rejected, then the last model is retained for another iteration. The Markov chain is generated via hundreds of thousands of iterations. The first part of the chain (called the burn-in period) is discarded, after which the random walk is assumed to be stationary and starts to sample the model space according to the posterior distribution $p(\mathbf{m}|\mathbf{d}_{obs})$. If the algorithm is run long enough, these samples should then provide a good approximation of the structure of Earth as constrained by the data.

This ensemble solution contains many models with variable parametrization, and each V_S model in the ensemble corresponds to one dispersion relationship. The expected dispersion is the weighted average through the posterior distribution sampled by the rj-MCMC algorithm. One can use this average to choose one dispersion curve with proper uncertainties for interpretation purpose.

2.6 MCMC Sampling Steps and Parametrization

In this study, we seek a 1-D depth-dependent isotropic shear velocity model to represent the dispersion of multiple modes between a chosen source and receiver. The isotropic nature of the model is assumed mainly for computational reason, but it is a reasonable assumption as demonstrated by Visser [2008] who showed that the differences in the phase velocities

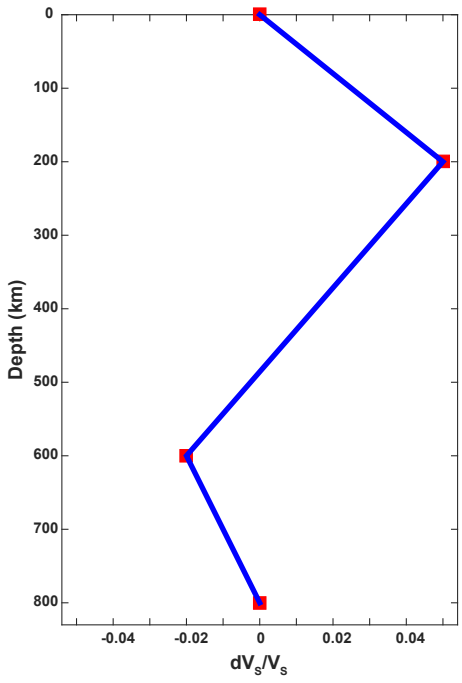

Figure 2.3: Example of model parametrization. The red squares denote the points at which the velocity model is perturbed. The complete dV_S profile is obtained by linear interpolation between those points.

calculated assuming isotropy or anisotropy are small. The V_S profile is described by a variable number k of interpolation points (Figure 2.3). The vertical position of these points defines the depths at which V_S is perturbed and the horizontal position of these points correspond to the amount V_S is perturbed relative to a reference model using the velocity prior described by Eq. 2.13. We adopted the rj-MCMC algorithm [Bodin and Sambridge, 2009] to explore the model space and sample the distribution of model parameters informed by the data. The procedure of our waveform inversion can be summarized as follows:

1. Choose path-specific reference 1-D shear velocity model

2. Calculate normal mode eigenfrequencies for the reference model using Mineos, and compute a reference synthetic seismogram using normal-mode summation (Eq. 2.1);

3. Generate a path-specific 1-D shear velocity model by perturbing the reference model according to the proposal distribution of the rj-MCMC scheme;

4. Compute the synthetic seismogram predicted by the 1-D model using Eq. 2.2;

5. Calculate the misfit between synthetic and observed waveforms in each window using the L_2 norm;

6. Randomly accept or reject the proposed model according to the acceptance ratio;

7. If the model is accepted, calculate and save the phase velocities predicted by the model using Eq. 2.3 and generate a new V_S model by perturbing the accepted model according to the proposal distribution. If the model is rejected, generate a new V_S model by perturbing the previously accepted model according to the proposal distribution;

8. Repeat steps (4) to (7) to generate the Markov chains;

9. Gather all the saved phase velocities and V_s profiles to determine the distribution of dispersion curves obtained at each period/frequency and the distribution of V_s at each depth;

10. Calculate the mean and standard deviation of these distributions to obtain measured 1-D profiles and their uncertainties.

2.7 Reliability Analysis

In principle, with the proposed method we are able to obtain the phase velocities for any mode at any period since they are calculated from the ensemble of V_S models obtained. However, in practice, only some modes at certain periods can be reliably constrained by a single seismogram. It is thus important to estimate the reliability of the measurements in each frequency band for different modes. Here, we adopted a procedure similar to Yoshizawa and

Kennett [2002] and Yoshizawa and Ekström [2010] based on the Frequency-Time Analysis method [Dziewonski et al., 1969].

Let us first define the waveform fit $f(\omega, t)$:

$$f(\omega, t) = \exp\left[-\frac{S^{\text{mis}}(\omega, t)}{S^{\text{syn}}(\omega, t)}\right] \tag{2.18}$$

where $S^{\text{mis}}(\omega, t)$ represents the spectrogram of the difference between real data and the inverted synthetics. $S^{\text{syn}}(\omega, t)$ is the spectrogram of the whole synthetic waveform. Similarly, the relative power of the jth mode $p_j(\omega, t)$ is defined as:

$$p_j(\omega, t) = \exp\left[-\frac{S_j^{\text{res}}(\omega, t)}{S_j^{\text{syn}}(\omega, t)}\right] \tag{2.19}$$

where $S_j^{\text{syn}}(\omega, t)$ is the spectrogram of the jth mode waveform, and $S_j^{\text{res}}(\omega, t)$ is the spectrogram of the residual seismogram calculated as the difference between the full synthetic and the jth mode waveform. In practice, both the frequency ω and time t are discrete, so the spectrograms can be expressed in matrix form. For example, the element in the kth row and lth column of the spectrogram matrix represents the amplitude of $S(\omega_k, t_l)$, where ω_k is the discretized frequency and t_l is the center of the lth time window used in the frequency-time domain analysis.

The waveform fit $\mathbf{f}$ measures the difference between the synthetic and real data in the frequency-time domain. It is designed such that $f(\omega, t) = 1$ at all frequencies and times when the synthetic seismograms are identical to the observed data, and $\mathbf{f}$ decreases when the waveform fit becomes worse. The relative power $\mathbf{p}_j$, which measures the relative power of the jth mode, is designed in a similar way so that $p_j(\omega, t) = 1$ at all frequencies and time when the jth mode in the seismogram is completely dominant and there is no contribution from other modes, and $\mathbf{p}_j$ decreases as the contribution from the jth mode becomes smaller.

For the reliability analysis, we want to consider the overall waveform fit and the relative weight of one single mode at the same time because both factors indicate how well the phase velocities at certain frequencies are constrained by the data. That is, the measurement of

the jth mode becomes more reliable if the waveform fit is better, or if the relative weight of the jth mode increases. Following this criteria, we define the reliability parameter as:

$$r_j(\omega) = \sum_l p_j^{kl} f^{kl} \tag{2.20}$$

where p and f are defined in Eqs. 2.18 and 2.19. To get the reliability parameter of the jth mode $r_j(\omega)$, we first multiply the waveform fit by the relative weight of the jth mode in the F-T domain, and then integrate the resulting matrix with respect to time. In this way, the $r_j(\omega)$ is a function of frequency and can be regarded as an indicator of reliability at frequency ω for the jth mode. Examples of the reliability analysis are shown in the following sections.

2.8 Synthetic Test

We first present a synthetic test to demonstrate that our method can recover an input shear-wave velocity model well (Figures 2.4 and 2.5). A shear-wave velocity profile generated by perturbing the PREM model was used to calculate a synthetic seismogram. Figure 2.4(B) displays the input perturbation $dV_S(r)/V_S(r)$. It is characterized by +3% anomaly relative to PREM at 200 km depth and -2% at 600 km depth. The synthetic seismogram (Figure 2.6), representing the velocity of the ground motion, was calculated for a great circle path between the Banda Sea and Beijing, which corresponds to a distance of 5,347 km. We used the fundamental mode and the first ten overtones to calculate the synthetics and to invert the synthetic data. The event source parameters were taken from the GCMT catalog [Dziewonski et al., 1981; Ekström et al., 2012] and are shown in Table 2.2. Only the vertical component is considered for the waveform fitting. We generated correlated noise by bandpass-filtering a sequence of uncorrelated Gaussian (white) noise, and then added the correlated noise to the synthetic seismogram. This way, the filtered noise sequence is correlated and data points in the sequence are no longer independent. The noise level was set at 10% of the average amplitude of the waveform contained in the third time window as defined in Table 2.1, which

Table 2.2: Source parameters from GCMT Catalog. Event 200503021042A was used for the synthetic test. 200910151211A was for the western Australia path and 201004172315A for the eastern Australia path.

ID	**lat(°)**	**lon(°)**	**depths(km)**	M_0**(dyne-cm)**	**strike,dip,rake**
200503021042A	-6.54	129.99	196.1	5.73e+26	41,88,55
200910151211A	-3.04	139.45	105.1	1.34e+25	296,83,145
201004172315A	-6.82	147.30	62.9	2.19e+25	268,50,91

includes higher modes and excludes the fundamental mode.

The inversion of the synthetic waveform data was performed using eight Markov chains starting from different random models, with the length of each chain fixed at 120,000 iterations. To guarantee the convergence of the inversion when sampling the posterior distribution, the first 60,000 iterations in each chain were marked as 'burn-in' and we removed them from the ensemble of sampled models. The ensemble of dV_S/V_S solutions represented by a color density plot is displayed in Figure 2.4(A). The brighter color means the algorithm spent more time in that region, and therefore it corresponds to a more likely V_S structure at that particular depth. The mean output model calculated from the ensemble of solutions (Figure 2.4(B)), which can be regarded as the expectation of the "true model", is close to the input model. Figure 2.5(A) displays the posterior distribution of the number of parameters used by the algorithm during the inversion and demonstrates the parsimony of the trans-dimensional framework: although we can almost always fit the data better by introducing more parameters, the rj-MCMC method tends to prevent overfitting the data and prefer models of smaller dimensions. In this case the result shows there is a higher probability that the data can be explained by less than eight depth nodes. Figure 2.5(B) represents the posterior data noise level and shows that fitting the first time window required less data noise than the other two time windows.

A comparison between the input and output seismograms is shown in Figure 2.6, which

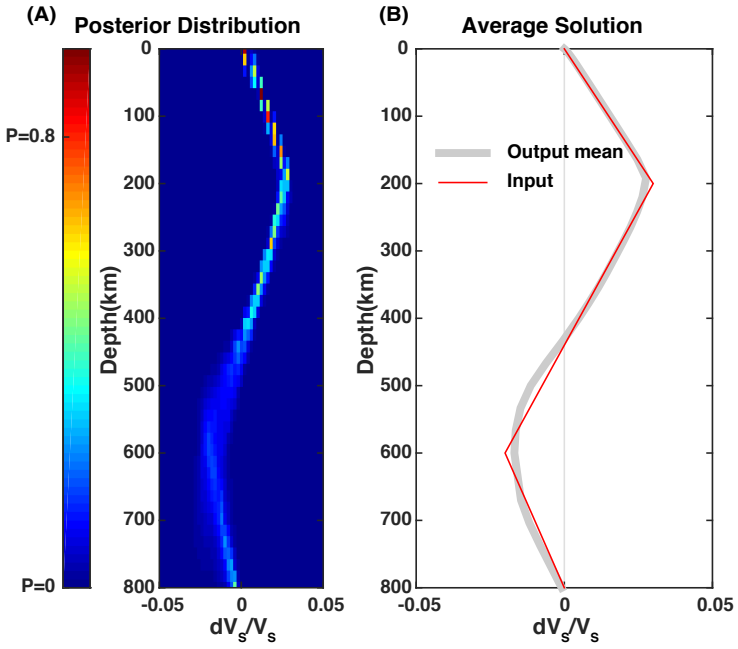

Figure 2.4: (A) Color density plot representing the ensemble of solutions obtained by inversion of the synthetic seismogram that was calculated with the input model shown in (B); The posterior mean model resulting from this distribution of solutions is also displayed in (B)

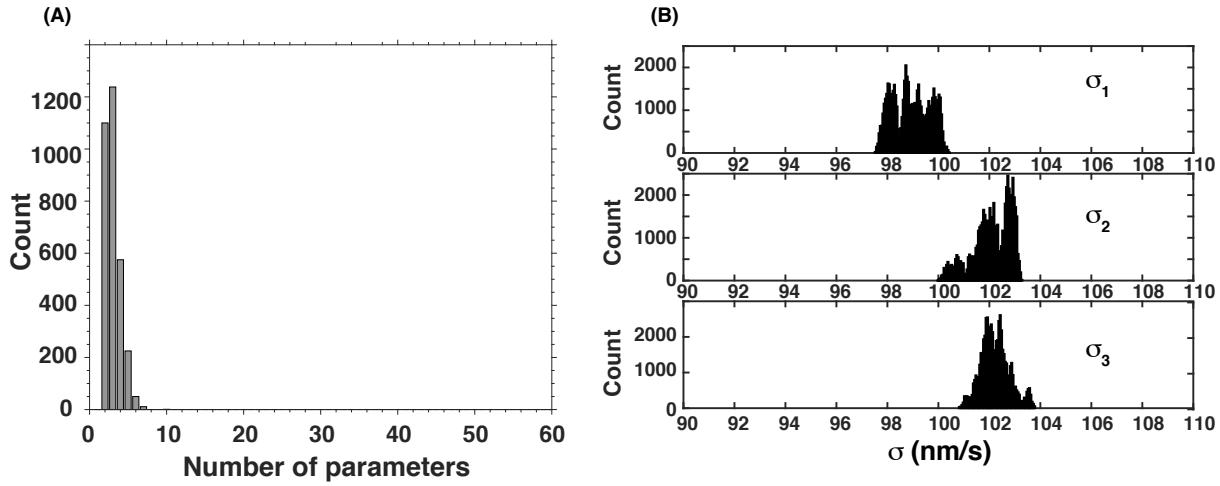

Figure 2.5: (A) Posterior distribution for the number of parameters in the synthetic test of Figure 2.4; (B) Posterior distribution for the data noise level for each of the three time windows considered.

shows that the predicted waveform resulting from our inversion fits the input data much better than the waveform predicted by PREM. The misfit between the inverted waveform and the input data is represented in Figure 2.7 both in the time domain and the F-T domain.

The fundamental mode and first overtone phase velocity dispersion was calculated and compared with the dispersion relationship predicted by the true model (Figure 2.8). The standard deviation of our measurements at each period were calculated from the ensemble of dispersion curves obtained. We see that the true dispersion curve is within the 95% likelihood contour of our inversion results at all periods.

We further applied the reliability analysis described in the previous section to our synthetic test. The relative weight of the first overtone is used as an example to demonstrate the method (Figure 2.9). The spectrogram of misfit in Figure 2.7 and the spectrograms of relative weights (like in Figure 2.9) were multiplied using Eq. 2.20 and summed along the time domain to obtain the reliability parameters as a function of frequency for each mode

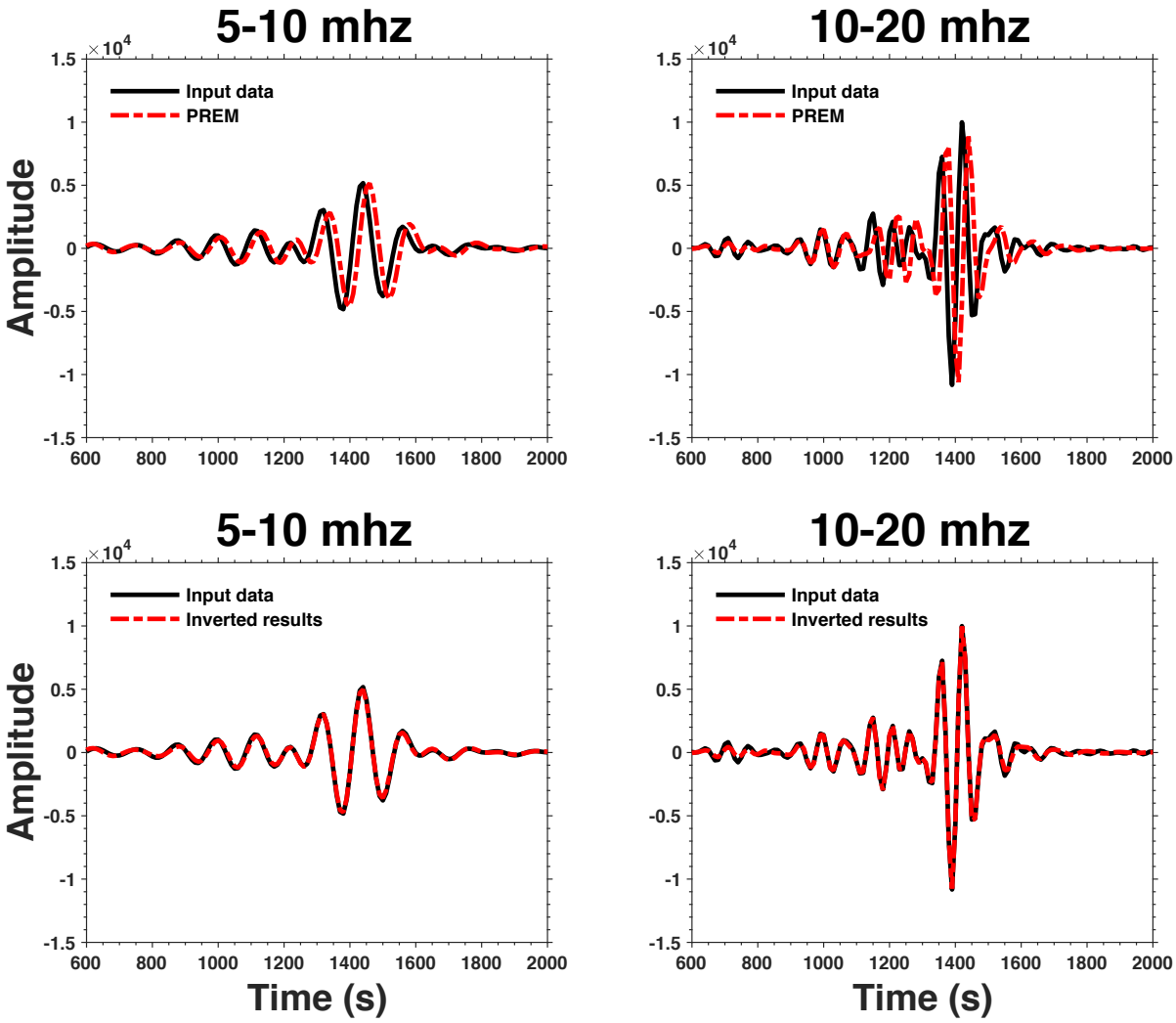

Figure 2.6: Comparison between input synthetic waveform and the waveform predicted by PREM (top) and by the mean model resulting from our inversion (bottom). The seismograms shown here represent the velocity of the ground motion. The input seismogram was calculated for the true model shown in Figure 2.4. Two frequency bands, as indicated in table 2.1, are considered separately. The waveforms match is much improved after inversion.

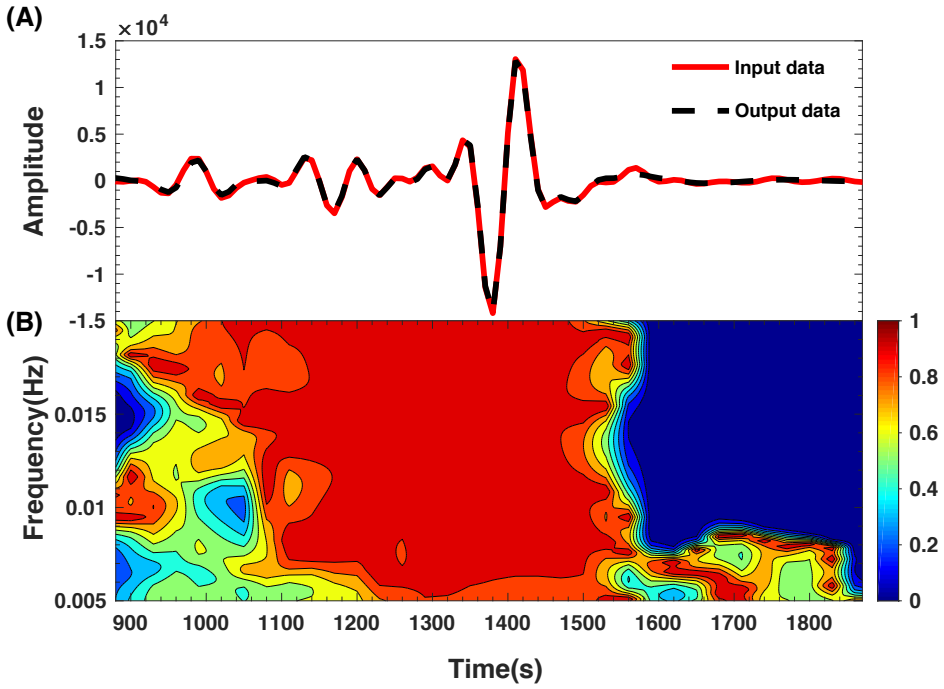

Figure 2.7: (A) Comparison between the output and input synthetic data in the time domain filtered in the 50s-200s period range; (B): Spectrogram of the waveform fit f(ω, t), as defined in equation 2.18. The regions with warmer colors correspond to better waveform fit in the F-T domain.

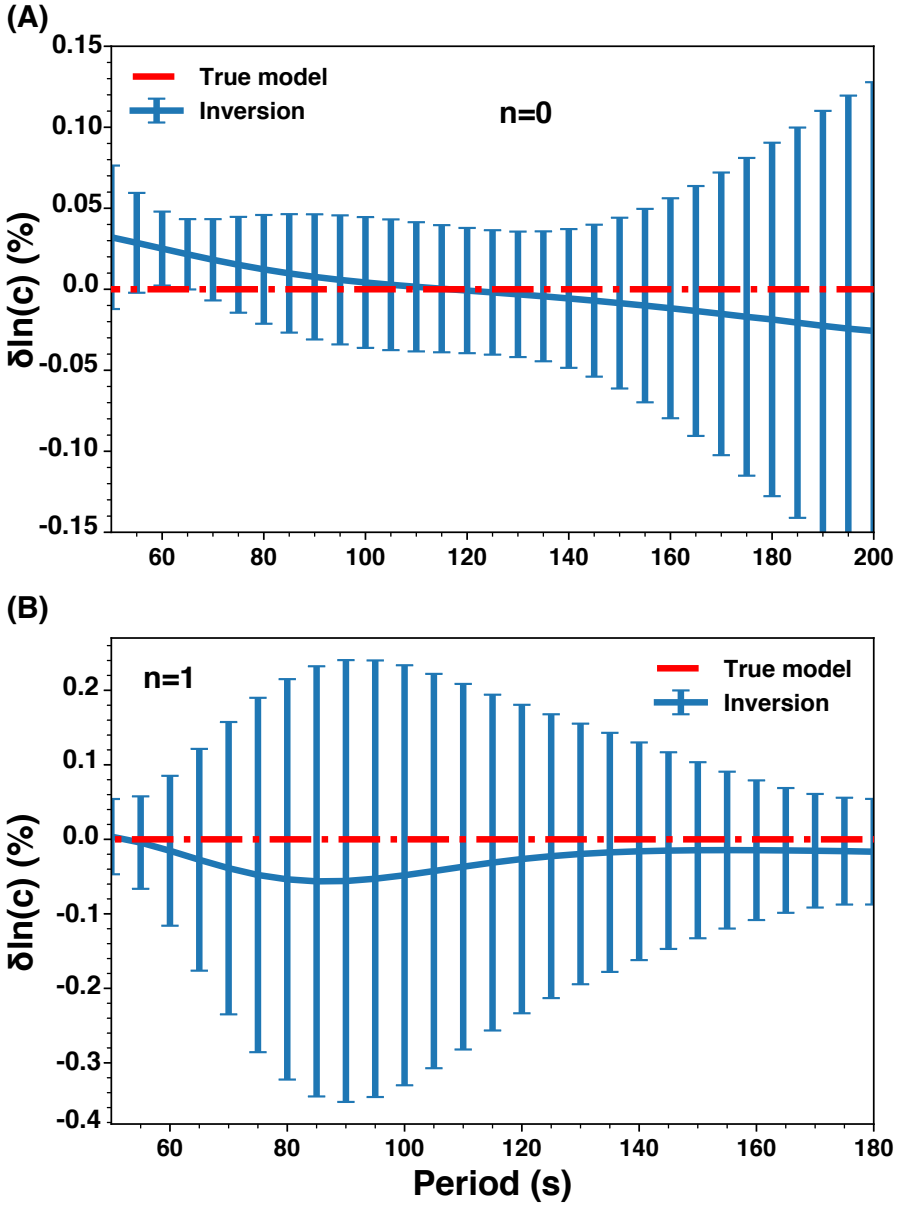

Figure 2.8: Inverted fundamental mode (A) and first overtone (B) phase velocity dispersion and uncertainties (blue) compared to the dispersion curve calculated for the true model (red). The uncertainties shown here correspond to 2σ obtained from the posterior distribution.

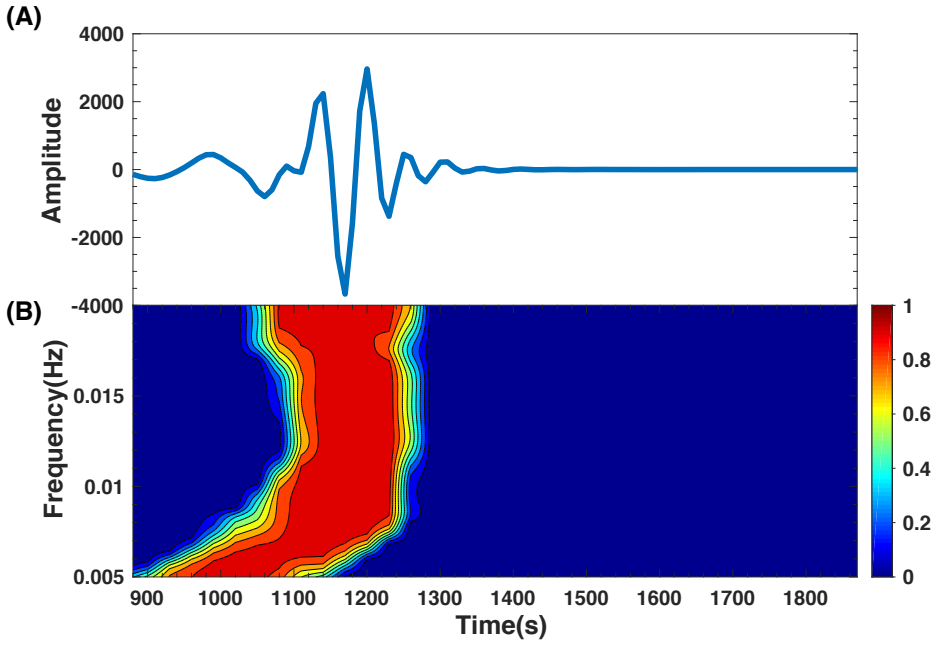

Figure 2.9: (A) Synthetic waveform of the first overtone calculated from the inverted 1-D Vs profile and filtered in the 50s-200s period range; (B): Spectrogram $\mathrm{P}_1(\omega, t)$ of the relative weight of the first overtone in the synthetic test, as defined in equation 2.19. The regions with warmer colors in the figure represent larger weights in the F-T domain.

(Figure 2.10). In order to automate the process, we arbitrarily define the threshold values at 10 for the fundamental mode and 2 for higher modes. For each mode, only periods with reliability parameters larger than the threshold will be kept. As is shown in the synthetic test results, the fundamental mode and the first overtone have high reliability at all periods. The second overtone is also above the threshold at most periods but the third and fourth higher modes only have a short range of reliable results. The fifth overtone cannot be determined reliably in the synthetic test, likely because it was not excited well at those frequencies by the employed seismic source.

Further synthetic tests were performed to verify whether our method is valid for uncorrelated noise (Fig. 2.11), and for fixed depth nodes, i.e. when the transdimensionality aspect of the software is turned off (Fig. 2.12). This transdimensionality test showed that

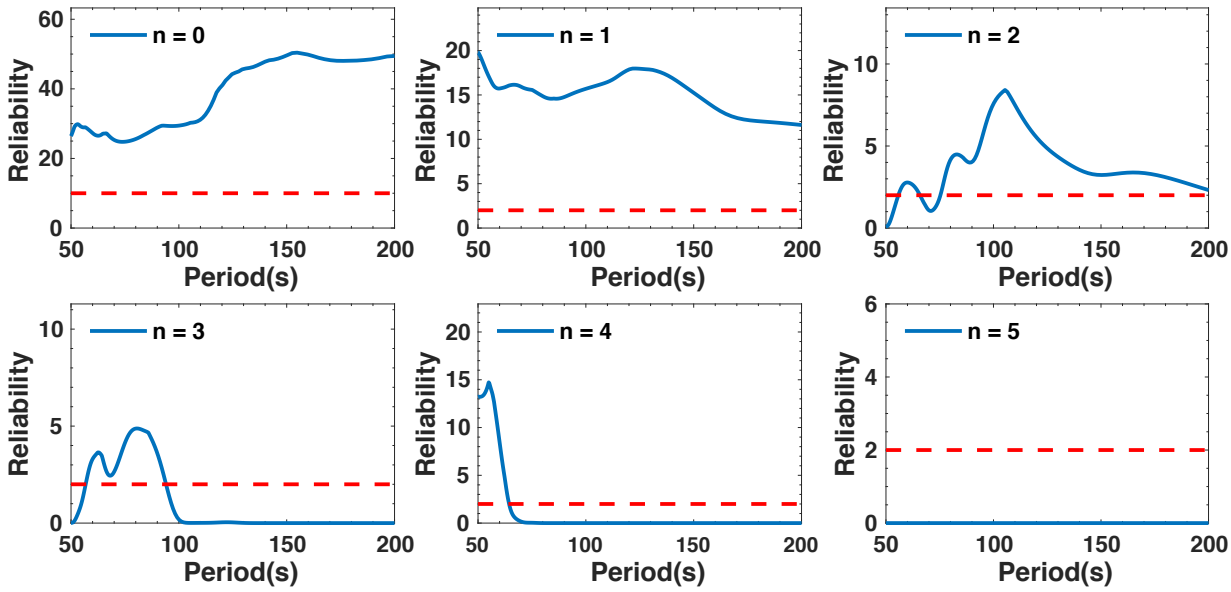

Figure 2.10: Reliability parameters as a function of frequency for the fundamental mode (n=0) and the first five overtones in the synthetic test. The thresholds we defined for each mode are denoted by the red dashed lines. Only periods at which the reliability parameters are above the threshold are kept as reliable inversion results.

for a parametrization with fixed number of parameters, similar to what was implemented by others [Yoshizawa and Kennett, 2002, 2004; Visser et al., 2007; Visser, 2008; Yoshizawa and Ekström, 2010], we can obtain phase velocity measurements with error bars that include the predictions of the input model, i.e. the "true" data. However, the mean phase velocities deviate from the true values, highlighting the importance of reporting proper uncertainties with the measurements. We also see that the mean phase velocities do not reproduce the input data as well as when the number of parameters is allowed to vary in the inversion. This is visible when comparing Figures 2.11 and 2.12. This is also true for the mean velocity model, which is not as close to the input model as the mean model of Figure 2.11. It should be noted, however, that when the dimension of the model is fixed, smooth parametrizations such as B-splines are more commonly employed [Yoshizawa and Kennett, 2002, 2004; Visser et al., 2007; Visser, 2008; Yoshizawa and Ekström, 2010], since they can more easily represent smooth 1-D velocity variations with a limited number of nodes. In addition, we note that the computational time when the transdimensionality is turned on was not very different from when it was turned off.

We additionally tested the effect of the data noise level by underestimating it (Fig. 2.13) and overestimating it (Fig. 2.14) compared to the input data. These figures demonstrate that the prior data noise level can have large influence on the inverted phase velocities as well as their estimated uncertainties: when the noise level is underestimated, the posterior uncertainties on the estimated phase velocities become smaller but the input data are not well represented by those uncertainties as they lie outside (or close to) two standard deviations. When the noise level is overestimated, however, the uncertainties on the phase velocities are much larger but the mean is close to the input data. We therefore argue that overestimating the noise level leads to more reliable measurements, albeit with larger uncertainties, and reduces the possibility of overfitting the data.

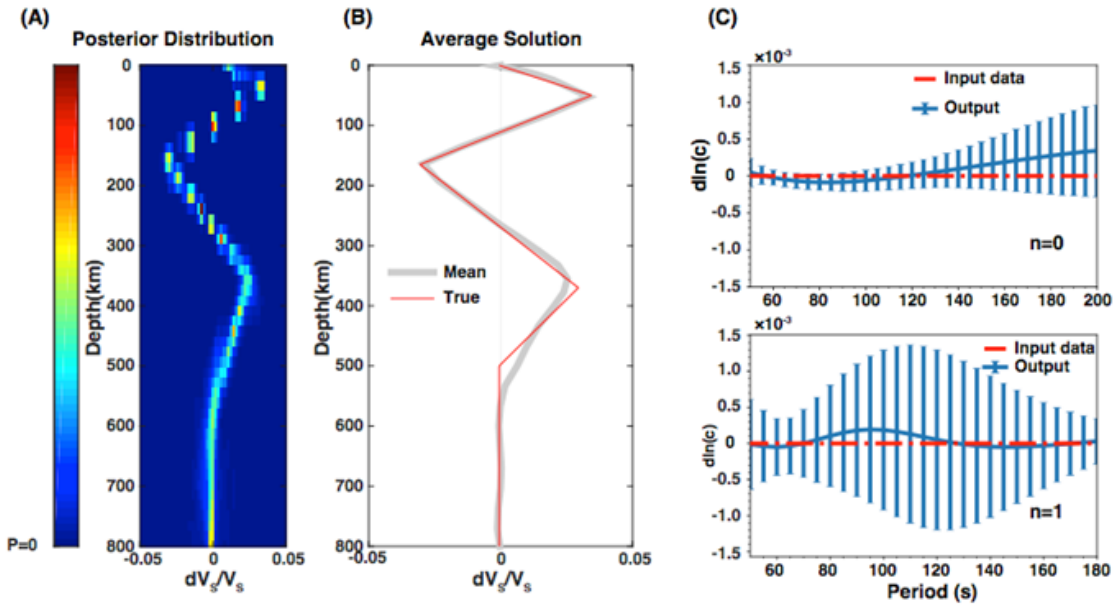

Figure 2.11: (A) V_S posterior distribution for a synthetic test with uncorrelated noise. Both noise levels and model dimensions are variable during the inversion. The red line in panel (B) is the true model. The grey curve is the mean of the distribution of panel (A). Panel (C) represents the inverted fundamental mode (top) and first overtone (bottom) phase velocity dispersion curves and uncertainties (blue) compared to the dispersion curve calculated for the true model (red). The uncertainties shown here correspond to two standard deviation obtained from the posterior distribution.

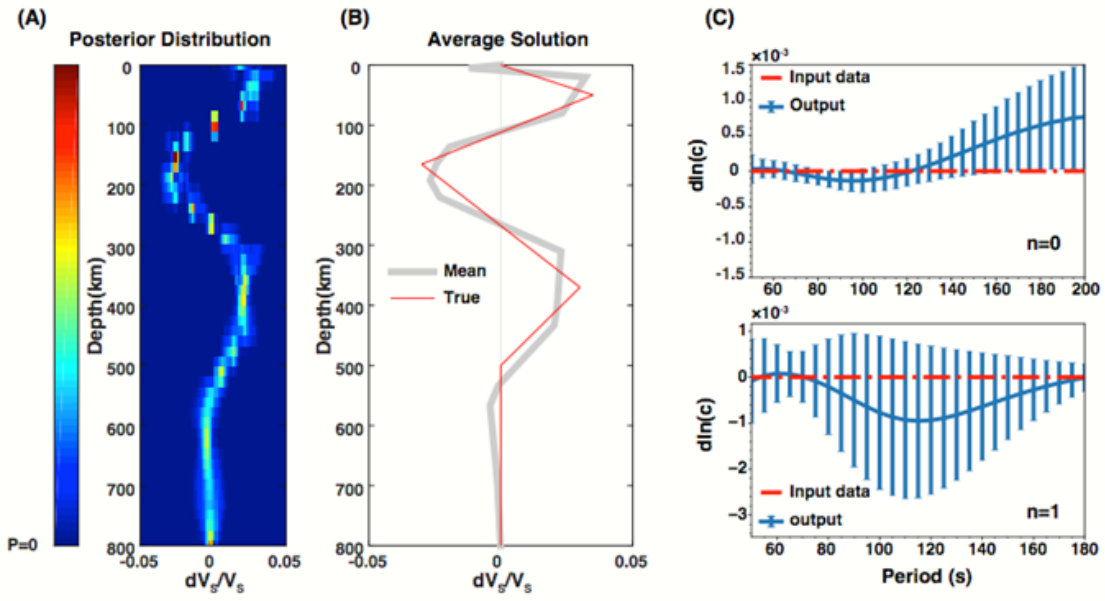

Figure 2.12: V_S posterior distribution (A) for the a synthetic test with uncorrelated noise and fixed depth parametrization. We fixed the number of depth nodes to nine and we fixed their depths at 5 km, 20 km, 80 km, 140 km, 210 km, 310 km, 430 km, 550 km and 690 km. Only the noise level and amplitude of dV_S/V_S are allowed to vary during the inversion. The red line in panel (B) is the true model and the grey curve is the mean of the distribution of panel (A). Panel (C) represents the inverted fundamental mode (top) and first overtone (bottom) phase velocity dispersion curves and uncertainties (blue) compared to the dispersion curve calculated for the true model (red). The uncertainties shown here correspond to two standard deviation obtained from the posterior distribution.

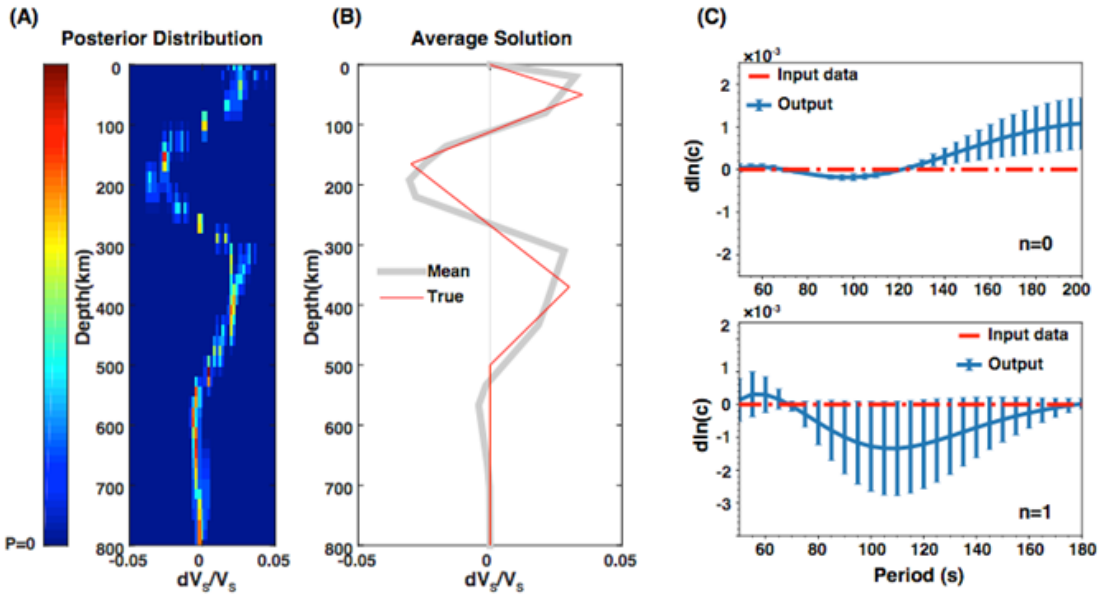

Figure 2.13: (A) V_S posterior distribution for the a synthetic test with fixed, uncorrelated and underestimated noise and fixed depth parametrization. The transdismentionality of the algorithm was turned off and the depths of the nodes were the same as in Fig. 2.12. We assumed the fixed noise level was underestimated in the inversion by a factor 100 compared to the synthetic input data noise level. Only the amplitude of dV_S/V_S was allowed to vary during the inversion. The red line in panel (B) is the true model and the grey curve is the mean of the distribution of panel (A). Panel (C) represents the inverted fundamental mode (top) and first overtone (bottom) phase velocity dispersion curves and uncertainties (blue) compared to the dispersion curve calculated for the true model (red). The uncertainties shown here correspond to two standard deviation obtained from the posterior distribution.

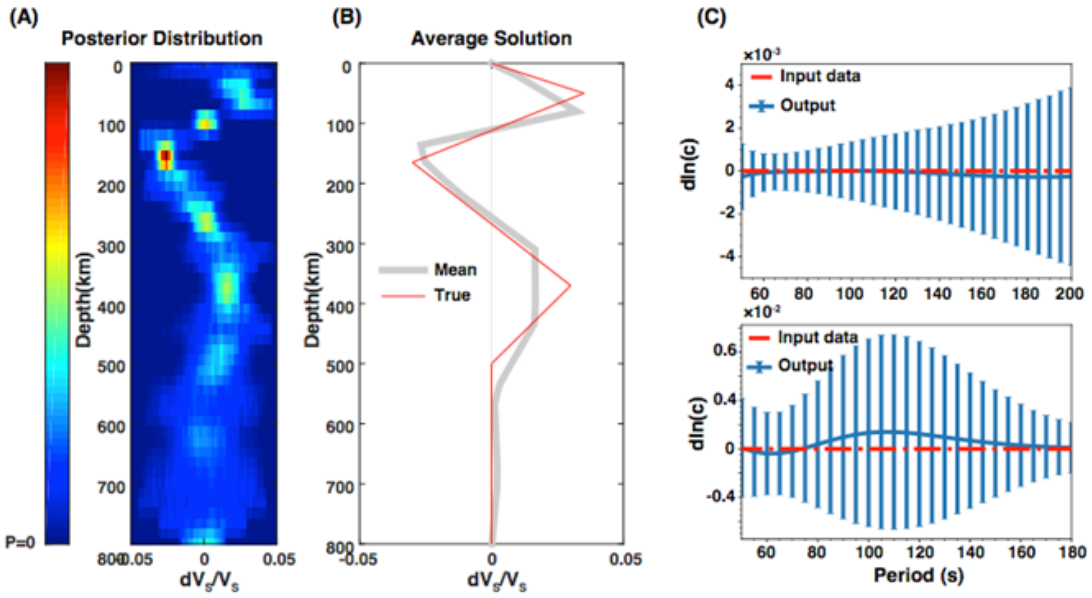

Figure 2.14: (A) V_S posterior distribution for the a synthetic test with fixed, uncorrelated and overestimated noise and fixed depth parametrization. The transdismentionality of the algorithm was turned off and the depths of the nodes were the same as in Fig. 2.12. We assumed the fixed noise level was overestimated in the inversion by a factor 10 compared to the synthetic input data noise level. Only the amplitude of dV_S/V_S was allowed to vary during the inversion. The red line in panel (B) is the true model and the grey curve is the mean of the distribution of panel (A). Panel (C) represents the inverted fundamental mode (top) and first overtone (bottom) phase velocity dispersion curves and uncertainties (blue) compared to the dispersion curve calculated for the true model (red). The uncertainties shown here correspond to two standard deviation obtained from the posterior distribution.

2.9 Real Data Test

In this section we present the phase velocity inversion results for two paths across western and eastern Australia. Figure 2.15 shows the locations of the events and stations. Both selected events have depths larger than 50 km. The source parameters of the two events are listed in Table 2.2. The epicentral distance for the western path is 4,036 km, and for the eastern path is 4,012 km. Although a non-linear inversion method is used here to calculate phase velocities from the S-wave velocity models, it can still be preferable to use a reference model that is as close as possible to the true structure of the region studied. This is mainly because our method to calculate the synthetic seismograms is not fully non-linear for computational reasons (see discussions in previous sections). The forward modeling part of the algorithm was linearized, and we search for model parameters dV_S/V_S between -5% and 5% around a reference model in order to reduce errors caused by the linearization. Here, we adopted the 3-D shear-velocity model of Debayle et al. [2016]. We averaged the V_S profiles extracted from the reference model along each station-event pair, and used this average as a reference model for the specific 1-D path considered. The prior data noise level was a uniform distribution between 1 and 500 nm/s for each time window.

The posterior distribution of dV_S/V_S models for the western Australia path is shown in Figure 2.16, followed by the number of parameters and data noise distributions (Figure 2.17), the waveform fit (Figure 2.18), the reliability analysis (Figure 2.19), and the estimated phase velocity dispersion curves (Figure 2.20). The inverted dV_S/V_S structure (Figure 2.16) displays a modest positive deviation from the reference model between 50 km and 200 km depth as well as below 400 km depth. The uppermost positive anomaly is consistent with a thick lithosphere as expected in a cratonic area. The number of velocity parameters required by the data is around four, which demonstrates the parsimony of the algorithm, and the posterior data noise distributions have relatively narrow Gaussian distributions with a standard deviation much lower than the assumed prior noise level. Overall, the fundamental

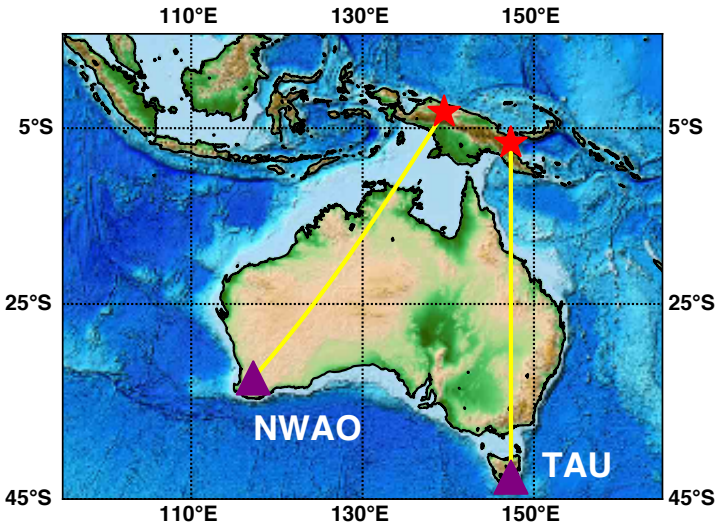

Figure 2.15: Locations of events (stars) and stations (triangles) used for the real data test. The yellow lines show the great circle paths from sources to receivers for western and eastern Australia.

mode in the first window (5-10 mHz) is the lowest, followed by the higher modes window.

The synthetic waveform calculated from the mean velocity model fits the real data well (Figure 2.18), and we see that phase velocities for the fundamental mode has reliability parameters larger than the predefined threshold, 10, at all periods considered (Figure 2.19). For the first overtone, the reliable measurements are in the period range 92 s-200 s, with the threshold set at 2. Similarly, the second overtone phase velocities were estimated to be reliable in the period range 58 s-148 s. The reliability parameters of the third overtones is between 60 s-88 s. Finally, a small portion (50 s-57 s) of the fourth overtone was found to be reliable.

For the eastern Australia path, we repeated the procedure described above. The results are shown in Figs. 2.21-2.25. We see a strong positive V_S anomaly compared to the reference model at about 60 km depth and a negative V_S anomaly at 120-220 km depth. Our solution can be interpreted as a thin lithosphere (about 100 km thick) with slightly positive velocity

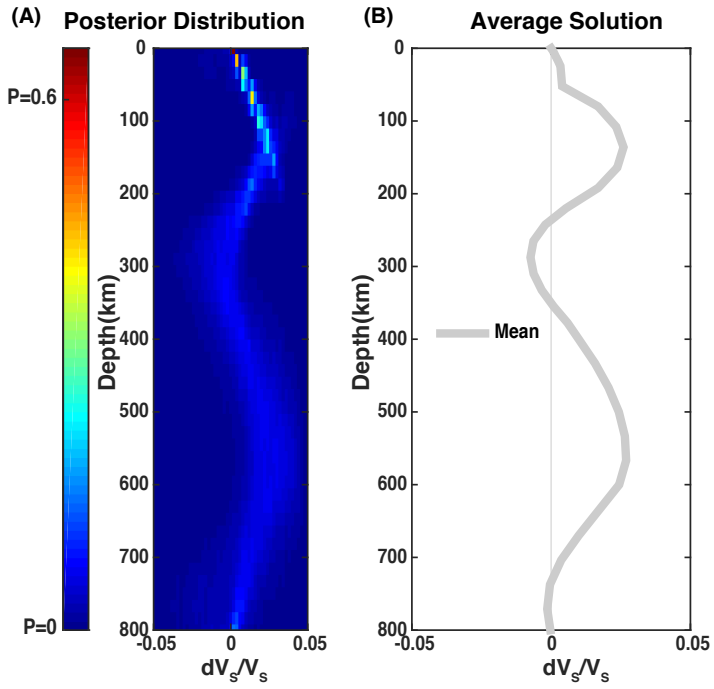

Figure 2.16: (A) Posterior distribution of relative velocity perturbations with respect to Debayle et al. [2016] for the western Australia path; (B) Resulting mean dV_S/V_S model

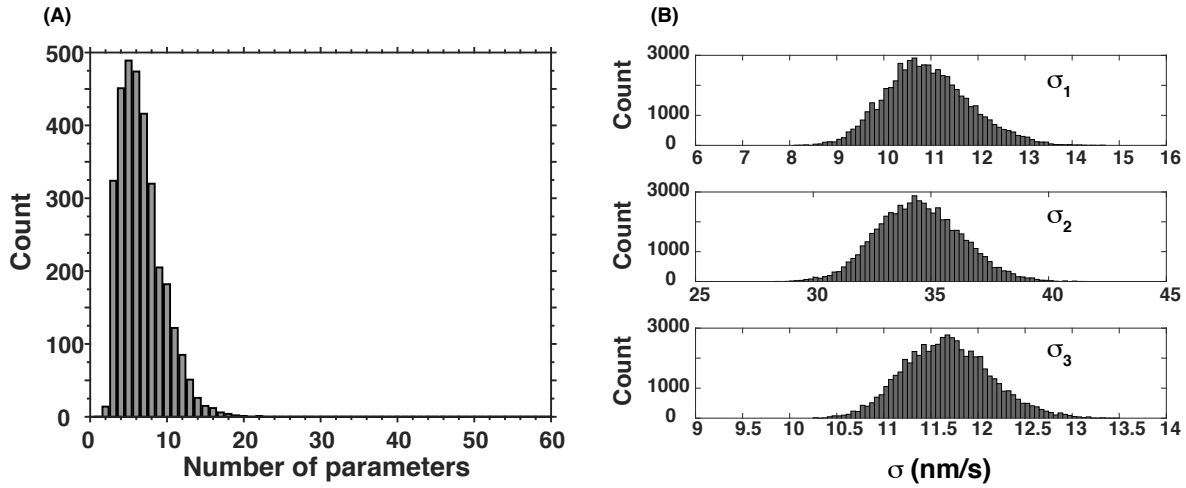

Figure 2.17: (A) Posterior distribution of the number of velocity parameters for the western Australia path; (B) Posterior data error distribution for each of the three time windows. Note the different scales on the horizontal axes.

anomalies and a low velocity layer that may coincide with the asthenosphere (Fig. 2.26(B)), consistent with Phanerozoic geological features and with previous studies [Yoshizawa and Kennett, 2015]. It should also be noted, however, that our V_S solutions are not directly comparable with 3-D models, but rather can be regarded as a 1-D approximation of the real Earth structure along the selected path. Figure 2.22 shows that the number of parameters required to fit the data is between four and eight and the data noise level is clearly the lowest for the fundamental mode filtered between 5 mHz and 10 mHz (window 1). Overall the noise level is much higher for the eastern Australia path than for the western Australia path.

With Figure 2.24, we show that the fundamental mode and the first four overtones can be reliably retrieved: the fundamental mode has high reliability at 50 s-150 s. The first and second overtones have large reliability at longer periods (60 s-200 s, 54 s-200 s). The reliable periods for third and fourth overtones are 50 s-83 s and 50 s-61 s, respectively. Measurements for the modes and periods estimated reliable are shown in Fig. 2.25. This figure also displays

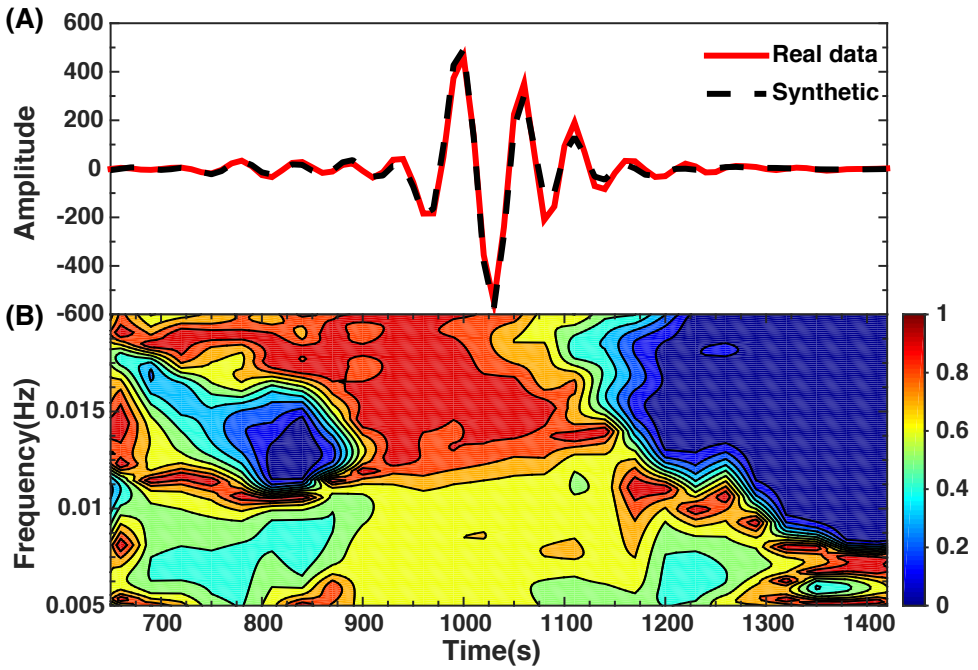

Figure 2.18: The same as Figure 2.7 but for the western Australia path. (A) Real data and synthetic seismogram filtered in the 50 s-200 s period range and calculated using the inverted mean model of Figure 2.16; (B) F-T analysis of the misfit as defined in equation 2.18.

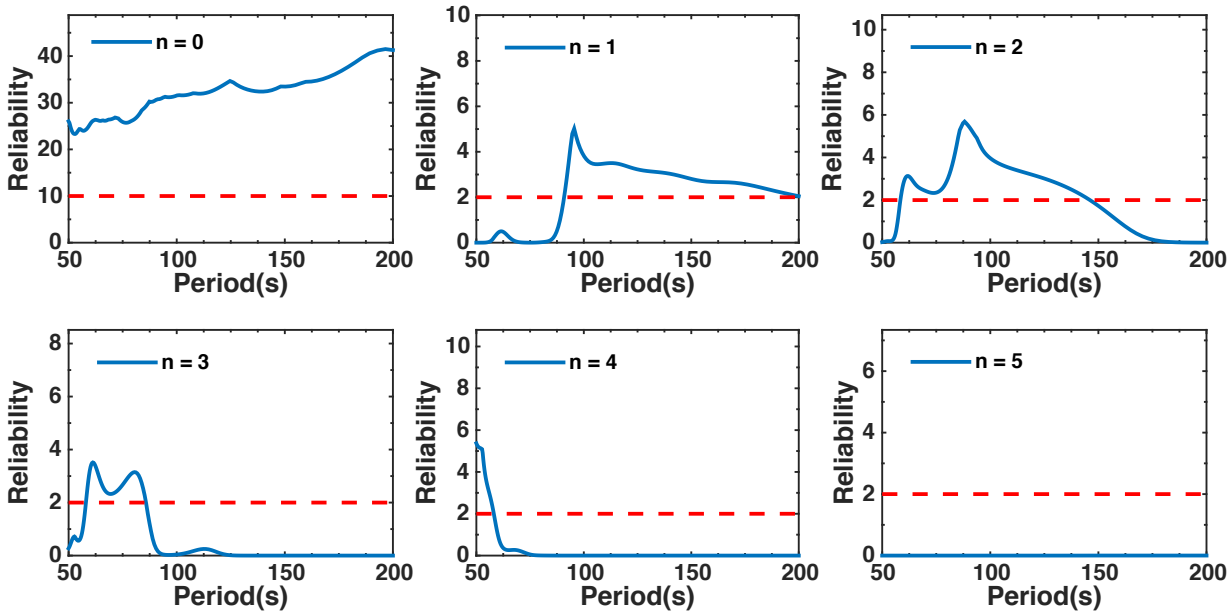

Figure 2.19: Reliability parameters for the western Australia path. See Figure 2.10 for details.

phase velocities measured using S40RTS [Ritsema et al., 2011] as a reference instead of the Debayle et al. [2016] model to test the dependence of our method upon the reference model. The results show no significant dependence on the reference model. The reliability tests were not strongly affected by the reference model either (not shown here).

The mean absolute V_S model were also plotted for paths and compared to PREM (Figure 2.26(A)). This figure shows a clear difference between the eastern and western paths in the top 200 km, beyond which the two velocity profiles become more similar.

In this study we used the centroid moment tensor from the GCMT catalog. We acknowledge, however, that for some paths dispersion measurements performed using waveform modeling at single stations can be affected by uncertainties in source parameters. While quality control can be applied to filter out unreliable earthquake sources by comparing source parameters from different earthquakes in the same region or by comparing different source

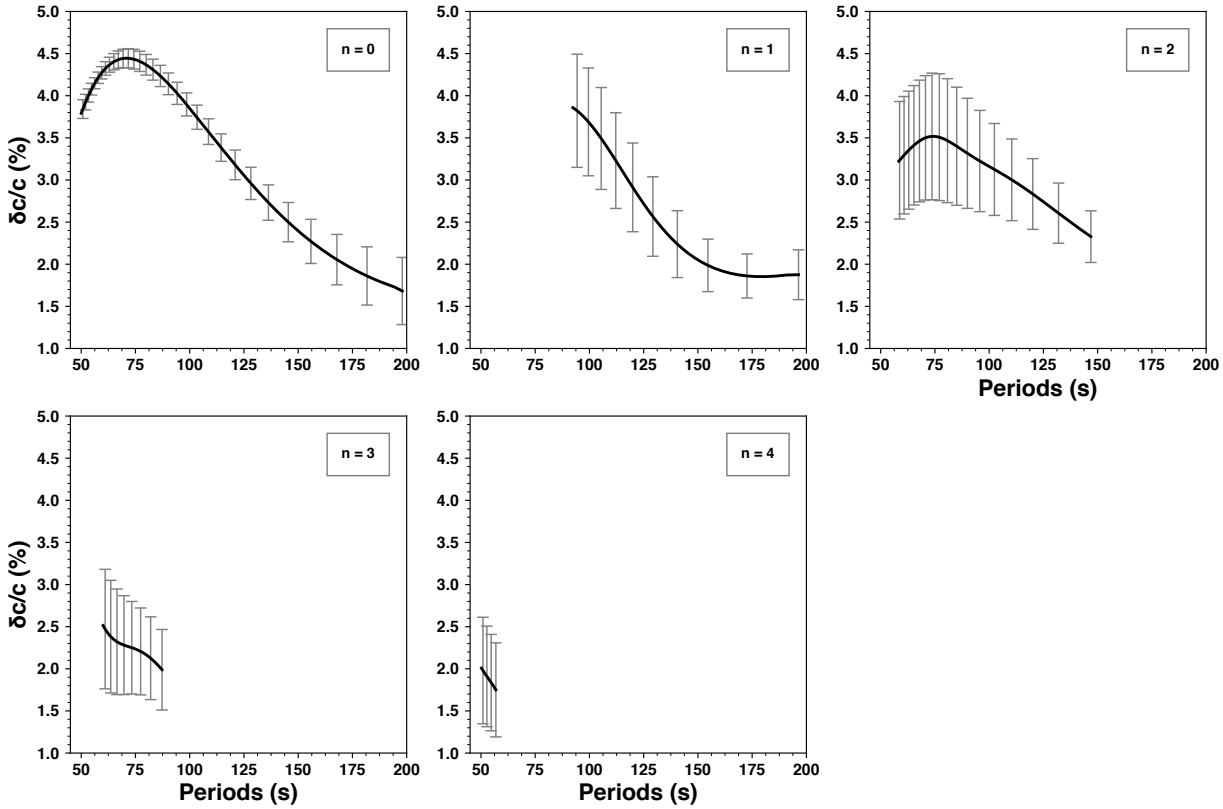

Figure 2.20: Measured phase velocities anomalies for the western Australia path and the modes and periods that were estimated to be reliable (Fig. 2.19). The measurements were converted from perturbations with respect to the average version of the 3-D reference model into perturbations with respect to PREM. Uncertainties correspond to 2σ.

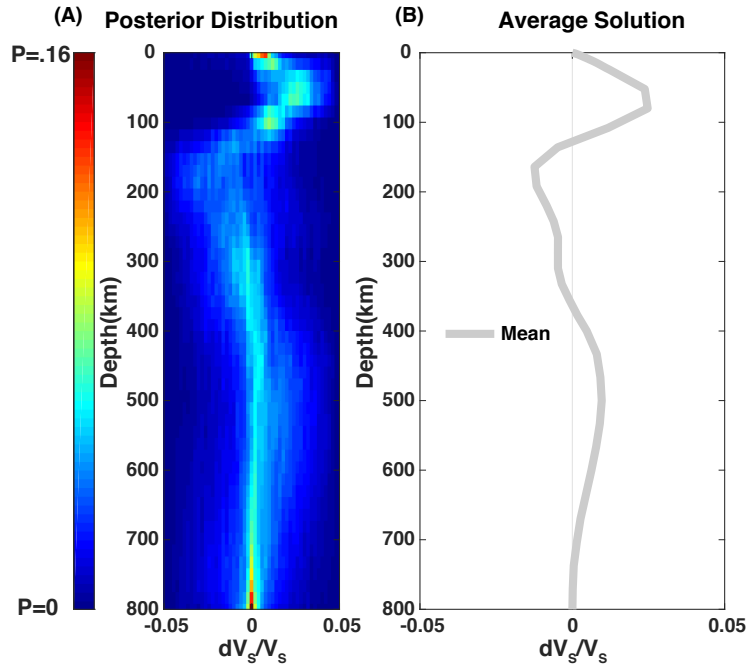

Figure 2.21: Posterior ensemble of solutions for the eastern Australia path. See Fig. 2.4 for details.

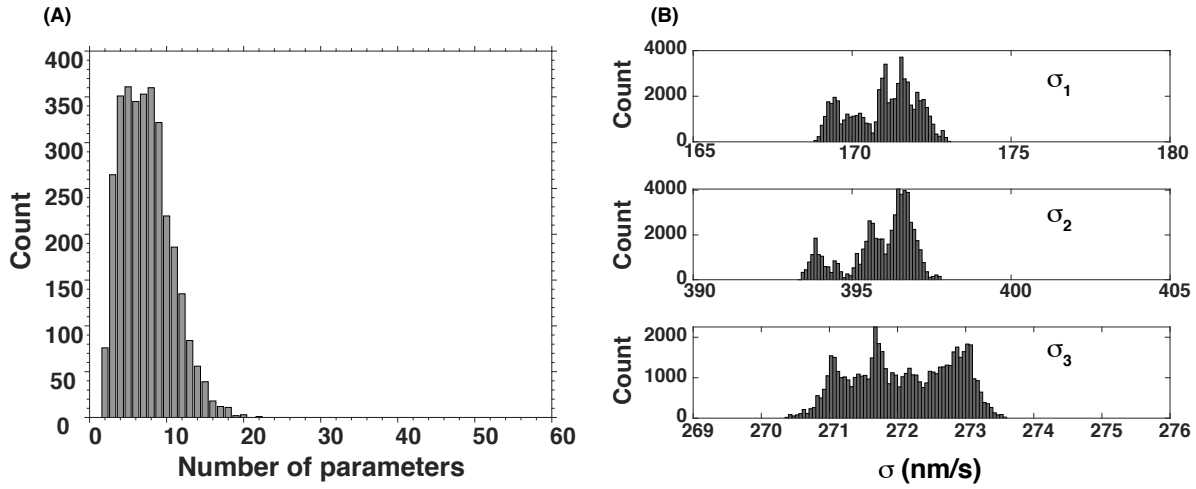

Figure 2.22: (A) Posterior ensemble for the number of parameters for the eastern Australia path; (B) Posterior noise distribution for each the the three time windows. Note the different horizontal scales.

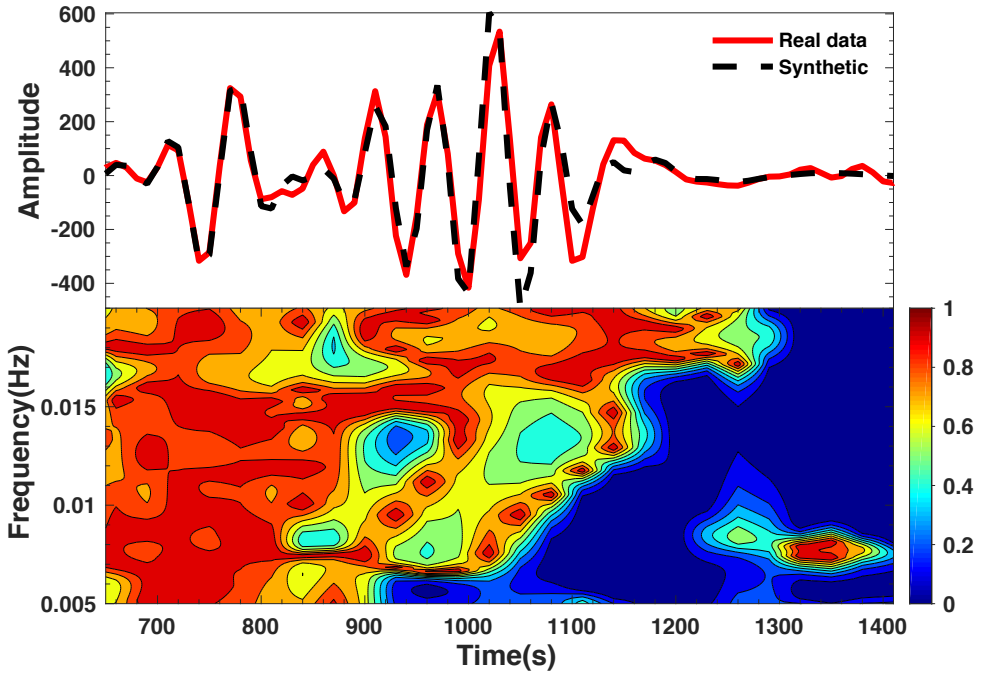

Figure 2.23: Real data and synthetic seismogram filtered in the 50 s-200 s period range and calculated using the inverted mean model of Figure 2.21 (top); F-T analysis of the misfit as defined in equation 2.18 (bottom).

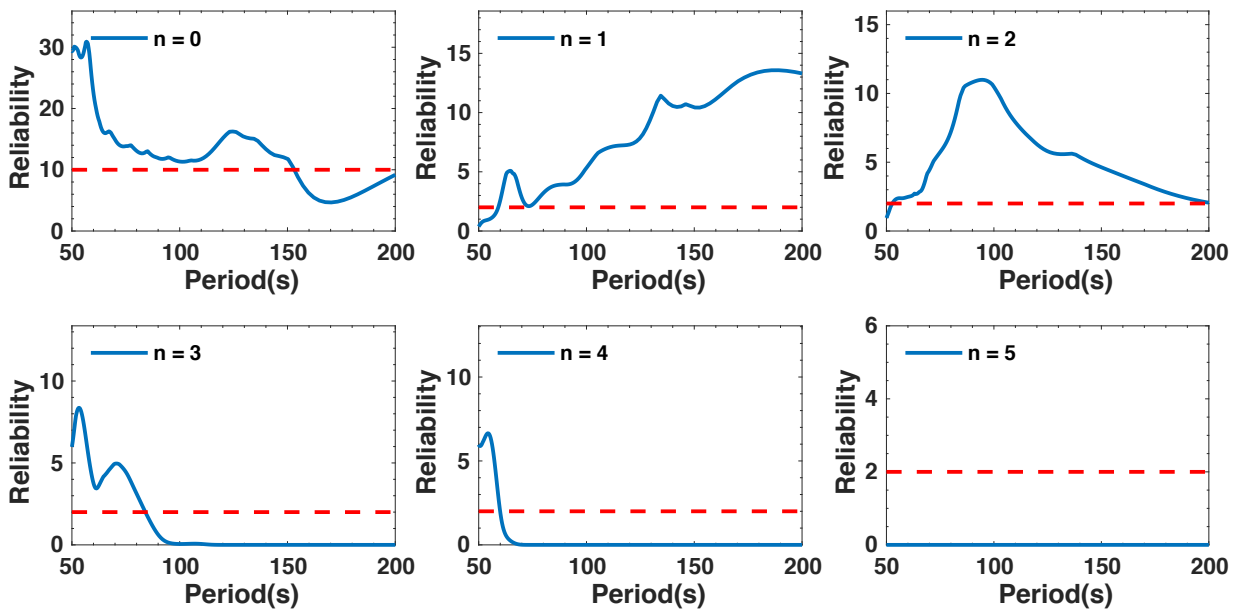

Figure 2.24: Reliabiliy test for the eastern Australia path. See Fig. 2.10 for details

catalogues, joint inversions of structure and source parameters are preferable [Valentine and Trampert, 2012]. A future implementation of our technique (see Chapter 4) will include source parameter among the unknowns in order account for possible errors in the source parameters.

2.10 Summary

We applied the rj-MCMC technique to the non-linear problem of measuring fundamental and higher mode Rayleigh wave phase velocity dispersion using waveform modeling. The use of higher mode surface waves in depth inversions of seismic velocities and anisotropy is very valuable as it increases the vertical resolution of tomographic models in the upper mantle and transition zone. The forward problem consisted in calculating synthetic seismograms by normal mode summation using computer program Mineos and a linearized approximation to the calculation of normal mode eigenfrequencies. The rj-MCMC method enabled us to

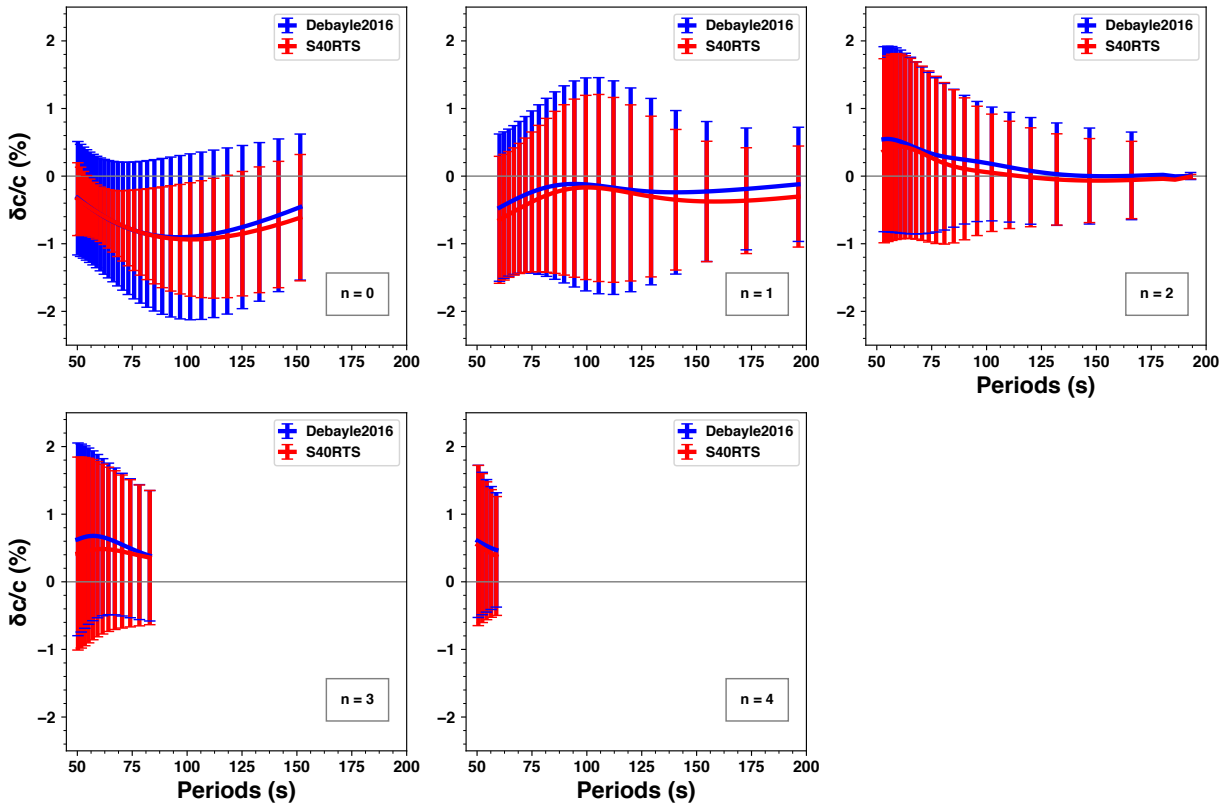

Figure 2.25: Reliable measured phase velocities expressed as perturbations with respect to PREM for the eastern Australia path and the modes and periods that were estimated to be reliable (Fig. 2.24). The red curve represents measurements performed using the model of Debayle et al. [2016] as a reference model. The blue curve are measurements performed using model S40RTS of Ritsema et al. [2011] as reference. The phase velocities were converted from perturbations with respect to the 3-D reference model into perturbations with respect to PREM. Uncertainties correspond to 2σ.

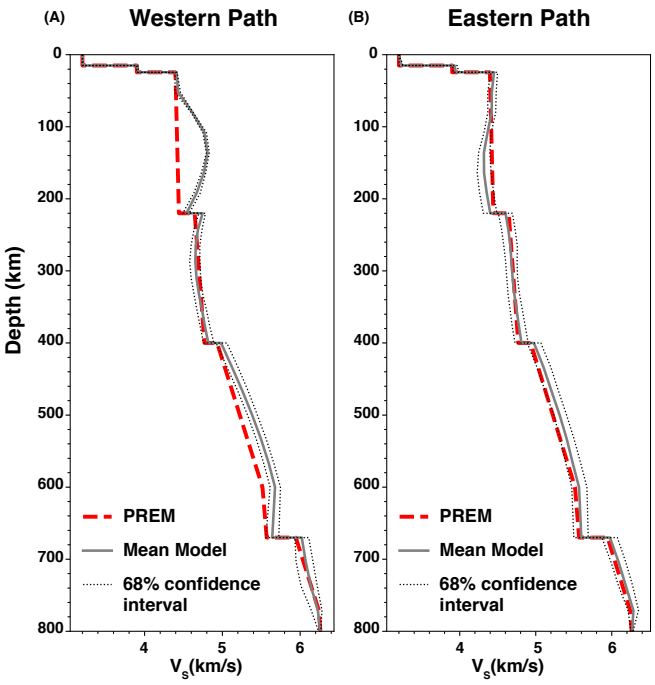

Figure 2.26: The mean V_S solution and one standard deviation for the western (A) and Eastern (B) Australia paths compared to PREM.

find a distribution of 1-D shear velocity models that best fit the waveform and represent the dispersion of multiple modes along a specific source-receiver path. An advantage of this technique is that the algorithm can decide how much data noise is needed to fit the data without overfitting them. The posterior noise distributions can then be used as an indicator of the quality of the waveform fit within each frequency-time window. The data noise was thus treated as an unknown and different noise levels were applied to the different time windows considered. The resulting distribution of velocity models was used to calculate a posterior distribution of dispersion curves, from which a mean and standard deviation were obtained for different modes. A reliability analysis was then performed following Yoshizawa and Kennett [2002] to assess which higher modes were reliably separated.

With synthetic tests, we showed that the newly developed method presented here can extract the first four overtones and the fundamental mode at most periods between 50 and 200s, but that the third and fourth overtones can only be measured reliably at relatively short periods and in a narrower period band (50 s-100 s for n=3 and 50 s-60 s for n=4). Measurements performed for real data along two paths sampling western and eastern Australia showed similar results: the fundamental mode and first two overtones were measured reliably over most frequencies considered, and the third and fourth overtones could be extracted and their dispersion measured over a narrower frequency band and for shorter periods. We also demonstrated that the measured phase velocities do not strongly depend on the reference model used to calculate the initial seismogram.

While computationally intensive, the technique presented here has several advantages. It allows the user to sample the model space without requiring any explicit regularization other than specifying the bounds of the model space explored. In addition, because it is transdimensional and parsimonious, it can include data noise and the number of parameters among the unknowns without overfitting the data. It therefore lets the data themselves control the complexity of the solution. The reliability of mode separation can be assessed and quantitative uncertainties on the dispersion curves of each mode can be readily obtained.

This provides useful information on the data to seismologists who use these measurements to model three-dimensional seismic velocity and anisotropy. Our technique can also be easily adapted to include source parameters among the unknowns and perform joint inversions of model structure and source parameters to account for the effect of source uncertainties on the measured phase velocities. We also note that the phase velocities are not the only products of this technique. One could also envision using the resulting path-averaged velocity models and uncertainties and combine them to obtain a three-dimensional velocity model. Example of such applications will be shown in the following Antarctica Chapter.

CHAPTER 3

Antarctica

3.1 Introduction

The Antarctica plate can be divided into two distinct regions (Fig. 3.1): East Antarctica (EANT), which is believed to be a Precambrian craton separated from the supercontinent Gondwanaland, and West Antarctica (WANT), which is made up of a number of microplates dating back to the Jurassic [Dalziel, 1992; Anderson, 1999]. Between EANT and WANT, the Transantarctic Mountains (TAMs) extend from Northern Victoria Land to the Weddell Sea. The Gamburtsev Subglacial Mountains (GSM), located in the center of EANT, are part of a subglacial mountain range that is not well understood due to poor data access. The lack of direct geological samples, for instance, makes it difficult to determine the age and origin of the GSM [Shen et al., 2018]. In WANT, lies the West Antarctic Rift system (WARS), a striking geological feature that experienced extension during most of the Cenozoic [e.g. Granot et al., 2010]. The thermal anomaly caused by this extension is likely still present in the WANT asthenosphere [An et al., 2015a]. WANT is also characterized by the Marie Byrd Land (MBL), which is associated with volcanism that might have resulted from the rifting, but that may also reflect the signature of mantle plumes [e.g. Sieminski et al., 2003; Accardo et al., 2014; Emry et al., 2015].

Early surface wave dispersion data analyses over Antarctica [e.g. Press and Gilbert, 1959; Evison et al., 1960; Kovach and Press, 1961] showed that EANT is characterized by phase velocities that are usually representative of stable continents and a relatively deep Moho

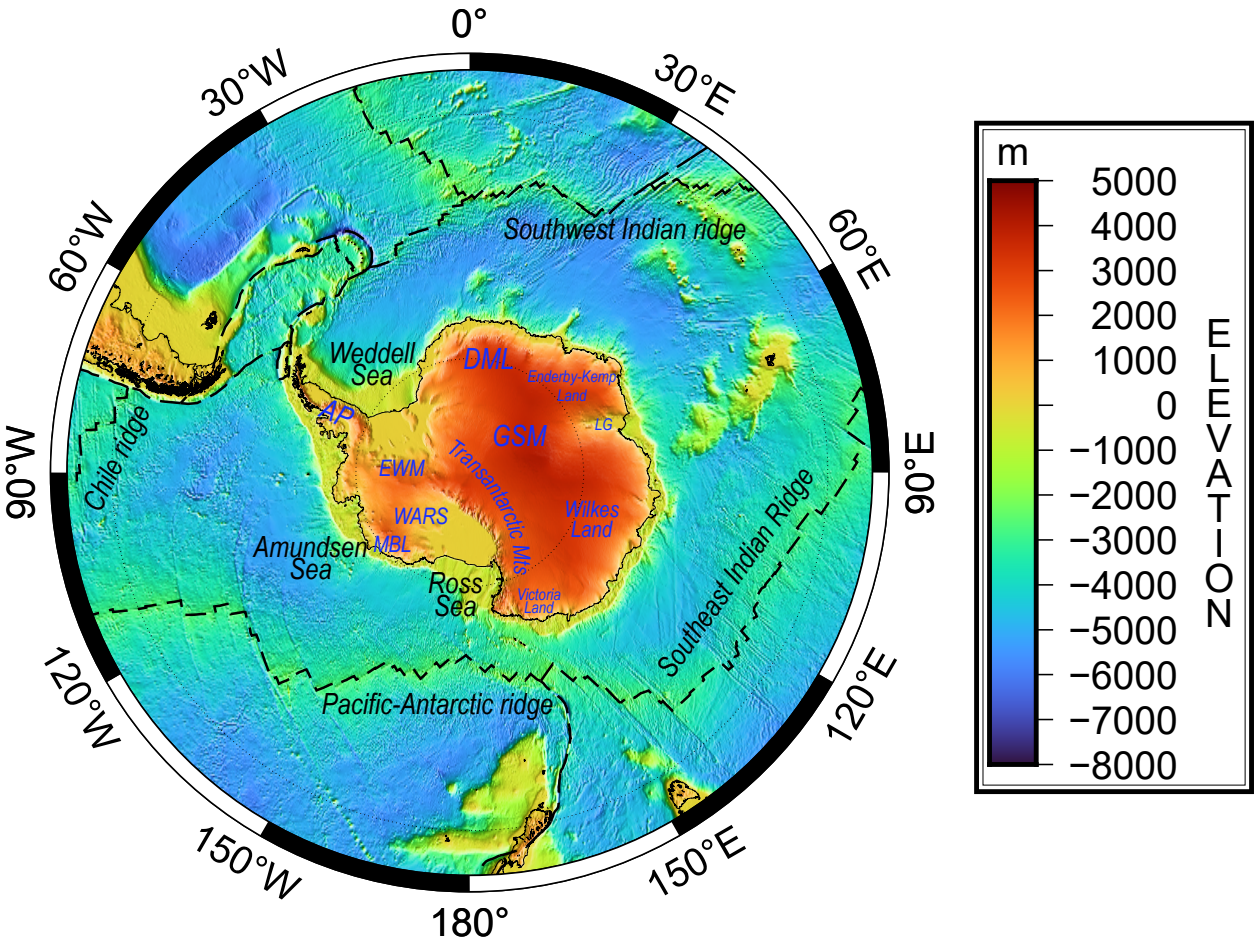

Figure 3.1: Topographic map of Antarctica. The bathymetry and topography of Antarctica and surrounding areas are based on model SRTM15+ [Tozer et al., 2019]. Abbreviations: AP = Antarctica Peninsula; DML = Dronning Maud Land; EMW = Ellsworth Whitmore Mountains; GSM = Gamburtsev Subglacial Mountains; LG = Lambert Graben; MBL = Marie Byrd Land; WARS = West Antarctic rift system.

of about 35 km depth, whereas WANT displays lower phase velocities and a thinner crust of about 25 km. Later studies [Dewart and Toksöz, 1965] found a slightly thicker crust in EANT of about 42 km, consistent with more recent receiver function results that show an average Moho of ∼40 km in the central EANT region and ∼55 km underneath the GSM [Hansen et al., 2009, 2010]. Roult et al. [1994] presented the first tomographic model of Antarctica and found a structure characterized by fast seismic velocities down to depths of about 250 km under EANT and low velocities under the ridges surrounding the Antarctic continent and under the TAMs. More recent global tomography studies [Ritsema and van Heijst, 2000b] as well as higher resolution regional seismic investigations of the region [Danesi and Morelli, 2001; Ritzwoller et al., 2001], have confirmed that the upper mantle beneath the EANT Craton is associated with high-velocity anomalies and a thick continental root of about 200 km, whereas WANT is characterized with relatively low velocities. In the first study using both fundamental and higher mode Rayleigh waves, Sieminski et al. [2003] also mapped a relatively slow structure that extends into the mantle transition zone beneath the western Ross Sea and might indicate the presence of a mantle plume.

These early continental-scale tomographic studies were, however, restricted by the limited number of seismic stations available. Seismic network coverage in Antarctica has increased significantly in the past two decades, enabling seismic imaging of higher resolution thanks to a much denser seismic raypath coverage. Recent fundamental mode phase [Heeszel et al., 2013] and group [An et al., 2015b] velocity surface wave studies show consistent results for EANT: the Gamburtsev Subglacial Mountains (GSM) is underlaid by a thick crust (∼60 km) and a seismically fast cratonic lithosphere reaching deeper than 200 km. Recently, Lloyd et al. [2020] performed the first full-waveform adjoint tomography study of Antarctica and estimated the depth of the craton to be between 250 km and 350 km. A number of recent regional seismic tomographic results have also shown relatively low seismic velocities under MBL extending through the upper mantle and possibly into the mantle transition zone [Hansen et al., 2014; Lloyd et al., 2015; Heeszel et al., 2016; Lloyd et al., 2020]. In contrast,

Emry et al. [2015] detected a local thinning of the transition zone, which may indicate high mantle temperatures, beneath neighboring areas of MBL rather than right below MBL.

Seismic anisotropy, which is the directional dependence of seismic wave velocity, offers a more complete description of Earth's elastic structure than isotropic velocities alone and can be used to constrain patterns of deformation in the mantle or crust [e.g. Becker et al., 2003; Yao et al., 2008; Karato et al., 2008; Volk et al., 2021]. Mantle seismic anisotropy can be detected using different types of observations such as shear-wave splitting [e.g. Silver and Chan, 1988; Long and van der Hilst, 2005], surface wave dispersion at the regional and global scales [e.g. Anderson, 1962; Montagner and Nataf, 1986; Ekström and Dziewonski, 1998; Trampert and van Heijst, 2002; Trampert and Woodhouse, 2003], free oscillation frequencies [Beghein and Trampert, 2006; Beghein et al., 2008; Moulik and Ekström, 2014], and anisotropic receiver function analyses [Ford et al., 2016]. Seismic anisotropy can manifest itself in different ways in seismic observations: (1) Transverse isotropy, in which case the elastic medium has one axis of symmetry. It is referred to as radial anisotropy if this axis is in the radial direction; (2) Azimuthal anisotropy, which describes the dependence of seismic wave speeds on the propagation azimuth. The shape-preferred orientation (SPO), sometimes called thin periodic layering, of isotropic structures with contrasting elastic properties, and the lattice-preferred orientation (LPO) of the crystallographic axes of elastically anisotropic minerals, are two different mechanisms that can yield observations of seismic anisotropy. LPO of olivine is the generally accepted explanation for observations of seismic anisotropy in the upper $\sim$250 km of the mantle as it has highly anisotropic crystals (about 18% shear-wave anisotropy) and is thought to be the dominant material at those depths [Karato and Wu, 1993]. In addition, most olivine deformation fabrics tend to align the fast axes of individual olivine crystals in the direction of shear. In the case of horizontal mantle flow induced by a vertical velocity gradient, the rule of thumb is thus that the fast direction for seismic waves reflects the flow direction. Observations of seismic anisotropy with axes aligned with present-day plate motion in region of low seismic velocities are therefore often interpreted

as the signature of current mantle flow in the asthenosphere [e.g. Gung et al., 2003; Marone et al., 2007; Beghein et al., 2014]. In the mantle lithosphere, it has been interpreted as the signature of fossil- or paleo-directions of deformation [e.g. Silver, 1996; Smith et al., 2004; Lebedev et al., 2008]. Seismic anisotropy has also been detected at greater depths, including in the mantle transition zone [e.g. Fouch and Fischer, 1996; Trampert and van Heijst, 2002; Visser, 2008; Yuan and Beghein, 2013; Auer et al., 2014; Yuan and Beghein, 2014; Huang et al., 2019] , top of the lower mantle [e.g. Lynner and Long, 2015; Ferreira et al., 2019], and in the lowermost mantle [e.g. Panning and Romanowicz, 2006; Lynner et al., 2014].

Roult et al. [1994] were the first to publish azimuthally anisotropic phase velocity maps for Antarctica by inverting dispersion curves obtained for fundamental mode Rayleigh waves in the period range 60 s to 300 s. They found that oceanic areas are associated with stronger azimuthal anisotropy than continents, but that the TAMs have relatively large anisotropy within the Antarctica continent. The fast directions of propagation in the oceans were found to be orthogonal to most of the ridges and to align with the direction of plate motion. However, the raypath coverage was very limited due to the small number of stations available, with only ∼400 paths covering the southern hemisphere. Sieminski et al. [2003] included azimuthal anisotropy in their fundamental and higher mode Rayleigh wave inversion, and found the presence of azimuthal anisotropy to be significant in the upper 200 km underneath the Antarctica continent, with maximum amplitudes at 100 km depth. Ritzwoller et al. [2001] studied radial anisotropy in the region and reported an average of ∼4 % anisotropy for Antarctica and surrounding areas, with slightly stronger amplitudes in WANT than in EANT. Additionally, O'Donnell et al. [2019] imaged WANT with ambient noise tomography in the period range 8 s to 25 s and detected $V_{SH} > V_{SV}$ in the crust across the region. The peak amplitude was observed in the Ellsworth–Whitmore Mountains (EWM). Lloyd et al. [2020] also included radial anisotropy in their ANT-20 model, but they did not interpret the anisotropic structure retrieved due to the imbalance in sensitivity of V_{SV} and V_{SH}, and instead focused on the Voigt average wavespeed.

A number of shear-wave splitting studies have also investigated the anisotropic properties of Antarctica [e.g. Pondrelli and Azzara, 1998; Barruol and Hoffmann, 1999; Müller, 2001; Bayer et al., 2007; Reading and Heintz, 2008; Barklage et al., 2009]. With the new seismometers deployed for the POLENET/ANET project, Accardo et al. [2014] calculated and summarized results on azimuthal anisotropy for Antarctica from shear-wave splitting methods. They found that the fast axis directions for shear-waves do not align with the Absolute Plate Motion (APM), which may indicate that the uppermost mantle is subject to other secondary convection mechanism other than plate motion. They also found a radial pattern of fast axis direction around the MBL, which was interpreted as flow associated with a mantle plume head.

However, while shear-wave splitting analyses have good lateral resolution, they lack vertical resolution because measurements result from near-vertical paths and thus reflect the integrated effect of anisotropic structures encountered along the path. Surface waves provide constraints on seismic anisotropy with a much greater vertical resolution than body waves, though with a more limited lateral resolution of a few hundreds of kilometers at best. In this study, we took advantage of the increased number of available stations in Antarctica since the last higher mode study of the region [Sieminski et al., 2003] and we obtained a new azimuthally anisotropic V_{SV} model by jointly inverting fundamental and higher mode Rayleigh waveforms. The depth range of our model is 60 - 600 km, and azimuthal anisotropy was found to be significant only for depth above 300 km.

3.2 Data Selection

The seismic data coverage in Antarctica was boosted significantly by the deployment of recent temporary seismic networks, such as GAMSEIS [Wiens and Nyblade, 2007a], POLENET [Wiens and Nyblade, 2007b], TAMNNET [Hansen, 2012] and UKANET [Alex Brisbourne, 2016]. In this study, we considered all permanent and temporary seismic stations south of

-40 degrees latitude and collected data recorded between 2005 and 2020. Because the lateral resolution of the models is limited by the wavelength of the data, having measurements at nearby stations would not improve resolution. The minimum interstation distance was thus set at 75 km so that only one station from very dense arrays is used. We obtained the event source parameters from the GCMT catalog [Dziewonski et al., 1981; Ekström et al., 2012], and considered all events falling between -20 degrees to -90 degrees latitude and with moment magnitudes between 5.5 Mw and 7.0 Mw. The magnitude thresholds are chosen to avoid small magnitude earthquakes with low signal-to-noise ratio (SNR), as well as to avoid large magnitude earthquakes that cannot be approximated by the single point source assumption in waveform modeling. The station-event pairs were then selected based on the following criteria: 1) The epicentral distance should be between 30 degrees and 75 degrees. The lower bound guarantees that the higher mode waveforms separate adequately from the fundamental mode. We also avoided paths with long epicentral distances as they are more likely to be contaminated by scattering effects [Lebedev et al., 2005]; 2) The SNR of the recorded waveform should be higher than 10 for the 10-20 mHz frequency band, and higher than 5 for the 5-10 mHz frequency band. This criteria helped filter out records contaminated by noise. The lower frequency band had a lower threshold because it usually carries weaker energy compared to the higher frequency band; 3) At least 45% of the great circle paths had to fall within the Arctic Circle in order to ensure good constraints on the Antarctica Continent. The selected 578 events and 164 stations are shown in Fig. 3.2.

3.3 Method

The technique employed in this study was originally designed to measure event-to-station phase velocity dispersion curves using waveform-fitting one-dimensional (1-D) velocity models sampled with a reversible-jump Markov Chain Monte Carlo (MCMC) approach [Xu and Beghein, 2019; Xu et al., 2021]. Dispersion curves obtained for a study area can then be

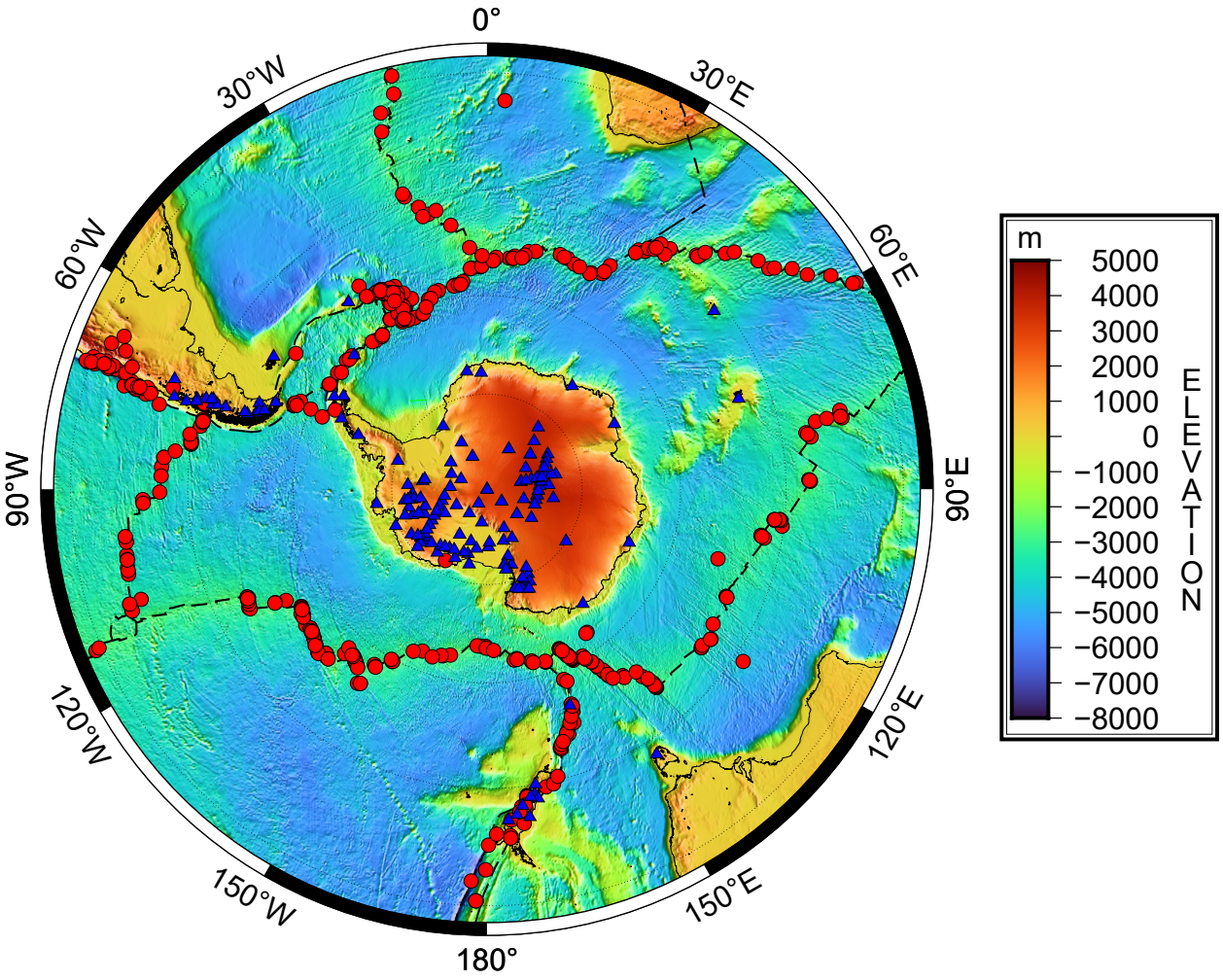

Figure 3.2: Maps of selected event locations (red circles) and stations (blue triangles). The background bathymetry and topography of Antarctica and surrounding areas are based on model SRTM15+ [Tozer et al., 2019].

jointly inverted to obtain phase velocity maps, which in turn can be inverted to obtain 3-D velocity and anisotropy models. This multi-step approach is commonly used in seismology and has the advantage of providing phase velocity maps, which is a compact way to represent the measurements and can be combined with other datasets for depth inversions. However, every time an inversion is performed, some form of prior information is introduced, either directly or indirectly via regularization, and it affects the solution. Here, we chose instead to use the path-averaged 1-D velocity models that result from the model space search used in our waveform fitting technique, and combine them to directly obtain a 3-D azimuthally anisotropic model of the upper mantle. The advantage is that it reduces the number of inversion steps and therefore the number of times user-specified prior information is introduced into the solution.

In this chapter, we briefly summarize our waveform fitting technique and explain the method used to perform the 3-D depth inversions as well as the construction of phase velocity maps. We then present and interpret both the resulting phase velocity maps and the 3-D anisotropy and velocity models.

3.3.1 MCMC Inversion Scheme and Waveform Fitting

In this section, we briefly summarize the framework of our inversion method and emphasize the improvements we made compared to the original paper. For more details, we refer the reader to Chapter 2.

We used a rj-MCMC method to obtain an ensemble of 1-D models that fit seismic waveforms in multiple frequency-time windows and that represent the dispersion of surface waves along the source-receiver path [Xu and Beghein, 2019; Xu et al., 2021]. One major advantage of model space search methods such as the rj-MCMC is that they enable direct uncertainty estimation of all model parameters. Another advantage of the trans-dimensional rj-MCMC algorithm is that it does not require a fixed model space dimension. Instead, it is designed to search for the optimal model space dimension during the sampling and discourages high

dimensional models to avoid overfitting issues [Malinverno, 2002]. In addition, unknown data noise can be part of the unknowns, reducing the risk of mapping noise into the models. Details about the implementation of rj-MCMC algorithm in our method have been summarized in our previous work [Xu and Beghein, 2019; Xu et al., 2021] and in Chapter 2 of this thesis. In this study, we sampled 480,000 models and used an ensemble of 1,600 models after burn-in period for each event-station pair. We used software package Mineos [Masters et al., 2011] to calculate synthetic seismograms for each model generated by the MCMC model space search and compared these synthetics with the recorded waveforms.

Synthetic seismograms can be calculated by normal mode summation [Dahlen, 1968]:

$$s(\omega) = \sum_m A_m(\omega) \exp\left[i\omega\Delta / c_m(\omega)\right] \tag{3.1}$$

where ω is the angular frequency of a mode m, $c_m(\omega)$ is its phase velocity, Δ is the epicentral distance, and A_m is the amplitude of the mode. While the calculation of one seismogram using this formulation is not particularly slow, the rj-MCMC sampling requires solving the forward problem hundreds of thousands of times for each path, which becomes very time-consuming when calculating normal mode eigenfunctions and eigenfrequencies at each iteration of the MCMC scheme. Instead, we chose to linearize the forward modeling by assuming that the perturbation relative to the reference model is small. Under this assumption, the perturbed eigenfrequencies $\delta\omega$ can be calculated as:

$$\delta \ln(\omega) = \int_0^a (\delta \ln V_S(r) K_{V_S}(r,\omega) + \delta \ln V_P(r) K_{V_P}(r,\omega) + \delta \ln \rho(r) K_\rho(r,\omega)) dr + \sum_d \delta d [K_d(\omega)]_-^+ \tag{3.2}$$

where $\delta \ln(\omega) = \delta\omega/\omega$, a is the radius of the planet, and V_P, V_S, ρ and d are P-wave velocity, S-wave velocity, density, and radius of discontinuities, respectively. K_{V_P}, K_{V_S}, K_ρ and K_d are the Fréchet derivatives [Woodhouse, 1980]. Here, shear-wave velocities were allowed to be perturbed by $[-5\%, +5\%]$ relative to the reference model. Unlike the methods presented in Chapter 2, which only considered the V_S term, here we also include the effects of V_P and ρ in the waveform simulation. The change in V_P and ρ are scaled to the change in

V_S because V_P and ρ only have secondary effects on the waveforms. For this, we followed the empirical scaling relationship from Yoshizawa and Ekström [2010]: V_P is scaled by a relationship that varies linearly with depth, with $\frac{dlnV_P}{dlnV_S} = 0.8$ at the surface and $\frac{dlnV_P}{dlnV_S} = 0.3$ at the core-mantle boundary, and ρ is scaled using a constant relationship, $\frac{dln\rho}{dlnV_S} = 0.3$, at all depths. Due to the intermediate-to-long period nature of the surface wave data analyzed here (50 s - 200 s), we do not expect to be able to resolve crustal structure independently from the mantle. We thus did not include perturbations in the depth of the crust-mantle boundary in our inversion scheme and used the Moho depths from CRUST1.0 [Laske et al., 2013] in our reference model.

The synthetic and the recorded waveforms were compared in multiple frequency-time windows (the selection criteria are summarized in Table 2.1) and the total misfit function was given by:

$$\text{Misfit}(\mathbf{m}) = \sum_{j=0}^{M} \frac{\sum_{i=0}^{N_j} (d_{j,i} - s_{j,i})^2}{\sum_{i=0}^{N_j} d_{j,i}^2} \tag{3.3}$$

where d and s denotes the recorded waveform and synthetic waveform, respectively. M is the number of frequency-time windows and N is the respective number of data points within each window. The normalization factor in the denominator guarantees that the misfits are independent of the absolute amplitudes of earthquakes and are used here for easier quality control.

Our waveform inversion requires good 1-D reference models in order for the MCMC sampling algorithm to converge within a reasonable amount of time, to reduce the errors introduced by the linearization of the forward modeling, and avoid cycle skipping. For each event-station pair, we thus calculated path-averaged reference models using CRUST1.0 [Laske et al., 2013] and 3-D global model 3D2018_08Sv [Debayle et al., 2016]. We saved the posterior distributions for both the along-path depth-dependent shear-wave velocities and the Rayleigh wave phase velocities, which allowed us to estimate the uncertainties on the 1-D V_{SV} profiles at different depths and the uncertainties on the phase velocity maps at different periods. Below, we present the phase velocity maps obtained as well as our 3-D velocity and

azimuthal anisotropy models.

3.3.2 Phase Velocity Maps and Inversion of 1-D Path-Averaged Models

Our trans-dimensional waveform fitting technique enables us to measure path-averaged phase velocity dispersion for fundamental and higher mode surface waves. In addition, a byproduct of this method consists in shear-wave velocity profiles between pairs of stations and events. We used the least squares (LSQR) method of Paige and Saunders [1982], as in Deschamps et al. [2008], to invert the path-averaged phase velocity measurements and obtain anisotropic phase velocity maps, and to invert the 1-D path-averaged velocity models and obtain a 3-D azimuthally anisotropic velocity model as explained below.

At each depth, the path-averaged slowness along great circle path l, $\beta^l(z)$, can be seen as the integral of the local slowness along the great circle path:

$$\frac{1}{\beta^l(z)} = \frac{1}{d}\int_l \frac{1}{\beta(z,l)}dl, \tag{3.4}$$

where z is the depth, l is the great circle path connecting the station and the event, and d denotes the epicentral distance along the great circle path. In a slightly anisotropic medium, the azimuthal variation of SV-wave propagating horizontally with velocity $\beta_v(z,\Psi)$ can be expressed as:

$$\beta_v(z,\Psi) = \beta_{v0}(z) + A_1(z)cos(2\Psi) + A_2(z)sin(2\Psi) + B_1(z)cos(4\Psi) + B_2(z)sin(4\Psi) \tag{3.5}$$

where Ψ denotes the azimuth. Provided good path coverage, the path-averaged velocities can be inverted to constrain the isotropic velocities β_{v0} and their anisotropic coefficients A_1, A_2, B_1, and B_2. A similar expression can be derived for surface wave phase velocities, c, at period ω:

$$c(\omega,\Psi) = c_0(\omega) + c_1(\omega)cos(2\Psi) + c_2(\omega)sin(2\Psi) + c_3(\omega)cos(4\Psi) + c_4(\omega)sin(4\Psi) \tag{3.6}$$

Both inverse problems can be written as:

$$\mathbf{d} = \mathbf{Gm} \tag{3.7}$$

where $\mathbf{m}$ represents the model parameters $(\beta_{v0}, A_1, A_2, B_1, B_2)$ in Eqn. 3.5 or C_0 - C_4 in Eqn. 3.6, $\mathbf{d}$ is the data, and $\mathbf{G}$ is a linear operator approximating the relationships between the data and the model parameters.

For shear-wave velocities, the amplitudes of anisotropy, Λ, and the fast directions of anisotropy, Θ, are given by:

$$\Lambda_{2\Psi}(z) = \sqrt{A_1(z)^2 + A_2(z)^2} \tag{3.8}$$

$$\Lambda_{4\Psi}(z) = \sqrt{B_1(z)^2 + B_2(z)^2} \tag{3.9}$$

$$\Theta_{2\Psi}(z) = \frac{1}{2}\arctan\left(\frac{A_2(z)}{A_1(z)}\right) \tag{3.10}$$

$$\Theta_{4\Psi}(z) = \frac{1}{4}\arctan\left(\frac{B_2(z)}{B_1(z)}\right) \tag{3.11}$$

Similarly, the equations for phase velocities are given by:

$$\Lambda_{2\Psi}(\omega) = \sqrt{c_1(\omega)^2 + c_2(\omega)^2} \tag{3.12}$$

$$\Lambda_{4\Psi}(\omega) = \sqrt{c_3(\omega)^2 + c_4(\omega)^2} \tag{3.13}$$

$$\Theta_{2\Psi}(\omega) = \frac{1}{2}\arctan\left(\frac{c_2(\omega)}{c_1(\omega)}\right) \tag{3.14}$$

$$\Theta_{4\Psi}(\omega) = \frac{1}{4}\arctan\left(\frac{c_4(\omega)}{c_3(\omega)}\right) \tag{3.15}$$

The study area was parameterized by a 2-D triangular grid at each depth for the $\beta_v(z, \Psi)$ inversions and at each period for the $c(\omega, \Psi)$ inversions. We manually tuned the grid spacing and set it at 300 km. The spatial distribution of the 2-D triangular grid for the study area is displayed in Fig. 3.3.

Regularization was introduced to solve the ill-posed geophysical problem and to avoid overfitting. Separate damping parameters are introduced for the isotropic terms, the 2Ψ terms, and the 4Ψ terms. For each of these terms, we used the L-curve method [Hansen, 1998] to select the optimal damping values. The L-curve describes the relationship between explained variances and the damping value. The preferred damping value is then chosen at

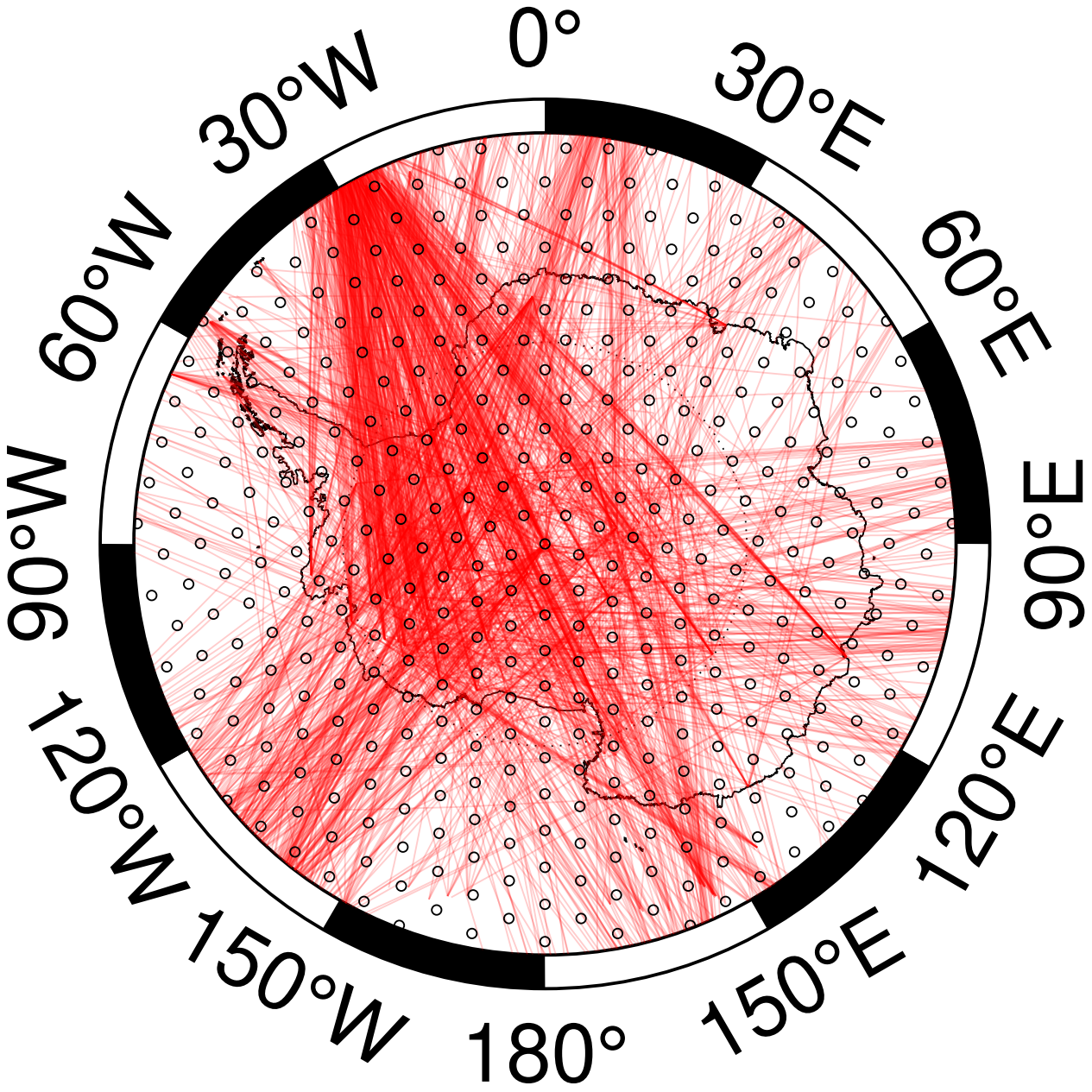

Figure 3.3: Ray-path coverage (red curves) and the 2-D triangular grid (black circles) used in the V_S modeling.

the "elbow" of the L-curve, which represents a good trade-off between variance reduction and model complexity. Different depths or periods are treated independently, and for each one of them, we start selecting the damping of the isotropic term. After the optimal regularization is selected for the isotropic term, we proceed with the 2Ψ terms, and finally the 4Ψ terms. Example of damping selection will be shown in the Result section. The significance of the 2Ψ and 4Ψ terms are determined via F-test and will be discussed in the Results section as well.

3.4 Results

3.4.1 1-D Path-Averaged Profiles

We ran MCMC samplings on all paths selected based on the criteria described in Section 3.2. Quality control was done by inspecting the converged noise levels in each of the time-frequency windows of Table 3.1. In this study, the maximum acceptable noise levels for windows 1, 2, and 3 are set at 0.3, 0.3, and 0.6, respectively. These thresholds were manually selected to balance dense path coverage and good individual path fitting, and only paths that satisfy all these conditions were kept. About 2,000 paths passed our rigorous quality control and the resulting ray-path coverage is shown in Fig. 3.4. For each of the selected paths, we calculated the standard deviations of the V_{SV} models at different depths and used these standard deviations to approximate the uncertainties at each path and depth. The inverse of the uncertainty estimates were then used as the path weights in the second inversion.

Fig. 3.5 shows the distribution of V_{SV} uncertainties at different depths. In general, the uncertainties increase with depth due to poorer resolution of our dataset at greater depths. For instance, most paths have uncertainties smaller than 40 m/s at 60 km and 150 km but at 600 km, the majority of the uncertainties falls in bins larger than 50 m/s. Shen et al. [2018] reported a standard deviation of 50 - 65 m/s from their Bayesian inversion on fundamental surface waves and receiver functions, which is roughly consistent with our

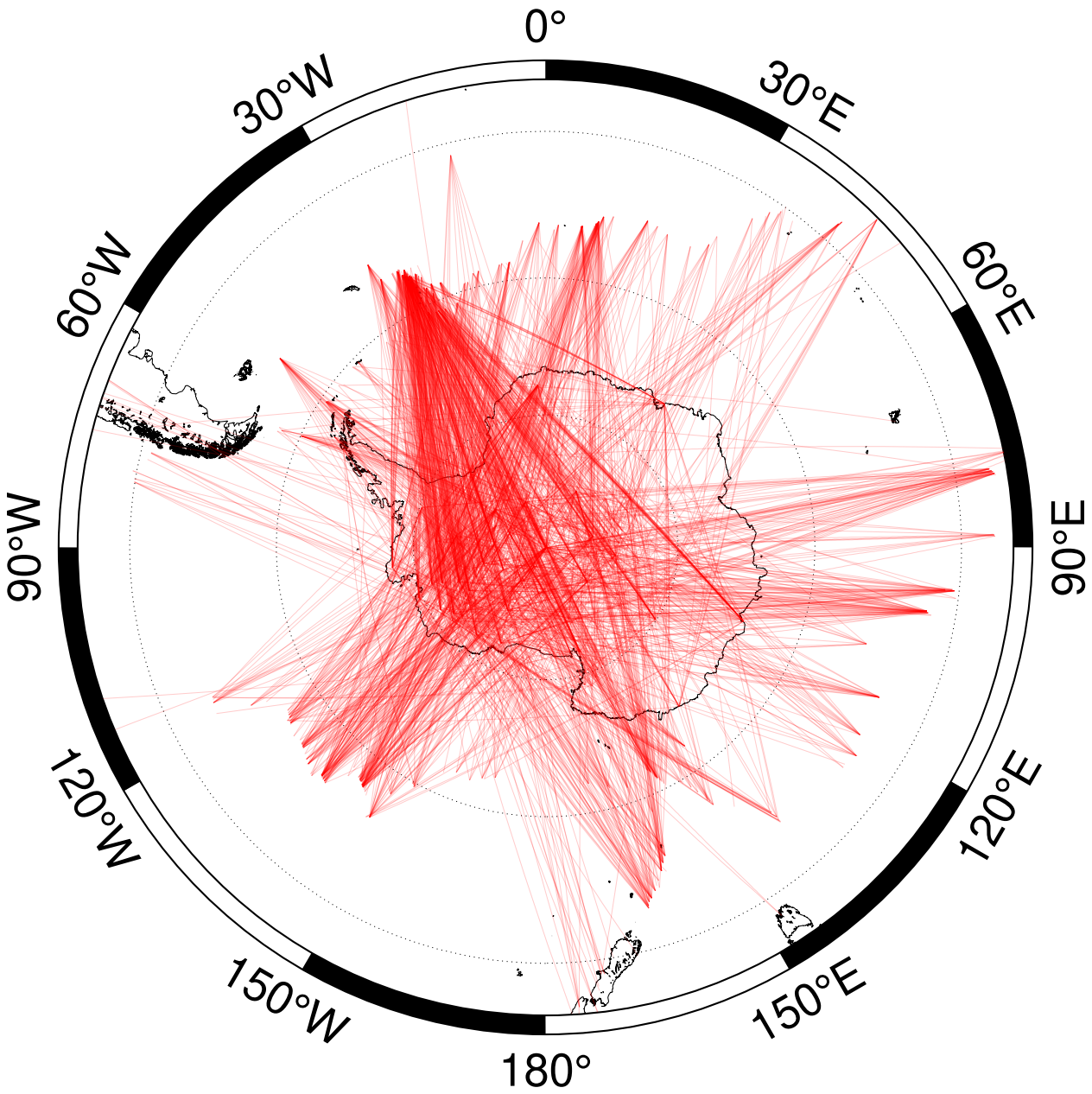

Figure 3.4: Ray-path coverage of all event-station pairs which pass all quality control steps.

Table 3.1: Selection of frequency-time windows. The first and second window indices correspond to the fundamental mode and the third window is for higher modes. The first and third windows share the same start time, which is determined by the S- or SS- wave arrival times. All other start/end times are determined by Δ/U, where Δ is the event epicentral distance and the values of the group velocities U are indicated in the table.

Window index	**Frequency(mHz)**	**Start**	**End**
1	5-10	S or SS	$U = 2.95\ km/s$
2	10-20	$U = 4.30\ km/s$	$U = 3.20\ km/s$
3	10-20	S or SS	$U = 4.30\ km/s$

path-specific uncertainties above 250 km. It should be noted, however, that our estimated standard deviations represent the uncertainties introduced in the waveform fitting step, while the results of Shen et al. [2018] consider both the data noises and depth trade-off in surface wave inversion. In order to further propagate the path-specific uncertainties into the second inversion, we used the inverse of the standard deviations as path weights. Paths with smaller uncertainties with be assigned a higher weight when inverted into a 3-D V_{SV} model.

3.4.2 Significance of the Anisotropy

As shown in Fig 3.6, the variance reduction increases as more parameters are included in the inversion. However, some of the parameters may not necessarily be constrained by the data. In order to test if the anisotropic terms in this study are statistically significant, we adopted the method of Trampert and Woodhouse [2003]. We defined a reduced χ^2 as:

$$\chi^2 = \frac{1}{N-M}(\mathbf{d}-\mathbf{Gm})\mathbf{C_d^{-1}}(\mathbf{d}-\mathbf{Gm}) \tag{3.16}$$

where N is the number of data points and M is the trace of the resolution matrix $\mathbf{R}$. $\mathbf{d}$ is the data vector, $\mathbf{m}$ is the model vector and $\mathbf{G}$ is matrix describing the relationships between the data and the model parameters. $\mathbf{C_d}$ is the data covariance matrix. The resolution

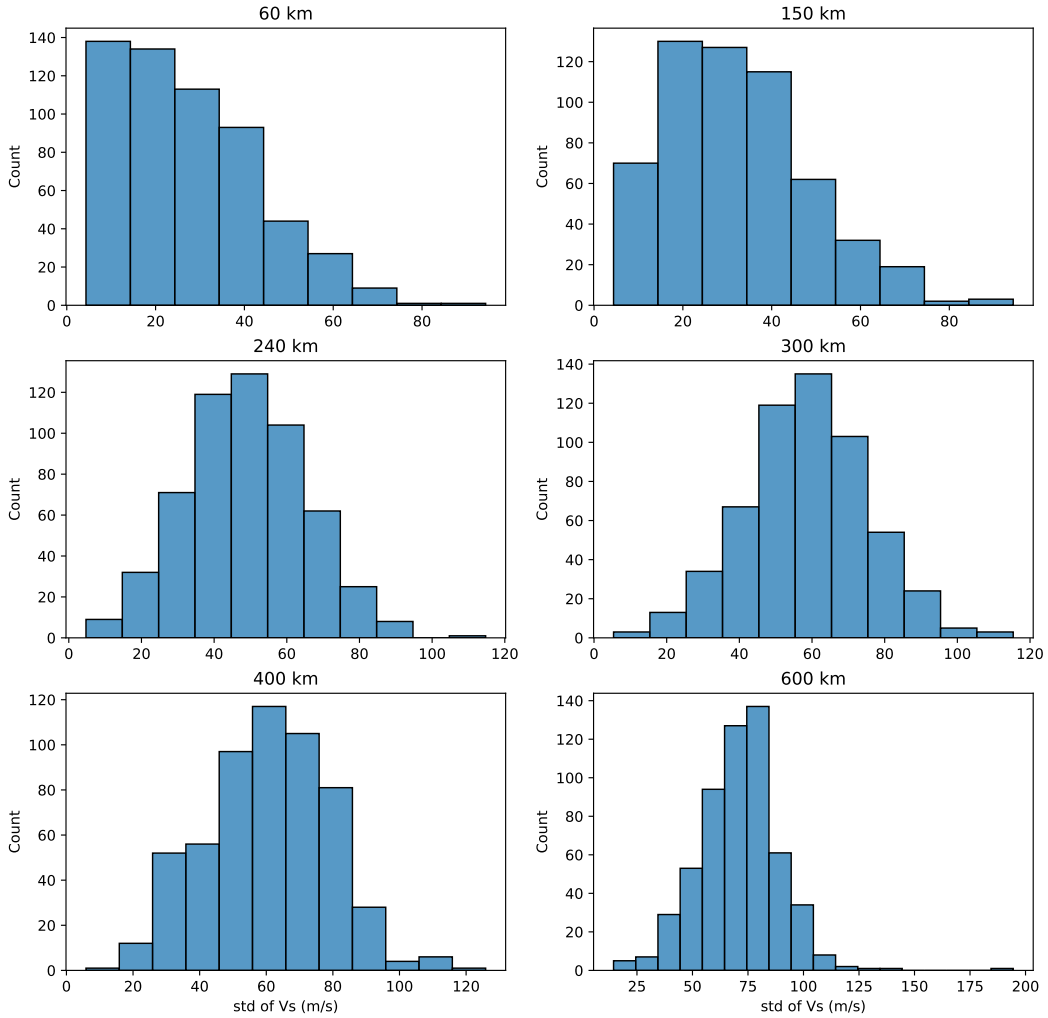

Figure 3.5: The distribution of path-specific V_{SV} standard deviations at different depths. All paths shown in Fig. 3.4 are included to estimate the distribution and the standard deviation for each path is calculated from the ensemble of V_{SV} models sampled in the MCMC step.

matrix cannot be directly estimated from the LSQR method. Alternatively, Trampert and Woodhouse [2003] suggested to calculate the resolution matrix by inverting each column of matrix **G**:

$$\mathbf{R}_j = \mathbf{L}\mathbf{G}_j \tag{3.17}$$

where **L** represents the LSQR operator, $\mathbf{R}_j$ is the j-th column of the resolution matrix. Fig. 3.7 shows one example of reduced χ^2 at depth 150 km as a function of the trace of resolution matrix. The reduced χ^2 decreases as the trace of **R** (which represents the number of indepedent parameters and thus the model complexity) increases. We then performed standard F-tests [Menke, 2018] between the preferred models selected with the L-curve method and determined if the misfit reductions are significant at each depth. In such comparisons, the null hypothesis is that the simpler model and the more complicated model are equivalent at explaining the dataset. The F-test calculates the confidence level at which the null hypothesis can be rejected (the model with more parameters are better). Here we set the confidence level threshold at 85%, and found that the misfit reduction between the isotropic (0Ψ) inversions and $0\Psi + 2\Psi$ inversions are only significant at depth shallower than 300 km, while the reduction between $0\Psi + 2\Psi$ inversions and $0\Psi + 2\Psi$ $+4\Psi$ inversions are not significant except at a depth of 60 km. Details of the F-test analysis can be found in Table 3.2. Considering these results, we believe the presence of the 2Ψ azimuthal anisotropy is required to explain the data in the upper mantle and our study focus on the discussion of the 2Ψ anisotropy in the upper 300 km and we do not discuss the 4Ψ terms.

3.4.3 Isotropic Model

The isotropic part of our azimuthally anisotropic 3-D model is displayed in Fig. 3.8. Because the lowest period surface wave data we measured in this study is 50 s, we do not expect the 3-D model to constrain the crust independently from the mantle, and thus we only present the V_{SV} model starting at 60 km depth. The dichotomy between EANT and WANT dominates the variations in V_{SV} at depths down to 100 km, and the positive anomalies in EANT are

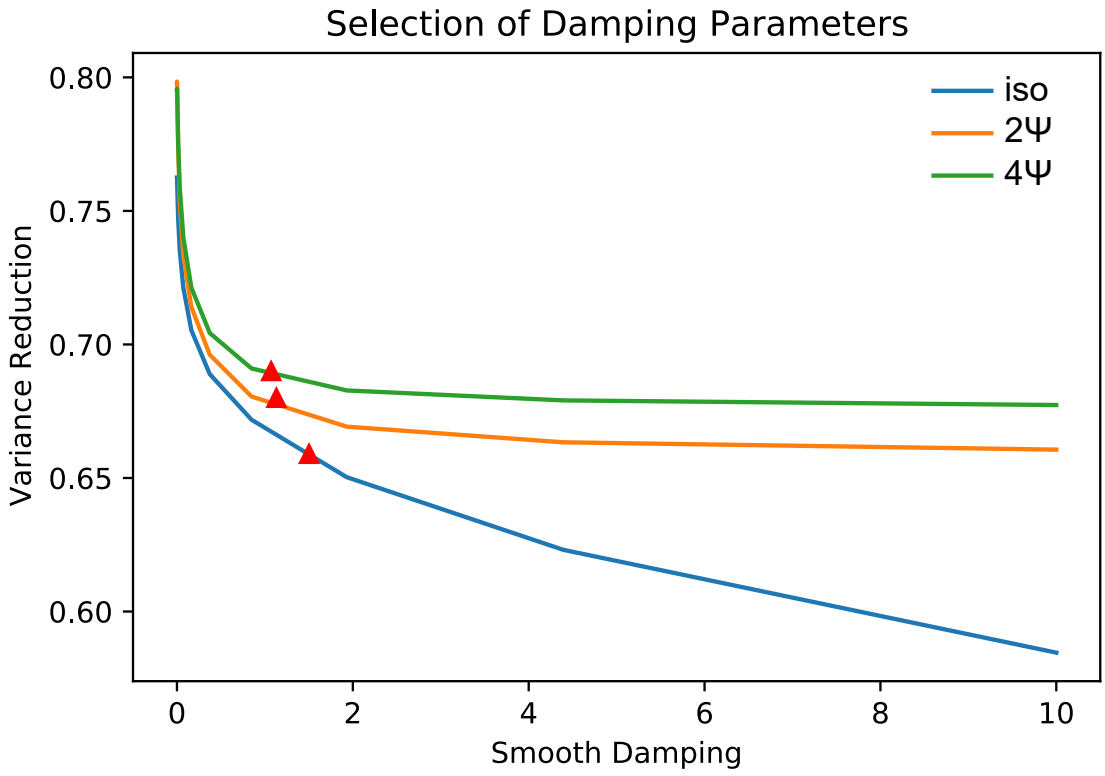

Figure 3.6: An example of damping parameter selection based on the L-curve method. The L-curves illustrate the trade-offs between the variance reduction (y-axis) and the amount of damping added (x-axis). The optimal damping parameters are selected as the elbow points (orange triangles) of the curves. We first searched for the damping parameters of isotropic terms, and then based on the selected damping parameters for isotropic terms, we further searched for the 2Ψ terms, and finally the 4Ψ terms.

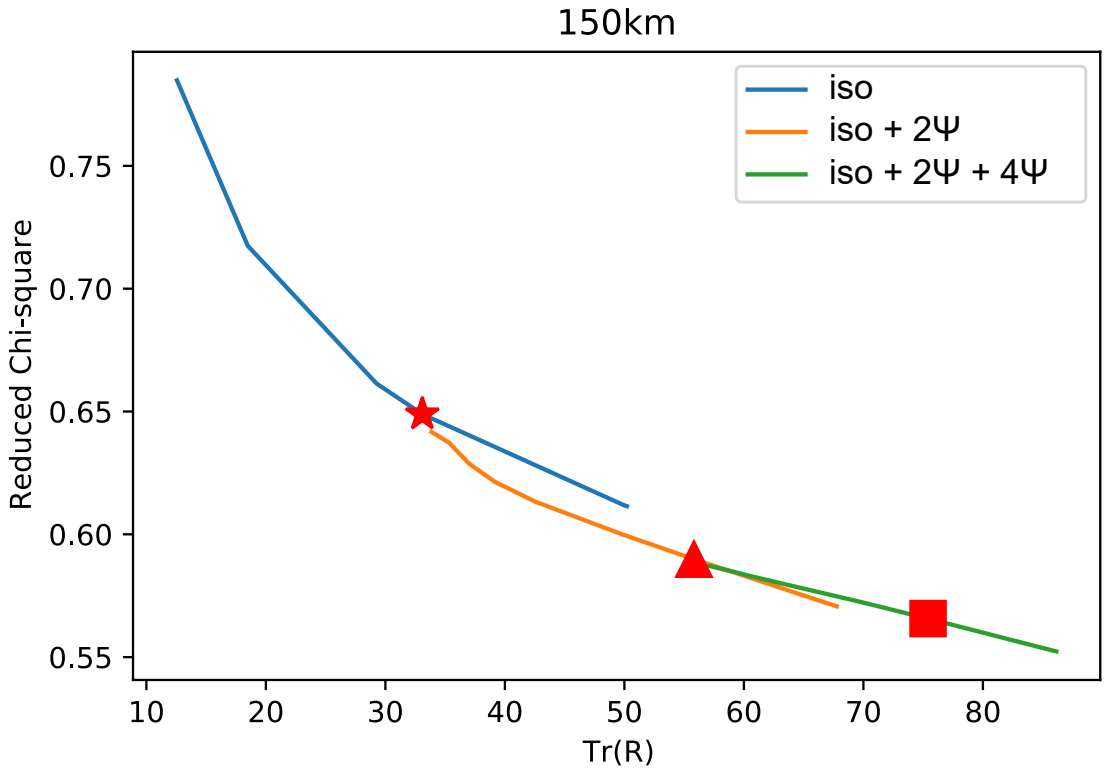

Figure 3.7: An example of reduced χ^2 as a function of the trace of resolution matrix $\mathbf{R}$ for inversions of Vs at depth 150 km. The blue curve is for cases where only the isotropic terms are included in the inversion. Different values of the trace of resolution matrix were obtained by applying different levels of damping. The preferred model selected by the L-curve method is marked as red star. The orange curve represents the inversion with both isotropic and 2Ψ anisotropic terms, and the damping parameters for the isotropic terms were fixed at the preferred values. The green curve is further based on the orange curve, with isotropic, 2Ψ and 4Ψ terms all included in the inversion. The red triangle and red square correspond to the preferred models in the isotropic + 2Ψ and isotropic + 2Ψ + 4Ψ inversions, respectively.

Table 3.2: Significance of 2Ψ and 4Ψ terms at different depths from F-test analysis. A lower probability means that the model with more parameters has significantly lower misfits compared to the model with fewer parameters, and thus those extra parameters are needed to explain the data.

Depth	$\mathbf{P}(0\Psi + 2\Psi == 0\Psi)$	$\mathbf{P}(0\Psi + 2\Psi + 4\Psi == 0\Psi + 2\Psi)$
60 km	0.23%	6.62%
150 km	4.40%	37.50%
200 km	2.98%	35.41%
250 km	12.56%	39.50%
350 km	15.19%	30.09%
450 km	19.67%	44.74%
600 km	34.21%	25.54%

visible down to 200 km depth, which indicate the distinct seismic patterns underneath the cratonic EANT and the extensional WARS. The largest amplitude anomalies range from +7% relative to PREM model underneath EANT, to about -5% below WANT. Such strong anomalies start to diminish below 200 km. Around the mantle transition zone, velocity anomalies are generally within +/- 2%.

As is shown in Fig. 3.5, the uncertainties in the path-specific measurements increases with depth, but the amplitudes of the velocity anomalies decrease with depth. For example, the mean uncertainty at 600 km is ∼75 m/s (∼1.3%). Thus most of the V_{SV} variations shown at 600 km, which are below 2%, are likely not constrained by the data. We therefore refrain from interpreting the anomalies in the transition zone in our models due to the limited resolution at these depths. On the contrary, depths shallower than 300 km have stronger variations and smaller uncertainties, and patterns shown at these depths can be interpreted with more confidence.

Vertical slices of three transects are shown in Fig. 3.9. Overall, the fast V_S anomalies

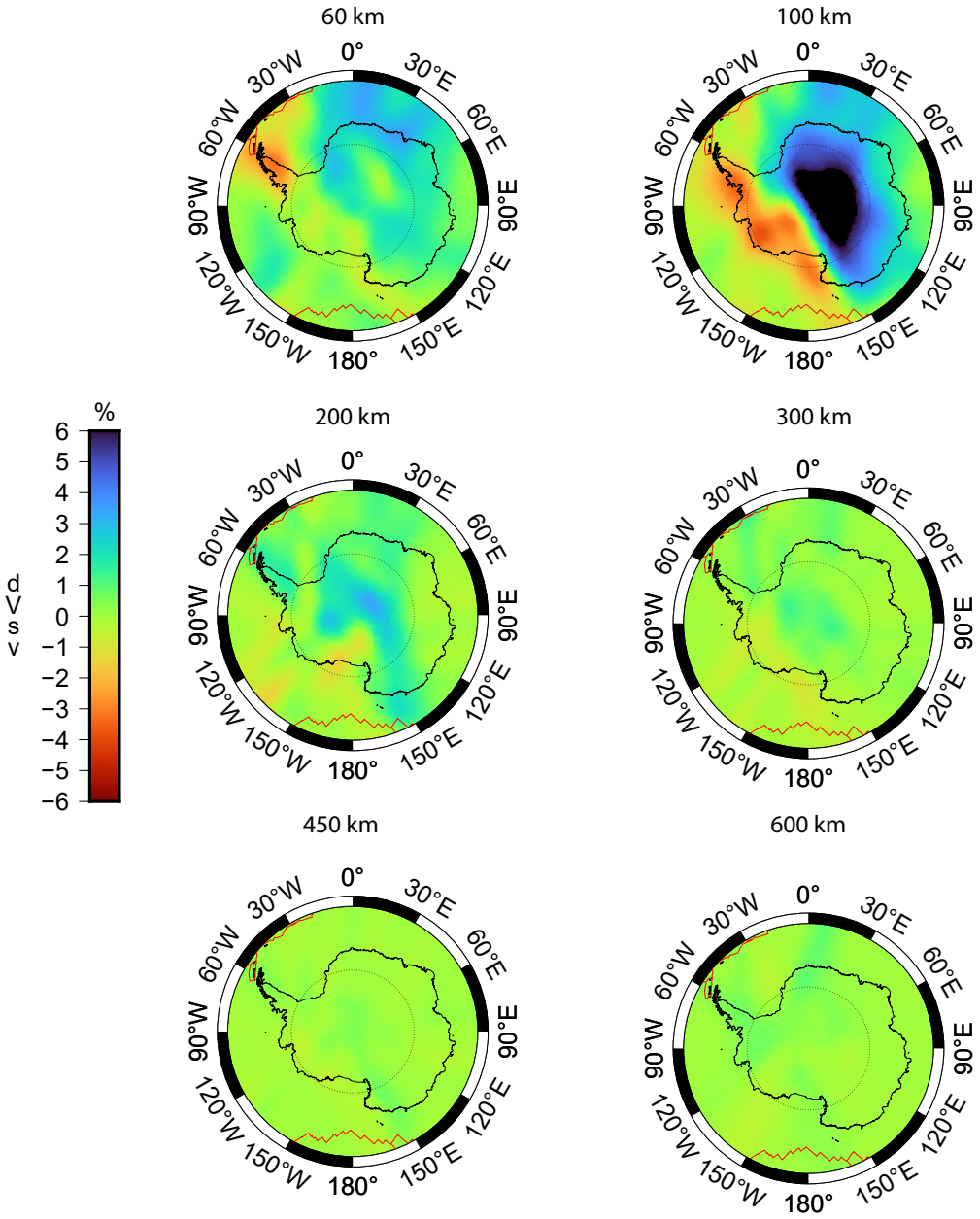

Figure 3.8: Isotropic part of our 3-D V_{SV} model at different depths. Velocity perturbations are calculated relative to PREM.

underneath EANT is consistent with observations from Lebedev et al. [2009], who found a global average of 5 - 6% positive V_S anomalies at 100 - 150 km depth in cratonic lithospheres. Similar to Lloyd et al. [2020], we also observe a varying depth extent of the fast velocity anomalies underneath the interior of EANT (Figs. 3.8 and 3.9): central EANT is underlain by thicker fast anomalies compared to the EANT coastal region. However, the depth range of fast anomalies in our model is roughly 200 - 300 km, which is shallower than the 250 - 350 km estimated by Lloyd et al. [2020]. Heeszel et al. [2013] observed a peak positive V_S anomaly of $\sim$ 7 % beneath GSM at 150 km depth with Rayleigh wave tomography, which is consistent with our results. Comparing to other Archean cratons, the peak V_S anomalies under GSM are similar to the tomography results for the Archean Kaapvaal craton, the V_S anomalies of which are reported to be $\sim$6 % larger than PREM at 150 km [e.g. Ritsema and van Heijst, 2000a; Chevrot and Zhao, 2007]. Tomography results for North American craton also show positive V_S anomalies at similar amplitudes ($\sim$ 6 %) [e.g. Yuan et al., 2014]. The amplitudes of positive anomalies beneath GSM in our model are weaker compared to another Archean craton, the Yilgarn craton (west Australia), as the surface wave tomography results for Australia show positive anomalies $>$ 8 % compared to PREM between 100 - 150 km [e.g. Yoshizawa, 2014]. The coastal area of EANT has a relatively thinner fast seismic lid extending down to 100 - 150 km (Figs. 3.8 and 3.9). From Fig. 3.9, we observe both the thickest craton and fastest velocity under the GSM, which is consistent with results from Heeszel et al. [2013] and Lloyd et al. [2020].

WANT features negative anomalies down to 200 km depth, beneath MBL and along the Amundsen Sea coast to the AP (Antarctica Peninsula). In Lloyd et al. [2020], a negative anomaly extending into the transition zone is identified in that area and is associated with a potential mantle plume. While we also observe negative velocity anomalies underneath the MBL between 300 - 400 km depth (Fig. 3.9 (a) and (c)), these anomalies extend over a wide area, larger than expected for a plume, making it difficult to determine whether this is related to a plume. We note, however, that the long wavelength of higher mode surface

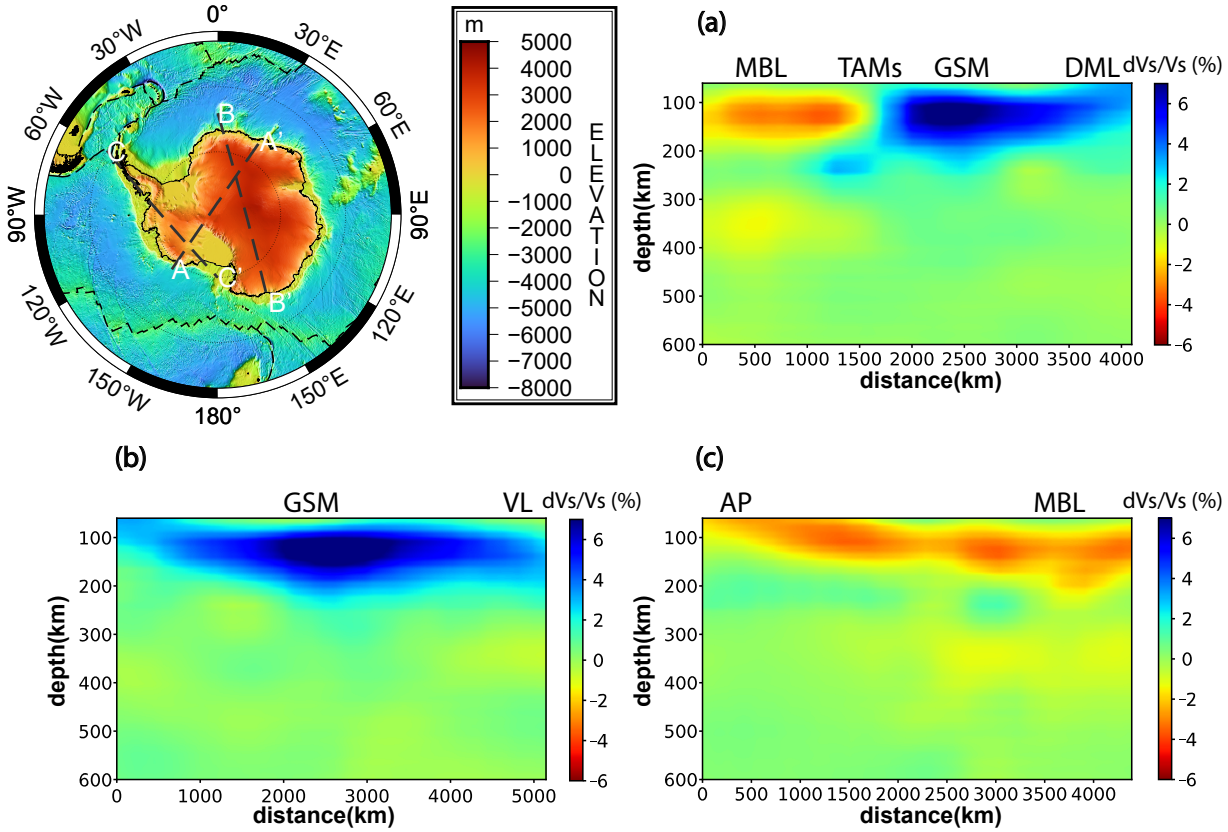

Figure 3.9: Vertical slices of the 3-D model. V_{SV} structure along transects A-A'(a), B-B'(b) and C-C'(c). Profile locations are marked in the upper-left map. Abbreviations: AP = Antarctica Peninsula; DML = Dronning Maud Land; GSM = Gamburtsev Subglacial Mountains; MBL = Marie Byrd Land; TAMs = Transantarctic Mountains; VL = Victoria Land.

waves ($\sim$ 500 km) limits the horizontal resolution of the 3-D model at such depths, and our synthetic isotropic tests (see below) also show that the model resolution is barely sufficient to constrain a 1000 km wide negative anomaly. Our model is thus unlikely to be able to constrain a thin mantle plume.

3.4.4 Azimuthal Anisotropy

Fig. 3.10 displays the horizontal distributions of the 2Ψ terms at depths ranging from 75 km to 285 km. Stronger azimuthal anisotropy can be observed in the interior of Antarctica as well as in WL at depths between 100 km and 200 km. The amplitudes of anisotropy start to decrease below 225 km and the anisotropy becomes weak at multiple locations in and around Antarctica starting at 285 km. This is consistent with our F-test results showing that the 2Ψ terms are not significant below 300 km. In oceanic areas, fast directions are roughly parallel to the extension direction of the Pacific-Antarctic Ridge at 75km, which agrees with the phase velocity maps of Roult et al. [1994] and is consistent with alignment of olivine in active mantle flow. However, due to the limited azimuthal coverage of the surrounding oceanic areas, we focus on the interpretation of the azimuthal anisotropy on the Antarctic continent. Abrupt changes in fast directions can be observed in all 4 depth slices between EANT and WANT. For EANT, the fast directions of anisotropy at 75 km show a bi-modal distribution, with the top half dominated by SW-NE and the bottom half by SE-NW. At deeper depths, SE-NW becomes the dominant fast direction, especially in the interior of EANT. Coastal areas tend to present different fast directions compared to the interior. The weak amplitudes of azimuthal anisotropy in Enderby-Kemp Land (EKL) and Lambert Graben (LG) are likely to caused by poorer ray-path coverage in these regions (Fig. 3.4. For WANT, we see that the fast direction near the Amundsen Sea changes from NE - SW to NW - SE from 75 km to 150 km, and then changes back to NE - SW below 200 km. Such changes are likely to associate with the lithosphere-asthenosphere boundary, as we explain in the Discussion section. We also point out that the edges of EANT, especially

the NE corner, do not have good azimuthal ray-path coverage due to the lack of stations. So the azimuthal anisotropy results for these areas are likely less reliable compared to the majority of WANT and the center of EANT.

3.4.5 Synthetic Tests

We implemented synthetic tests in order to evaluate the quality of the data coverage and the trade-offs between isotropic and anisotropic model parameters. Fig 3.11 shows example tests at 150 km depth for an isotropic checkerboard test, a test for an anisotropic inversion with an isotropic true model, and an anisotropic inversion with anisotropic true model. The true model of the isotropic checkerboard test has a strong positive anomaly at the South Pole with a radius of 10° (∼1000 km). In other areas, the checkerboard anomalies correspond to 8° (latitude) by 36° (longitude) cells. The cell size varies with latitude and the size of the negative anomaly at MBL is about 900 km × 1000 km. In the isotropic checkerboard test, the positive and negative anomalies south of -70 degrees can be resolved, though some smoothing effects are visible toward the east. The resolution in the surrounding oceans is not as good as on the continent because of the reduced ray path coverage. The anisotropic inversion of an isotropic model shows that the isotropic input model is well recovered and that a very small ($< 0.2\%$) amount of anisotropy is found in the output model over more than 75% of the study region, meaning that most of the anisotropic signal found at that depth is constrained by the data. Some moderate artifacts are observed at the transition between the positive anomalies in the East and the negative anomalies in the West, with the anisotropy amplitude as much as 0.6%, but it is still very small compared to the anisotropy amplitudes found in the 3-D models resulting from the real data inversions. The recovered amplitude and fast directions are consistent with the input model in most of the Antarctica continent. Inconsistencies can, however, be found in some areas of the surrounding oceans where the azimuthal coverage is not ideal. We also note that the isotropic terms in the second and third tests are recovered well compared to the true models, and the amplitudes

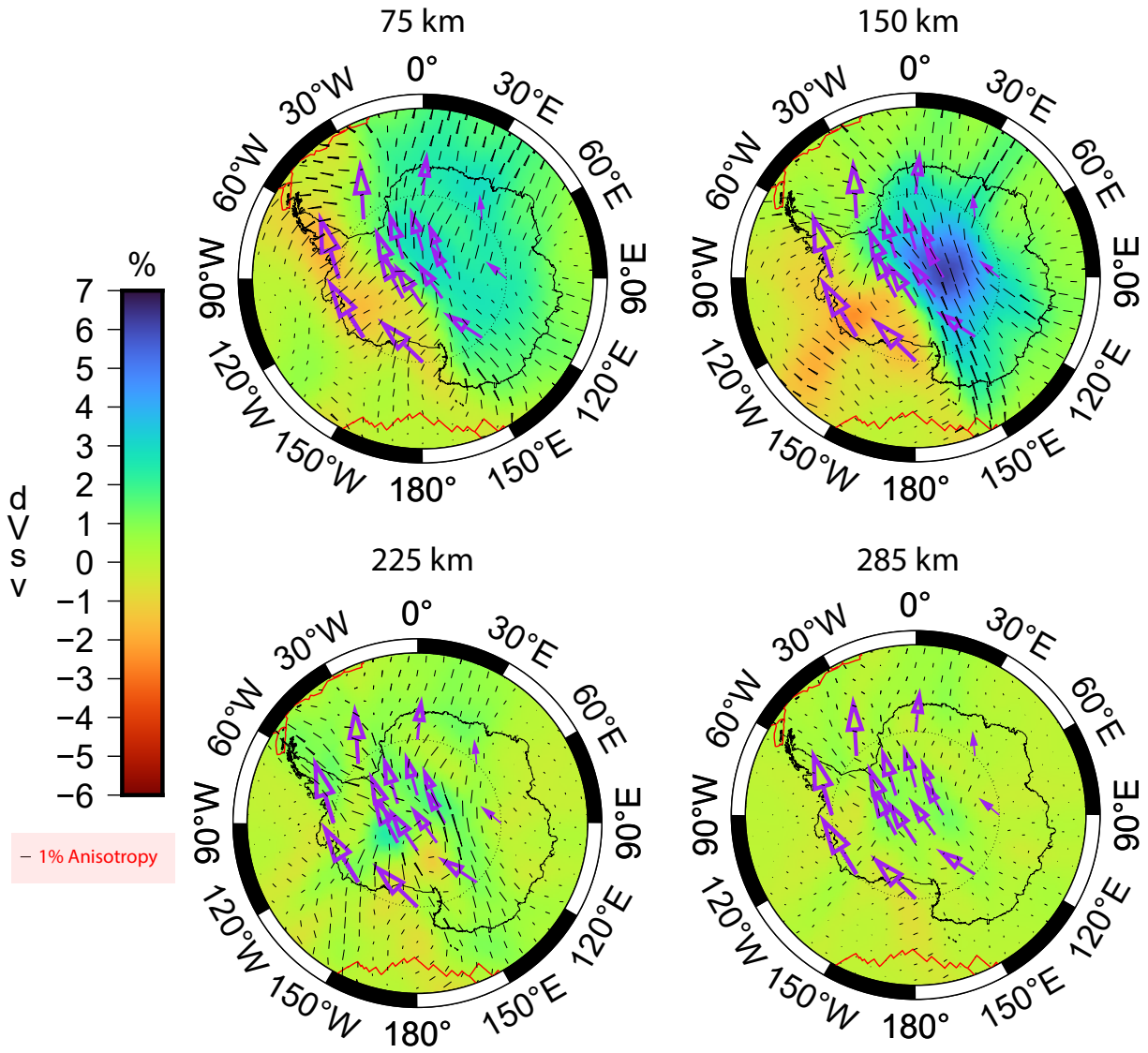

Figure 3.10: 2Ψ anisotropy at different depths (black bars). The background color represents the isotropic part of the model. Directions of black bars represent the fast directions and the length of black bars are proportional to the amplitude of the anisotropy.The purple arrows represent the APMs based on NUVEL-1A with no-net rotation reference frames [Gripp and Gordon, 2002]. The red line at bottom represents the Pacific-Antarctic Ridge.

of the isotropic terms are barely affected by the introduction of the azimuthal anisotropy.

3.4.6 Phase Velocity Maps

In this section, we briefly show the resulting 2-D phase velocity maps obtained. Future work may leverage these phase velocity results by combining them with higher frequency surface wave measurements from ambient noise method or inter-station measurement method, in order to have good constraints for the upper 50 km structure. It is also possible to jointly invert these phase velocity maps with other types of seismic data, such as body waves or receiver functions, to resolve the ambiguities from separate inversions and obtain a more complete picture of Antarctica.

We considered a number of periods for each surface wave mode and the results for each mode and period are filtered using the reliability analysis described in Chapter 2. Only modes and periods with sufficient ray-path coverage were considered for 2-D phase velocity map inversion. The F-test results using a confidence level of 85 % to determine the significance of additional 2Ψ terms are shown in Table.3.3.

Fig. 3.12 displays examples of the azimuthally anisotropic phase velocity maps for fundamental and higher modes. The dichotomy pattern between WANT and EANT shown in the V_{SV} model is also present in the phase velocity maps, especially for fundamental modes and the second overtone at a period of 100s, which are sensitive to the upper 200 km. EANT is associated with fast anomalies while WANT has consistent slow anomalies around MBL, which may indicate a deep source of thermal anomalies around that area. Amplitudes of anisotropy are stronger for fundamental modes than for higher modes. Since fundamental modes are sensitive to shallower structure, this indicates weaker anisotropy at greater depths. This is consistent with our 3-D V_S results and with Sieminski et al. [2003] who determined azimuthal anisotropy to be significant in the upper 200 - 250 km. In addition, fundamental modes show stronger anisotropy in the surrounding oceanic areas, agreeing with the results of Roult et al. [1994]. Fast directions are orthogonal to the Pacific-Antarctica Ridge for

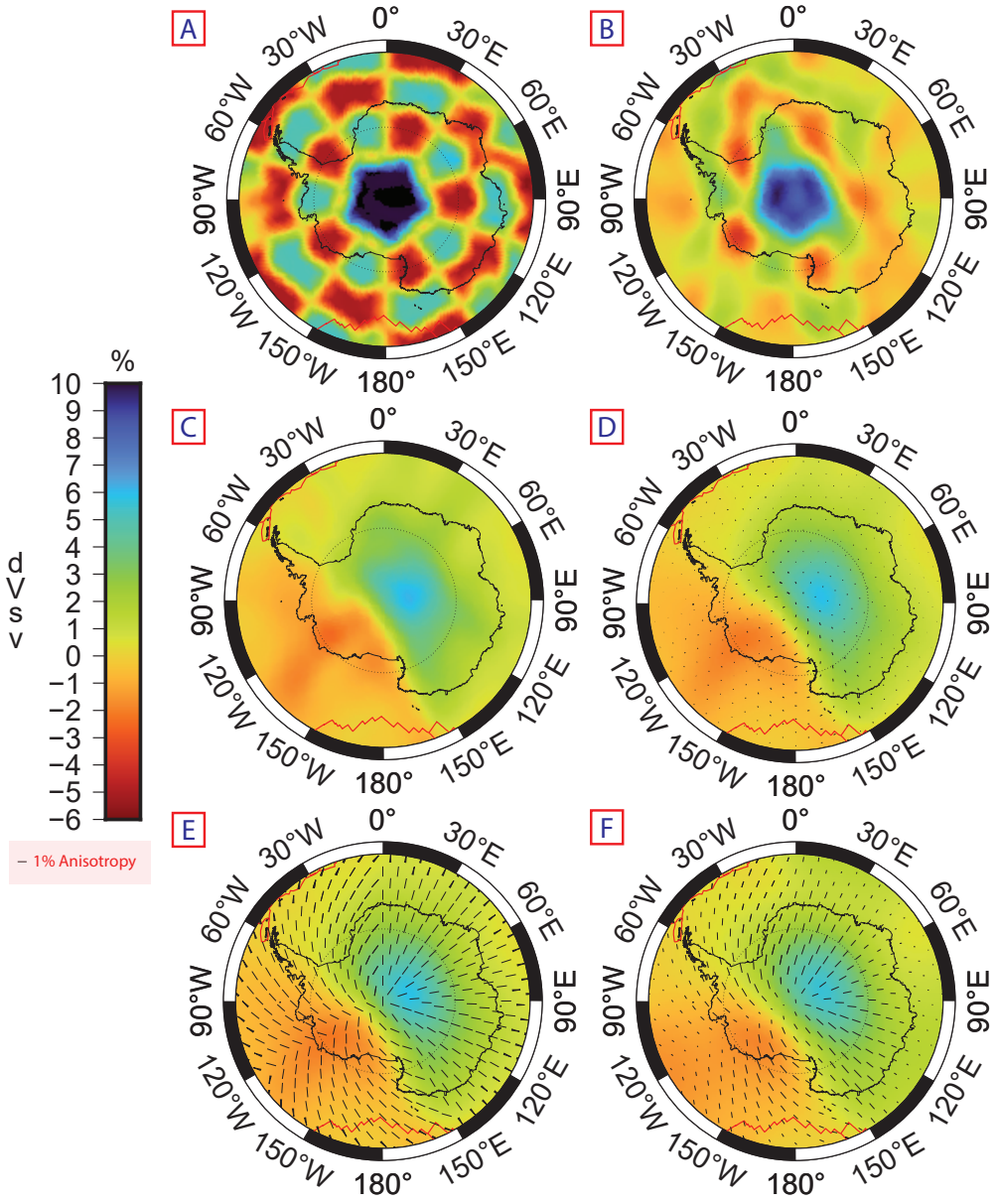

Figure 3.11: Synthetic tests at 150 km depth. Isotropic checkerboard test (top): (A) is the input V_{SV} model and (B) is the recovered isotropic model. The middle panels are for an anisotropic inversion with an isotropic input model (C). The recovered output model with 2Ψ terms included in the inversion is shown in (D). The bottom panels are for an anisotropic resolution test. (E) is the input model and (F) is the recovered model. The length of black bars represents the amplitudes of the anisotropy.

Table 3.3: Significance of 2Ψ terms in the phase velocity map modeling for different modes and periods using a F-test analysis. A lower probability means that the model with more parameters has significantly lower misfits compared to the model with fewer parameters, and thus those extra parameters, i.e. anisotropy, are needed to explain the data.

n	**Period (s)**	**P(iso + 2Ψ == iso)**	**P(iso + 2Ψ + 4Ψ == iso + 2Ψ)**
0	51	0.00%	0.00%
0	62	0.00%	0.00%
0	89	0.00%	0.00%
0	115	0.00%	0.00%
0	151	0.04%	0.00%
0	176	0.61%	0.00%
1	173	10.65%	0.52%
2	99	0.62%	1.90%
2	150	0.04%	0.00%
3	69	1.81%	0.00%
3	88	5.16%	0.06%
4	51	6.42%	0.46%
4	62	0.51%	0.00%

fundamental mode. Within the Antarctic continent, the overall fast directions of azimuthal anisotropy are generally consistent with the anisotropic results for our 3-D model, including the dominant NE-SW fast directions in WANT and a sudden change of fast directions from WANT to EANT.

While phase velocity maps are useful, because surface wave phase velocities are sensitive to overlapping depth ranges, interpreting the fast directions directly from those maps is not straightforward. We thus focus the interpretation on the 3-D model instead.

3.5 Discussion

Following Bartzsch et al. [2011], we approximated the LAB depth as the middle of the interval over which V_{SV} decreases in our isotropic model. Fig. 3.13 shows our calculated LAB depth for the Antarctic plate. We see that the WANT and EANT have very different LAB depths with ∼80 km for WANT and ∼180 km for EANT, consistent with the different tectonic natures of the two regions. The estimated WANT LAB depth is in agreement with the 70 - 100 km range obtained by Heeszel et al. [2016]. Comparing our results to An et al. [2015a] who defined the LAB as the shallowest position with a temperature crossing the 1330° adiabat, we find that the LAB depth for the center of EANT is lower in our results (∼190 km compared to ∼225 km in theirs). The difference is likely to be caused by the different definitions of the LAB as well as the difference in surface wave measurement techniques.

In general, global-scale surface wave azimuthal anisotropy models show a good correlation between the fast seismic direction and APM models at depths associated with the asthenosphere in regions with a simple tectonic history such as oceanic plates. However, for regions with a complicated tectonic history, the correlation is quite low [Debayle and Ricard, 2013]. Accardo et al. [2014] summarized a number of SKS splitting measurement work for Antarctica and pointed out that both hotspot (HS) and no-net rotation (NNR)

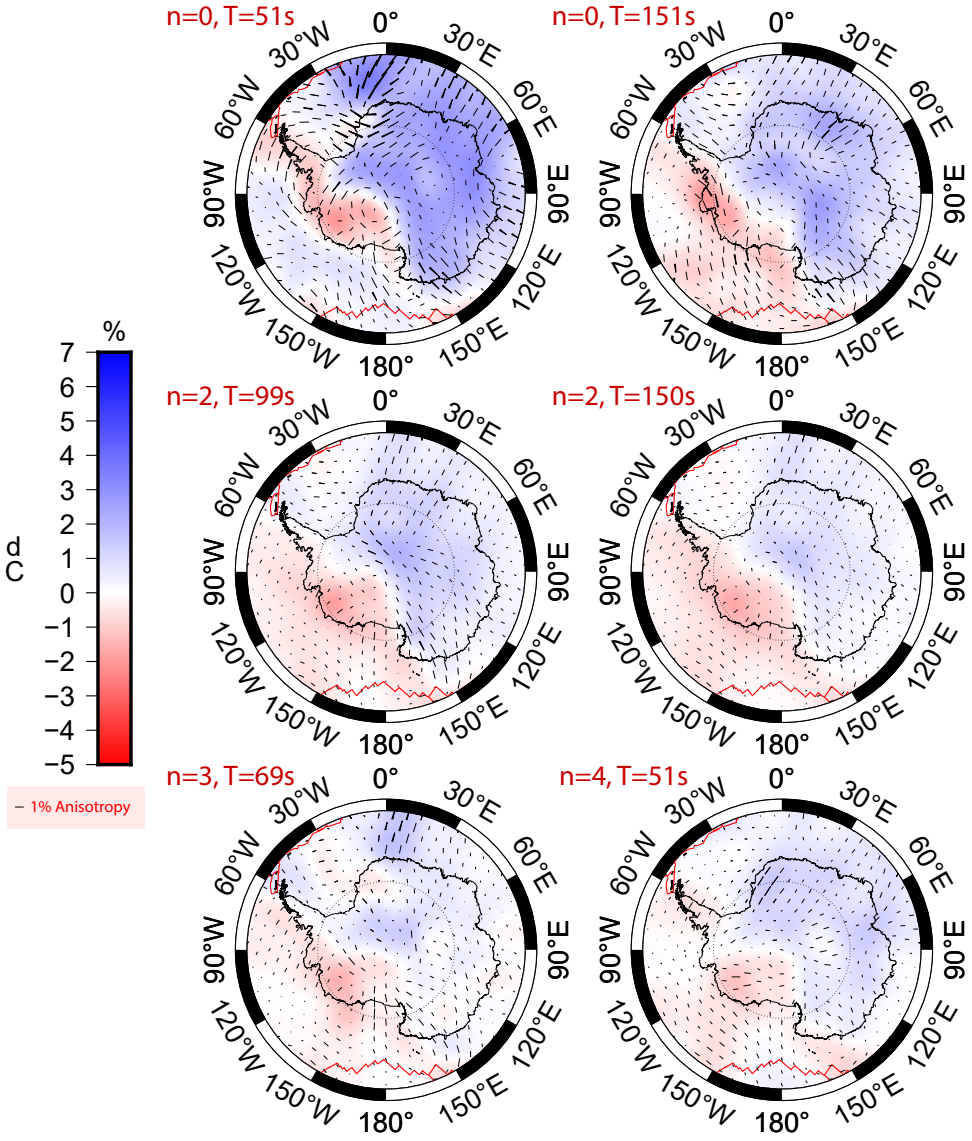

Figure 3.12: Horizontal cross sections of the 2Ψ anisotropic terms (black bars) for phase velocities at selected modes and periods.. Directions of black bars represent the fast directions and the length of black bars are proportional to the anisotropic strengths.

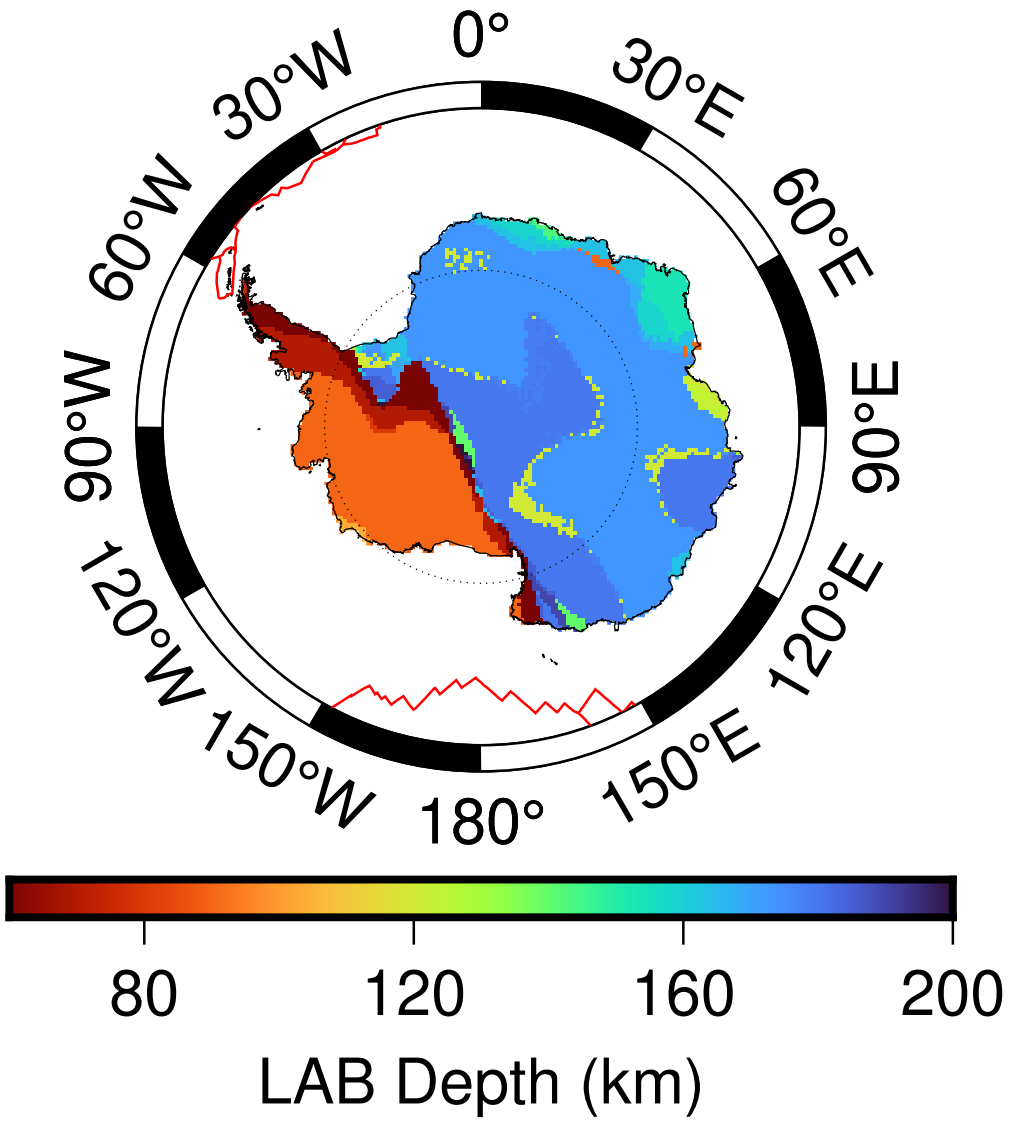

Figure 3.13: Topographic map of the Antarctic plate LAB depth calculated using the middle point of the interval over which V_S decreases in the isotropic model.

absolute reference frames are highly inconsistent with most of the observed splitting results in Antarctica. They concluded that anisotropic fabric does not broadly result from shear associated with the motion of the Antarctic lithosphere over the mantle, due to the relatively slow motion speed of the Antarctica plate. In Fig. 3.10, we plotted the APMs based on NUVEL-1A with the no-net rotation (NNR) reference frame in addition to the fast directions of azimuthal anisotropy. The NUVEL-1A with hotspot (HS) reference frame has a pattern similar to that of the NNR model, so here we focus on the comparison with the NNR APMs only.

Fast directions of azimuthal anisotropy vary with depth below WANT. At regions around MBL and EWM, the fast directions are dominantly SW - NE at depths shallower than 100 km, which is nearly perpendicular to the APM. At 150 km, which corresponds to the asthenosphere based on our estimated LAB depth (Fig. 3.13), we observe fast directions which are almost perpendicular to those at 75 km depth and tend to align with the APMs. This indicates that the fast direction between 100 - 150 km may correspond to present-day mantle flow within the asthenosphere, whereas the azimuthal anisotropy at shallower depth mainly reflects extensive Cenozoic extension including the final pulse of western WARS rifting in the Miocene [Accardo et al., 2014].

For EANT, the fast directions start to align well with the APMs from 100 km down to at least 225 km. This depth range appears to be shallow compared to the estimated LAB depth of the EANT Craton (160 - 190 km from Fig. 3.13) and therefore this alignment is unlikely related to present-day mantle flow as one might be tempted to infer. Shen et al. [2018] detected a robust negative V_S anomaly from $\sim$50 to $\sim$110 km beneath GSM, which they interpreted as compositional variability related to past orogenic processes. Heeszel et al. [2013] also reported lower phase velocities at periods < 50 s beneath GSM compared to other regions of Archean and Proterozoic ages. Similar relatively slow anomalies beneath EANT can also be observed from our isotropic model. By analyzing the fast directions of azimuthal anisotropy with depth, Yuan and Romanowicz [2010] found a second layer on top

of the thermal layer in the lithosphere of North American craton, which they also related to compositional origins. The change of fast directions we found at depths much shallower than the LAB could be an indicator of a second layer in EANT craton. According to both the isotropic and anisotropic terms of our model, the interior of EANT shows contrasting patterns above and below $\sim$ 100 km. While the anisotropy in the upper 100 km likely reflects the signature of past deformation into the continental lithosphere, the change of fast direction at 100 km may indicate the existence of a second layer within the thick cratonic lithosphere, possibly of compositional origin similarly to what has been observed for the North American craton [e.g. Yuan and Romanowicz, 2010; Abt et al., 2010].

In an attempt to compare our results with shear-wave splitting studies, we followed Montagner et al. [2000] and used our 3-D azimuthally anisotropic model to predict the SKS delay times δt and fast directions Ψ under the assumption of weak anisotropy with a horizontal axis of symmetry:

$$\delta t = \sqrt{(\int_0^R \frac{G_s}{V_s L} dr)^2 + (\int_0^R \frac{G_c}{V_s L} dr)^2} \tag{3.18}$$

and

$$\tan 2\Psi = \frac{\int_0^R \frac{G_s}{V_s L} dr}{\int_0^R \frac{G_c}{V_s L} dr} \tag{3.19}$$

where V_S and L are the shear-wave velocity and Love parameter from the isotropic model, respectively, and G_c and G_s are the 2Ψ anisotropic parameters that determine shear-wave anisotropy. L, G_c and G_s can be expressed by the elastic tensor C_{ij}:

$$L = \frac{1}{2}(C_{44} + C55), \tag{3.20}$$

$$G_c = \frac{1}{2}(C_{55} - C_{44}), \tag{3.21}$$

$$G_s = -C_{45}. \tag{3.22}$$

and these anisotropic parameters can be linked to shear-wave velocity and its azimuthal

variation according to Montagner et al. [2000]:

$$\rho V_{S_I}^2 = L + G_c \cos 2\Psi + G_s \sin 2\Psi, \tag{3.23}$$

$$\rho V_{S_{II}}^2 = L - G_c \cos 2\Psi - G_s \sin 2\Psi. \tag{3.24}$$

Our predictions are compared to previous SKS splitting measurements in Antarctica [Müller, 2001; Bayer et al., 2007; Reading and Heintz, 2008; Barklage et al., 2009; Hernandez et al., 2009; Accardo et al., 2014]. We only plotted available SKS measurements with good quality from previous work in Fig. 3.14. It is worth noting the SKS measurement results at a couple of locations differ among different studies and that large variations are sometimes found within the same study [e.g. Müller, 2001; Reading and Heintz, 2008], which indicates quite large uncertainties in both SKS delay times and fast directions.

Overall, our predicted splitting time amplitudes roughly agree with observations. For WANT, including EWM, WARS and MBL, the dominant fast direction is SW - NE, for both predictions and SKS measurements, which may indicate strong and uniform anisotropy within the upper mantle in these areas. However, the fast directions at about 150 km in our results tend to align with the APM and disagree with this dominant fast direction, which should relate to the effects of plate motion on the top of asthenosphere. At AP, the predicted fast directions are sub-parallel to the observed fast directions. The two stations located at DML also show good agreement with our predictions. The red circle and red bar located in GSM represent the overall splitting directions and study area from Hernandez et al. [2009]. Since the observations are perpendicular to our predictions, we argue that the difference might result from the lack of resolution of the shallower structure in our 3-D model. From the 3-D anisotropic model (Fig. 3.10), the fast directions in GSM are rotating anti-clockwise, from SSW - NNE to SSE - NNW from 75 km to 150 km. The fast directions at depths between 60 km and 100 km in our model match the SKS observations in GSM much better than the integrated results, which implies that the splitting results better reflect the anisotropy existing at depths shallower than 100 km. The SSE - NNW fast direction below

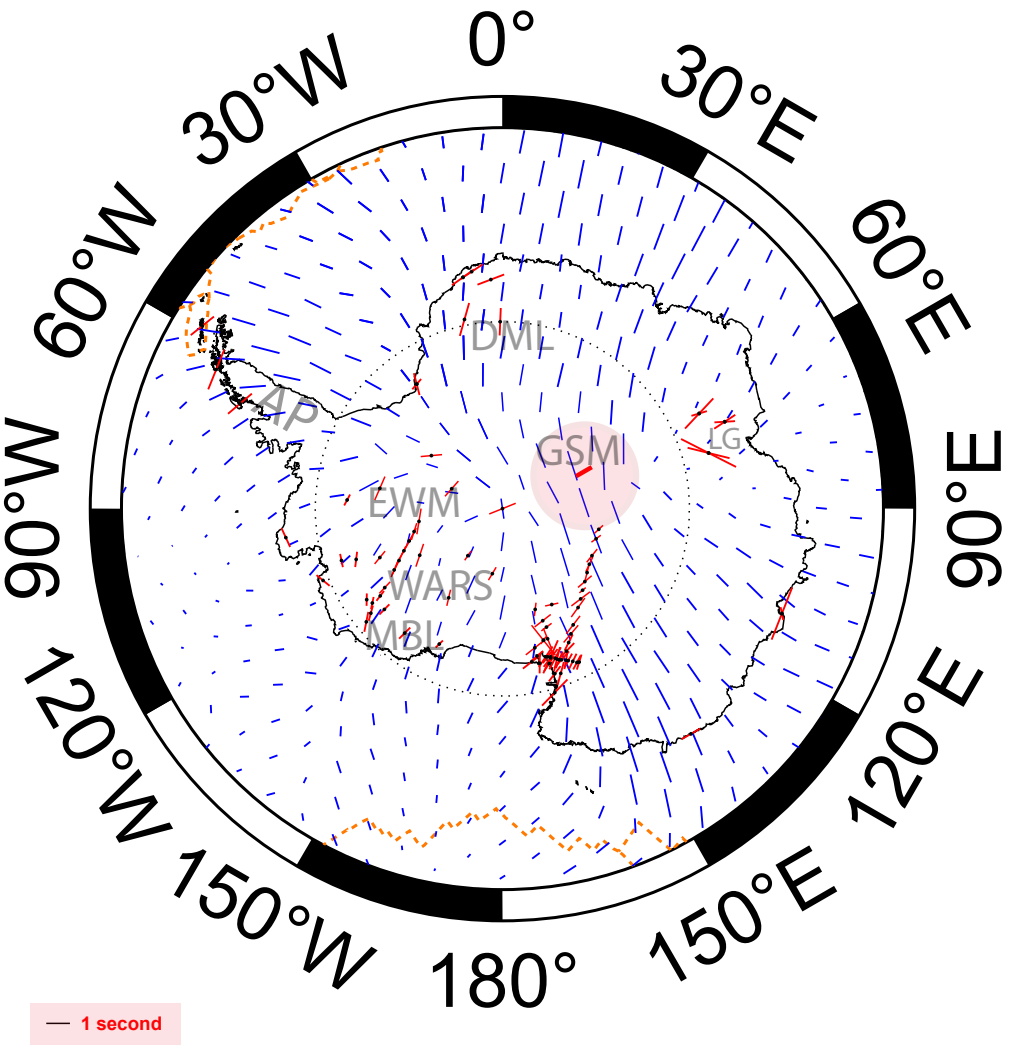

Figure 3.14: Comparison of observed (red) and predicted (blue) SKS splitting measurements for Antarctica. The red bar and red circle in EANT roughly describe the SKS measurements and seismic station distribution of AGAP network [Hernandez et al., 2009]. Lengths of the bars are proportional to the SKS splitting delayed time while the directions represent fast directions. Abbreviations: AP = Antarctica Peninsula; DML = Dronning Maud Land; EMW = Ellsworth Whitmore Mountains; GSM = Gamburtsev Subglacial Mountains; LG = Lambert Graben; MBL = Marie Byrd Land; WARS = West Antarctic rift system.

150 km actually corresponds to the APM directions of EANT (Fig. 3.10). At TAMs, the observed fast directions are mainly perpendicular to the trend of TAMs, but our predictions show fast directions changing from SW - NE in WANT to SSE - NNW in EANT, which could be explained by the smoothing damping effects we added in the second step inversion.

The observed fast directions are parallel to the plate margins at multiple locations, whereas our predictions are generally normal to the edges. According to Accardo et al. [2014], there is a mix of normal and parallel results on EANT margins, which may indicate the complexity of asthenospheric flow around the craton. Also, due to the limited horizontal resolution of surface wave tomography, our results are unlikely to capture such sharp changes in fast directions.

In summary, our SKS splitting predictions based on the 3-D anisotropic model show good agreement with station-wise observations. Differences in fast directions are likely owing to the lack of shallow sources of anisotropy, such as the ice and crustal layers beneath a given station.

3.6 Conclusion

In this chapter, we applied the transdimensional inversion method we proposed in Chapter 2 for multi-mode surface waves to the Antarctica Continent, and presented a new 3-D azimuthally anisotropic shear-wave velocity model for Antarctica. We additionally obtained a new set of phase velocity maps for fundamental mode and higher modes up to $n = 4$, which could be inverted in future work together with other types of seismic observations, including body waves, receiver functions, group velocity dispersions, and phase velocity dispersions from ambient noise method. 1-D path-averaged V_S profiles were first estimated from the waveforms of both fundamental and higher-mode surface waves in the period range 50 - 200 s. Those 1-D path-averaged results were then inverted to get a 3-D V_S model with both isotropic and anisotropic terms. By taking advantage of the recently deployed seismic

arrays, we were able to obtain better ray-path coverage compared to earlier higher-mode studies of Antarctica. In this model, the isotropic terms are constrained between 60 km and 600 km, whereas the 2Ψ anisotropic terms are only significant above 300 km according to our F-tests. It provides valuable information to constrain the distinct WANT and EANT. Major observations in this work include the following:

1. EANT and WANT have distinct V_S anomalies in the upper mantle: the cratonic EANT has strong positive V_S anomalies down to 150 - 250 km, with the fast layer thinner in the coastal regions than in the interior of EANT. In contrast, WANT features negative anomalies down to about 200 km.

2. Based on the isotropic 3-D V_S, we estimated the LAB depth to be $\sim$190 km for EANT, and $\sim$80 km for WANT.

3. In WARS, the fast axes of azimuthal anisotropy change from perpendicular to the APM to parallel to the APM from 75 km to 150 km, which indicates the influence of plate motion on structure near LAB depth. Other regions in WANT, including EWM and AP, start to show good alignment with the APM at much greater depths (225 km). This reflects either a poor azimuthal resolution in those regions, or the fast axes are dominated by other secondary mantle flows rather than the plate motion, as the amplitudes of plate motion in Antarctica are relatively weak. The integrated azimuthal anisotropy distribution also agrees well with SKS-splitting results at most stations across WANT.

4. In EANT, the fast axes start to align well with APM at about 100 km, which is quite shallow compared to the deep LAB depth of the craton. So the change of fast axes takes place in the lithosphere rather than around the LAB, which may indicate the existence of a second layer within the lithosphere of the EANT craton.

   The current results also have the following limitations which might be resolved by future work:

(a) The current model does not resolve the upper 60 km due to the relatively large periods of the seismic observations used in the inversion. By including higher-frequency surface wave measurements from ambient noise methods or inter-station methods, we could better resolve the shallower structure, and thus obtain a more complete picture of structure under Antarctica.

(b) The current method is based on single-station measurements, and most paths used in this study cover both the Antarctica continent as well as the surrounding oceans. The model doesn't have good resolution in oceanic areas due to limited raypath coverage, and this may affect the resolution of the continent as well due to smearing of the model. Our current solution is to add a modest amount of norm damping in the inversion so that oceanic areas with low path coverage remain close to the reference model. A more sophisticated method would be needed to better separate the anomalies from the oceans and the Antarctica continent, e.g. by fixing the model grids in oceans according to other published 3-D regional V_S models.

CHAPTER 4

Mars (InSight)

4.1 Introduction

One of the objectives of the InSight mission is to constrain Mars interior structure. Previous missions to Mars have focused on the surface characteristics of the planet by examining features like canyons, volcanoes, and rocks. However, to better understand the early formation and evolution of Mars, we need to obtain constraints on its internal structure. Several Mars seismological models have been proposed over the years based on the estimated bulk density and moment of inertia of Mars, as well as geochemical and equation of state data (e.g. Sohl and Spohn [1997], Gudkova and Zharkov [2004], Nimmo and Faul [2013]). There are, unfortunately, large uncertainties associated with these indirect methods and our prior knowledge of the Martian interior is still limited. Seismology remains the most direct and efficient way to probe the interior of a planet.

InSight landed in Elysium Planitia on 26 November 2018 and the SEIS (Seismic Experiment for Interior Structure) instruments were successfully deployed a few weeks later. These consist in a Very Broad Band (VBB) seismometer and a short period sensor to record Marsquakes and meteoric impacts. The VBB is an ultra-sensitive very broad band 3 axis oblique seismometer, which transforms the ground motion into analog electrical signals [Lognonné et al., 2019]. The VBB can record signals from quakes to meteoric impacts, and thus provide valuable constraints on Mars interior structure.

Generally, earthquakes with magnitude between 5 and 7 are preferred for seismic in-

versions based on waveform fitting, since smaller earthquakes suffer from low signal-to-noise ratio (SNR), while larger ones may have complicated focal mechanism and thus can no longer be approximated as point sources. Mars is not as geologically active as the Earth, so the number of Marsquakes with intermediate to large magnitudes is likely limited. This has been verified by the InSight SEIS data collected so far: most of the marsquakes detected during the first year of operation of SEIS have moment magnitude between 3 and 4 [Giardini et al., 2020]. Besides the limitation of the number of large enough events, other complications result from the fact that InSight only has one seismic station. Surface wave inversion techniques and receiver function analyses become thus natural choices to obtain models of Mars interior. While the first constraints on the properties of the shallow upper crust using InSight data and receiver functions were recently published [Lognonné et al., 2020], surface waves have not been detected yet. However, if they were to be observed in the future, dispersion measurements of fundamental and higher mode surface waves would provide depth constraints on the planet's internal structure, which was expected to be a primary means of constraining velocity structure by the Mars Structure Service (MSS) [Panning et al., 2017], and demonstrated by the MSS blind test [Drilleau et al., 2020]. In addition, the method presented in this chapter to measure dispersion data, and the modifications we brought to our original code to allow for less well-constrained reference models and source parameters, are extremely important for any planetary seismology application, including the likely future missions on the moon and on Titan (Dragonfly), as well as the ones that have been proposed for other bodies like Europa, Enceladus, from balloons on Venus, and even possibly on the surface of Mercury.

Surface wave dispersion data primarily constrain the path-averaged shear velocity structure between a station and a seismic event, with longer period data more sensitive to deeper structure. On Earth, fundamental mode surface waves, with their usually high SNR, are the most commonly used types of surface waves. For Earth applications, measurements at intermediate periods (between $\sim$30 s and 200 s) can resolve structure down to 200-300 km.

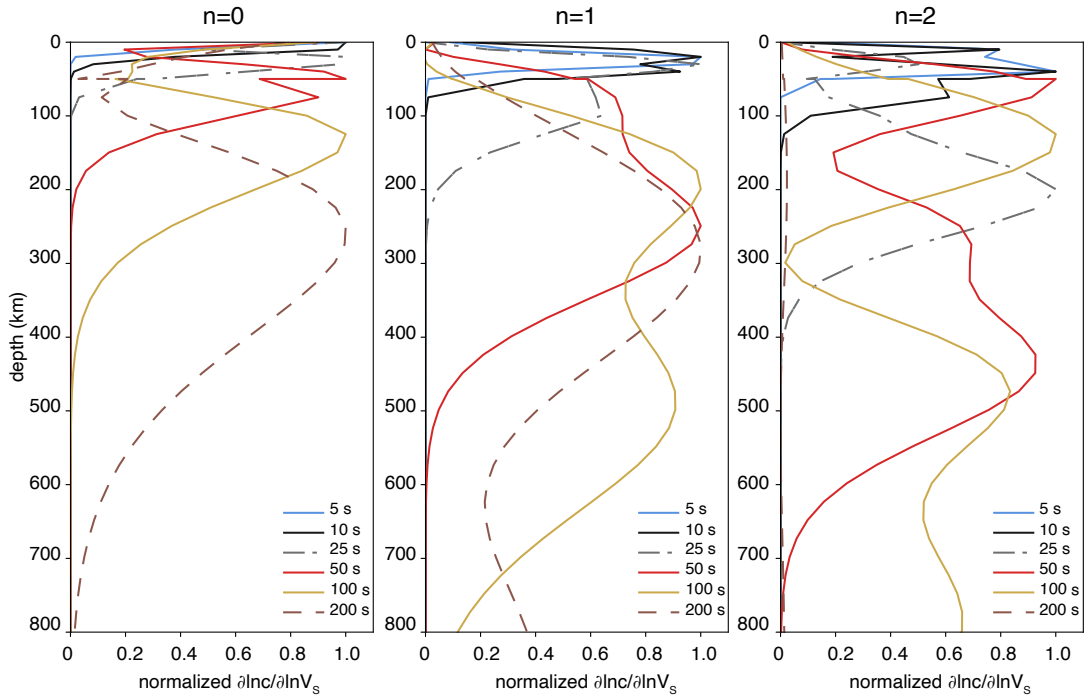

Figure 4.1: Sensitivity kernels $\partial \ln c / \partial V_s$ at different periods for fundamental mode surface waves (left), the first overtone (middle), and the second overtone (right) at periods between 5s and 200s. They were calculated using software package Mineos [Masters et al., 2011]. The model of Zheng et al. [2015] with no low velocity zone was used as reference.

Higher mode surface waves are less commonly used, but they carry unique, independent constraints on structure at greater depths. Higher modes (n > 0) surface waves are sensitive to deeper structure than fundamental modes at the same periods and can thus enhance the vertical resolution of surface wave tomographic models in the deep mantle. Examples of multiple-mode surface wave sensitivities calculated with software package Mineos [Masters et al., 2011] are shown in Fig. 4.1. For these partial derivative calculations, we used one of the Zheng et al. [2015] martian models as reference. More specifically, we chose the model that does not have a low velocity zone (LVZ), hereafter referred to as their noLVZ model.

Higher modes dispersion is undoubtedly more challenging to measure than fundamental mode surface waves due to their lower SNR and to the fact that the group velocities of differ-

ent modes overlap significantly in a broad frequency range. They usually do not appear as a clear wave train on the seismogram, and thus are difficult to separate. Methods developed to measure higher mode surface waves on Earth can be categorized into two groups: One group directly invert waveforms to get shear-wave velocity structure (e.g., Cara and Lévêque [1987], Nolet [1990], Lebedev and Nolet [2003], Li and Romanowicz [1995], Li and Romanowicz [1996]), and the second group measures higher mode phase velocity dispersion curves that are then inverted for structure [Cara, 1978; Nolet, 1975; van Heijst and Woodhouse, 1997b, 1999b; Beucler et al., 2003].

The method presented here was modified from that of Xu and Beghein [2019], which itself was inspired by the techniques of Yoshizawa and Kennett [2002] and Visser et al. [2007]. The idea is to perturb the path-averaged 1-D shear velocity profile to fit the data in a nonlinear waveform inversion and calculate the corresponding phase velocities at different periods. Our method takes advantage of the flexibility of the reversible jump Markov Chain Monte Carlo (rj-MCMC) approach [Bodin and Sambridge, 2009] to perform a thorough yet efficient sampling of the shear-wave velocity model space to fit the filtered multi-mode waveform. The posterior distributions of shear-wave velocity models and corresponding phase velocity dispersion curves can be estimated from the ensemble of V_S models sampled. We adapted our method to Mars and present it in this chapter. We first provide information regarding the rj-MCMC method and how we apply it to our problem. We then discuss in detail the modifications brought to the original method to deal with complications pertaining to InSight, including the lack of a good reference model and the large errors in source parameters. Finally, we present applications of our technique using a blind InSight dataset distributed to the MSS team [van Driel et al., 2019; Drilleau et al., 2020] as well as another synthetic dataset we created and to which we added realistic noise based on real recordings by the VBB.

4.2 Method

The method presented here is a waveform fitting technique based on the work of Xu and Beghein [2019], which was originally developed for Earth applications and was modified here to adapt to Mars. Details of the original method are also described in Chapter 2. The primary goal is to find models of Mars interior that fit the observed long-period waveforms. Our technique adopted the rj-MCMC method of Bodin and Sambridge [2009] and Bodin et al. [2012] to perform an efficient transdimensional model space search and to seek all possible path-averaged 1-D V_S models that can fit the filtered waveform. Our method additionally enables us to use these models to measure the dispersion of fundamental and higher mode surface waves. We will be able to use these dispersion curves in future work in combination with other data sets, thereby improving the resolution of the initial path-averaged interior models.

In this section we briefly summarized the framework of our original inversion method, which was described in Xu and Beghein [2019] in details, and emphasize the improvements we made to adapt it to studying Mars.

4.2.1 Waveform Modeling

Synthetic seismograms can be calculated by normal mode summation (See equation 3.1). Similar to what we did for Earth applications in previous chapters, we linearized the calculation of eigenfrequencies for Mars in order to accelerate the forward modeling computations. For the P-wave speed scaling, we used a linearly varying scaling relation, with $m_\alpha = 0.8$, and for the density scaling, we set m_ρ to 0.3 [Anderson et al., 1968]. These choices do not typically affect the V_S models in Earth applications so we do not expect it to play an important role here either. The shear-wave velocity is allowed to change by $[-10\%, +10\%]$ relative to the reference model. While the depth of mantle discontinuities has been shown to not be resolved by surface wave data [Meier et al., 2009], the crust thickness has been shown to

have strong nonlinear effects on waveform modeling and phase velocity calculations [Montagner and Jobert, 1988]. We thus included perturbations in the depth of the crust-mantle boundary in our inversion scheme and allowed it to vary by 5 km around the Moho depth in the reference model.

An important point to make here is that we need a good reference model for these assumptions of small perturbations to be valid. This may generally be an achievable goal for Earth since we have very good reference and 3-D models of its interior. However, we do not currently have a good reference model for Mars, which is one of the reasons for the InSight mission. In an attempt to circumvent this issue and to get better model uncertainty estimates than can be obtained with our linearized approach, we test different mantle models with different starting Moho depths and perform the model space search multiple times. This is not an ideal scenario but, as explained above, it is one with more reasonable computational costs. As the mission continues and models of Mars interior become available, these issues will become less important.

4.2.2 Source Parameter and Cycle Skipping Considerations

The phase velocity at angular frequency ω for a seismogram recorded at time t and distance x from an earthquake is given by:

$$c(\omega) = \frac{\omega x}{\omega t + \Phi_i(\omega) + 2n\pi - \Phi(\omega)} \tag{4.1}$$

where Φ_i includes the initial phase at the earthquake and any phase shift introduced by the seismometer and $\Phi(\omega)$ is the total phase of the seismogram, which can be obtained by Fourier transform of the time-series. The $2n\pi$ term reflects the periodicity of the complex exponential that describes the displacement produced by a plane wave.

Phase velocity measurements and synthetic waveform calculations on a single-station therefore require accurate knowledge of the event locations and focal mechanism. In Earth studies, these source parameters are generally determined prior to the inversion for structure

and the GCMT catalog [Dziewonski et al., 1981; Ekström et al., 2012] is a common choice in long-period waveform modeling (e.g., Yoshizawa and Kennett [2002]; Visser [2008]). However, even on Earth where multiple receivers are usually employed to constrain the earthquake source parameters, these parameters have non-zero uncertainties and can be biased by the choice of the reference Earth model used to obtained them.

Ideally, one should recalculate source parameters jointly with structure during the inversion to constrain the interior model more reliably [Valentine and Woodhouse, 2010]. This is not often done in practice but in the case of the InSight mission this may be a crucial part of the inversion since we only have one seismometer and no good reference model yet. The source parameters constrained by the Mars Quake Service (MQS) team of the InSight mission are thus expected to have even larger uncertainties than for quakes happening on Earth and propagating these uncertainties will be an important step in our search for Mars interior models. We thus modified our original code [Xu and Beghein, 2019] to include source parameters in the rj-MCMC sampling scheme, allowing us to vary them around the values reported by the MQS team and thereby enabling the propagation of source errors into the velocity models.

Because of the 2π ambiguity in Eq. 4.1, care must be taken when inverting single seismograms for phase velocities. Cycle skipping can happen when the reference model deviates too much from the true model. To avoid this, one often tries to "lock" the $2n\pi$ term in the correct phase at the longest periods (100 s to 150 s), and assumes the dispersion curve is smooth and continuous to extrapolate to the correct number of cycles at shorter periods. This helps infer short period phase velocities without ambiguity. This locking is usually done by choosing good reference model (e.g., Visser [2008]) or by adding extra constraints from the envelopes of the filtered seismogram [Yoshizawa and Ekström, 2010]. Here, because we do not have a good 3-D reference Mars model yet, we opted to test two methods: in one we simultaneously invert the waveform and the envelope as in Yoshizawa and Ekström [2010] and in the other we invert both waveform and group velocity dispersion curve. Group ve-

locities can be measured with other techniques and serve as independent constraints on the sought-after 1-D average structure. By including information from group velocities, we narrow down the range of V_S profiles. In this project, we compare the results between inversions including envelopes and group velocity data.

4.2.3 Misfit Function

When calculating a misfit from multiple types of data (in this case waveform and envelope or waveform and group velocities), it is important to determine the proper weights for each of the data sets. In this study, we adopted a L_2 norm and the misfit of each data type was normalized by the sum of squares of the data. The normalization operation guarantee that the amplitudes of different types of misfits are comparable.

For the joint waveform and envelope inversion, the misfit function is thus:

$$\text{Misfit}(\mathbf{m}) = \frac{\sum_{i=0}^{N}(w_{p,i} - w_{d,i})^2}{\sum_{i=0}^{N} w_{d,i}^2} + \frac{\sum_{i=0}^{M}(e_{p,i} - e_{d,i})^2}{\sum_{i=0}^{M} e_{d,i}^2} \tag{4.2}$$

where w and e denotes the waveform and the envelope, respectively, and N and M are their respective number of data points. The subscripts p and d represent predicted (synthetic) and observed values, respectively.

For the joint waveform and group velocity data inversion the misfit function is defined as:

$$\text{Misfit}(\mathbf{m}) = \frac{\sum_{i=0}^{N}(w_{p,i} - w_{d,i})^2}{\sum_{i=0}^{N} w_{d,i}^2} + \frac{\sum_{i=0}^{M}(U_{p,i} - U_{d,i})^2}{\sum_{i=0}^{M} U_{d,i}^2} \tag{4.3}$$

where M is now the number of group velocity measurements, and U_p and U_d denotes the predicted and measured group velocities, respectively. The group velocity dispersion measurements we used in this study were presented in Drilleau et al. [2020]. They were measured using a method based on probability density functions and described in Panning et al. [2015].

4.2.4 Bayesian Inference

We solve the inverse problem in a Bayesian framework, where model parameters are described by probability density functions (PDFs). The *posteriori* probability distributions of model parameters describe the uncertainties associated with these parameters. The posterior is given by Bayes' theorem:

$$p(\mathbf{m}|\mathbf{d}_{obs}) \propto p(\mathbf{d}_{obs}|\mathbf{m})p(\mathbf{m}) \tag{4.4}$$

where $A|B$ means A given (or conditional on) B, i.e. the probability of having A when B is fixed. $\mathbf{m}$ is the vector of model parameters and $\mathbf{d}_{obs}$ is the observed data. $p(\mathbf{d}_{obs}|\mathbf{m})$ is the likelihood function, which shows the probability of observing data $\mathbf{d}_{obs}$ given a particular model $\mathbf{m}$. The *a priori* probability of model, $p(\mathbf{m})$, contains what we assume about the model $\mathbf{m}$ before having the observed data. In this study, we adopted a similar prior distribution, $p(\mathbf{m})$, as in our previous work [Xu and Beghein, 2019]: model parameters are assumed to have uniform prior distributions with relatively wide bounds so that the final posterior distribution is dominated by the data.

The likelihood function $p(\mathbf{d}_{obs}|\mathbf{m})$ describes the probability of data given the current model. As is described in Xu and Beghein [2019], if we assume the data noise in the waveform follows a multivariate normal distribution with zero mean and covariance matrix $\mathbf{C}_d$, then the likelihood term can be expressed in this form:

$$p_i(\mathbf{d}_i|\mathbf{m}) = \frac{1}{\sqrt{(2\pi)^n|\mathbf{C}_{d_i}|}} \times \exp\left[-\frac{\Phi_i(\mathbf{m})}{2}\right] \tag{4.5}$$

where i is the index for different frequency-time windows. $\Phi_i(\mathbf{m})$ is the function describing the distance between the real data and the synthetics predicted by the current model. As in Xu and Beghein [2019], we assumed the Gaussian noise to be uncorrelated, in which case the covariance matrix $\mathbf{C}_d$ becomes diagonal. The $\Phi(\mathbf{m})$ term is then simplified to:

$$\Phi_i(\mathbf{m}) = M_i(\mathbf{m})/\sigma_i^2 \tag{4.6}$$

where M_i is the L2 norm between data and synthetics predicted by current model. σ_i is the standard deviation of the Gaussian uncorrelated noise in the ith frequency-time window.

In this study, the misfit function describes the errors between different types of observed data and values predicted by models. For the misfit function, we assumed equal relative variance as a percent of amplitude for all inverted parameters. We also decided to assign the same adaptive noise levels to the two data types to guarantee that our Hierarchical Bayesian inversion won't favor one data type over the other too. The standard deviation of the Gaussian uncorrelated noise accounts for both the primary misfit of the waveform fitting and the secondary misfit of the envelope or group velocity fitting. Here we use a different notation, σ_i^* instead of σ_i, to denote the normalized overall standard deviation of the noise.

With all these assumptions, the updated likelihood function is given by:

$$p_i(\mathbf{d}_i|\mathbf{m}) = \frac{1}{\sqrt{(2\pi)^n(\sigma_i^*)^{2n}}} \times \exp\left[-\frac{\text{Misfit}_i(\mathbf{m})}{2\sigma_i^{*2}}\right] \tag{4.7}$$

As is shown in Chapter 2, the overall standard deviations are considered as unknowns in the Hierarchical Bayesian inversion, rather than being fixed at a presumed level as in traditional inversion methods. This allows us to invert for the unknown noise level in addition to the targeted parameters and reduces the risk of mapping noise into the models.

4.2.5 rj-MCMC Inversion Scheme

Details of the rj-MCMC method for Earth were discussed in Chapter 2. For Mars application, two additional types of parameters are included as free parameters during the sampling: depth of the crust-mantle boundary, and the source parameters. In our new inversion scheme for Mars, there are seven types of perturbations of the current hyperparameters in order to get the next iteration:

1. Change the velocity of one interpolation point;

2. Change the depth of the crust-mantle boundary;

3. Change the source parameters (focal depth, strike, slip and dip);

4. Birth: create a new interpolation point;

5. Death: remove one interpolation point at random;

6. Move: Randomly pick one interpolation point and move it to a new depth;

7. Change the noise level;

During the Birth step, we add a new interpolation point at a certain depth, so that the model complexity around that depth increases to account for more complicated structure. During the Death step, we randomly remove one interpolation point to make the model representation more efficient at depths without large Vs anomalies. The Markov Chain is generated for hundreds of thousands of iterations. The first part of the Markov Chain, or burn-in period, is discarded, after which the random walk is assumed to be stationary and it begins the sampling of the model space according to the posterior distribution. Here, we used 180,000 as the burn-in length, followed by 60,000 samplings for each Markov Chain.

4.3 Tests and Results

In this section, we present different tests to illustrate our method and determine how well it can recover an input model. One of the tests performed made use of a blind data set [van Driel et al., 2019] that was distributed to the MSS team to validate multiple methodologies proposed to estimate Marsquake locations and 1-D Martian structures between source and receiver [Drilleau et al., 2020]. Other tests were conducted using our own synthetic data sets because the MSS blind data did not display any higher modes in the frequencies for which our method is reliable, as explained below.

4.3.1 Blind Test

4.3.1.1 Blind Test Data and Reference Model Search

The synthetic data set that was distributed to the MSS and MQS teams was generated using a 3-D crust model overlaying a 1-D base model from the Moho discontinuity to the core and synthetic noise was added to the waveform. All parameters of the Martian model and the Marsquake were unknown during the blind test period. The MQS team first calculated a reference focal depth of 36 km using the arrival time of the pP phase and an assumed crustal velocity of 5 km/s. They then determined the posterior distributions for focal depth and focal mechanism parameters [Böse et al., 2017; Drilleau et al., 2020] using the method of Stähler and Sigloch [2016]. In this project, we employed the mean and width of these distributions as prior values for the source parameters in our waveform modeling.

We used the vertical component of the blind data set with the goal of measuring Rayleigh wave dispersion. The raw data were filtered in different frequency bands, but no clear signals of higher mode Rayleigh wave were visible. The fundamental mode Rayleigh waves were, however, clearly visible at periods between 25 s and 50 s (Fig. 4.2). This absence of clear surface waves at long period ($>$ 50 s) is consistent with true Martian noise levels [Banerdt et al., 2020]. If the real VBB noise level is larger at long periods than at shorter periods, surface waves on Mars are generally going to be more difficult to measure at periods $>$ 50 s since their signal-to-noise ratio is expected to be lower than at shorter periods.

The first step in our procedure was to find a suitable reference model to calculate the waveform. We thus calculated waveforms using Mineos for several published 1-D Mars interior models (e.g., Zheng et al. [2015], Sohl and Spohn [1997]) using the source parameters determined by the MQS team. The estimated Marsquake location, depth, magnitude as well as origin time we employed are listed in Table 4.1. We found that the seismogram calculated using model noLVZ (no Low Velocity Zone) from Zheng et al. [2015] resembled the filtered blind waveform the best, apart from a time-shift of about 300 s (Fig. 4.2). We then performed

Table 4.1: Comparison between MQS-estimated and true source parameters.

Event parameters	Computed origin	True origin
Origin time (UTC)	2019-01-03 15:00:53.0	2019-01-03 15:00:30.0
Lat(°)	26.0 S	26.443 S
Lon(°)	53.0 E	50.920 E
Depth (km)	38.4	38.4
Magnitude	MsM=3.7 (Mw=4.2)	Mw=4.46

a rough grid search to change both the V_S profile and the depth of the crust-mantle boundary to time-shift the synthetic waveform closer to the blind test waveform. It should be noted that the model considered for the blind test was comparable to those included in Smrekar et al. [2019], which did not include either the Sohl and Spohn [1997] model or the Zheng et al. [2015] models, making this test of our method more realistic.

4.3.2 Waveform Modeling: Effects of the Source Parameters

Because the uncertainties in the estimated source parameters by a single-station method can be large and underestimated, we included the focal mechanism as free parameters during our MCMC sampling. This helps avoid the propagation of errors in the the quake source into the interior model. We let the focal mechanism parameters and the source depth vary using prior uniform distributions with ranges roughly matching the MQS error estimates. The source latitude, longitude and origin time were kept fixed due to the strong trade-offs between source location and travel time. The magnitude was also kept constant and equal to the MQS estimate. The amplitude mismatch between the MSS blind test data and the predicted waveforms were corrected by energy equalization rather than including source magnitude simultaneously in the MCMC sampling, as the latter may result in the instability of the MCMC algorithm as explained in Xu and Beghein [2019]. Details about the source priors are given in Table 4.2.

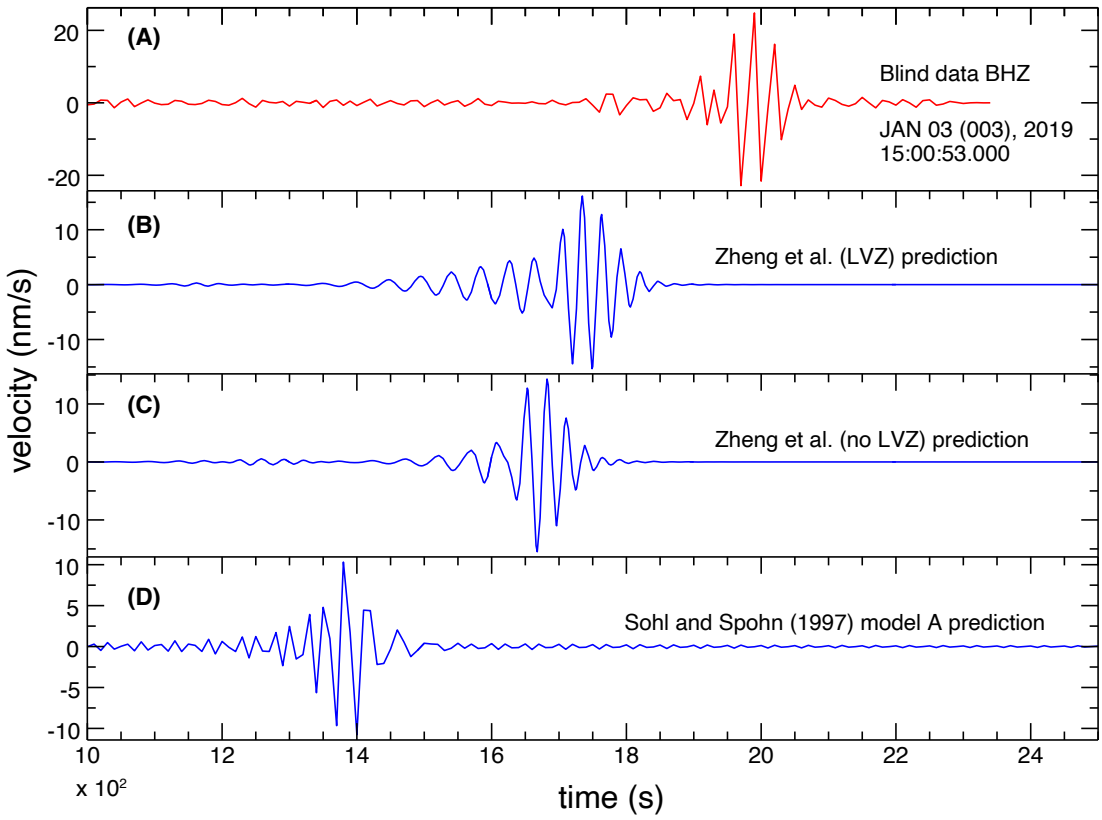

Figure 4.2: Comparison of the MSS blind test waveform (A) and synthetic waveforms predicted by three different reference models: (B) model LVZ by Zheng et al. [2015], which included a low velocity zone; (C) model noLVZ by Zheng et al. [2015] without Low Velocity Zone; (D) Sohl and Spohn [1997]'s model A. All traces were bandpass-filtered between 25 s and 50 s.

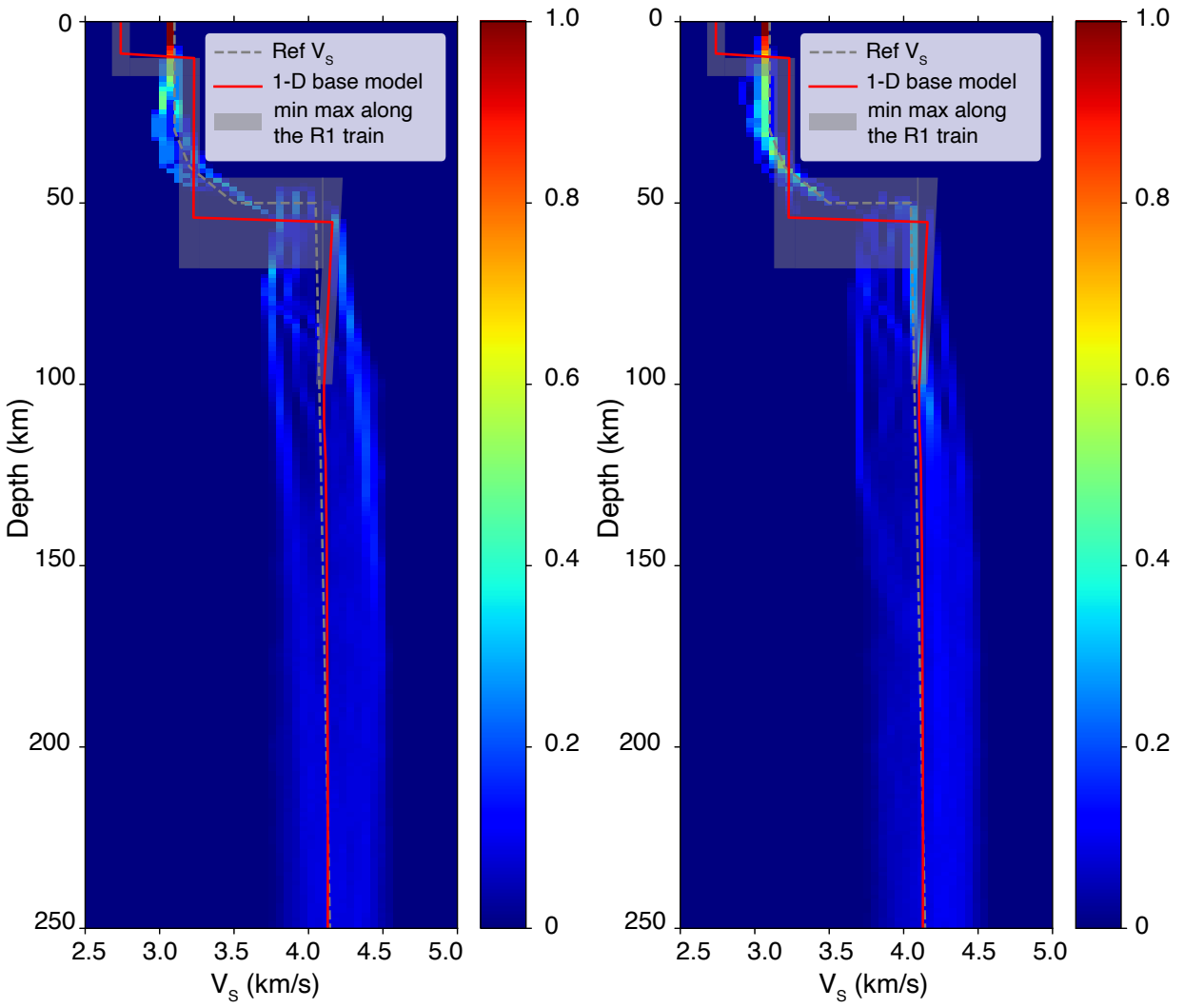

Figure 4.3: Inversion results with fixed source parameters (left) and free source parameters (right). The gray dashed line represents the reference model used for MCMC sampling and partial derivative calculations. The red line is the 1-D base model used to compute the blind test data. The gray shaded area is for the maximum and minimum V_S and Moho depth along the source-receiver path based on the 3-D crust model used to generate the blind test data. The color scale represents the likelihood of a given model parameter.

Table 4.2: Prior (uniform) distributions of source parameters used for the rj-MCMC sampling.

Focal mechanism parameters	Prior range
Strike(°)	85 - 135
Slip(°)	40 - 60
Rake(°)	50 - 100
Depth(km)	36.4 - 40.4

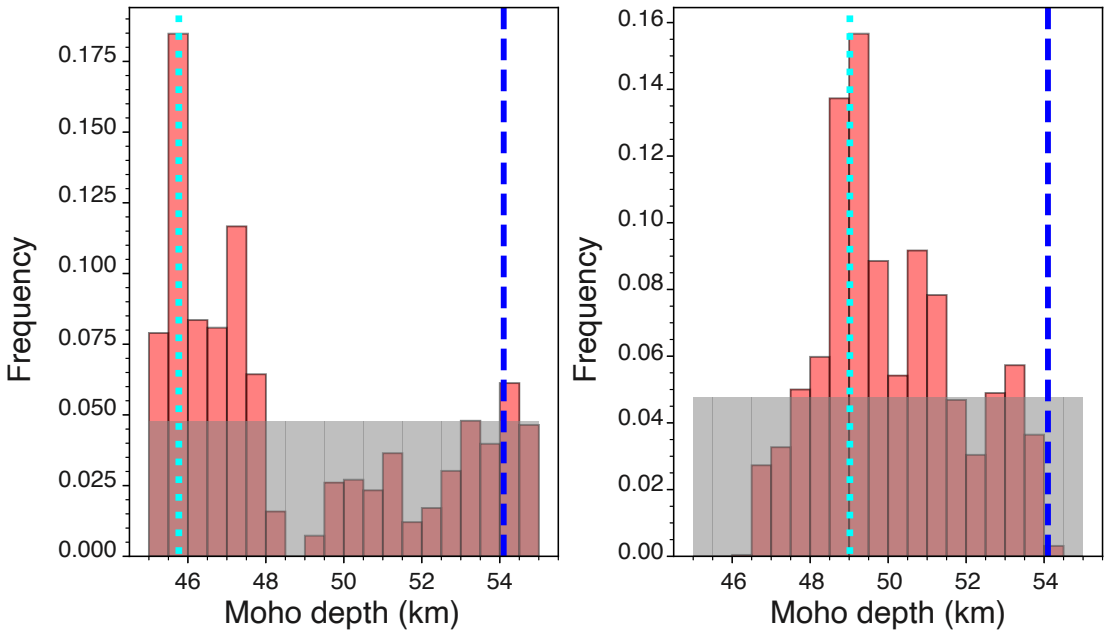

Figure 4.4: Posterior distributions of Moho depth in the fixed-source test (left) and in the free-source test (right). The dark blue dashed lines represent the Moho depth in the 1-D base model used to generate the MSS blind test data. The light blue dotted line represents one of the best fitting values.

Figs. 4.3 and 4.4 compare results of inversions performed using fixed source parameters and inversions in which the focal mechanism and focal depth were allowed to vary as explained above. Waveform envelopes were used as constraints to avoid cycle skipping. The fixed source values employed were the mean values shown in Table 4.2. The reference model used for both tests was the modified model of Zheng et al. [2015] as previously described and is represented by the dashed grey line. The color scale in Fig. 4.3 represents the likelihood of a given V_S model parameter. Because the model used to generate the blind test data contained a 3-D crustal model, there is a range of V_S values and Moho depths along the source-receiver great circle path in addition to the base 1-D model that is shown in red. This range is represented by the shaded area. Fig. 4.4 shows that both the free-source test and fixed-source test favor a shallower Moho than the true value in the 1-D base model. The fixed-source test also shows a bi-modal distribution for the Moho depth, with the highest peak at about 46 km. This bi-modal pattern does not exist in the free-source test, which likely reflects the existence of trade-offs between source parameters, Moho depth, and V_s.

Fig. 4.5 shows how the misfit change with the iteration number in both tests. On average, the two ensembles of models have similar misfits. Statistical F-tests [Bevington et al., 1993] were performed on a number of "best" models selected in each ensemble to determine to which the level of confidence the difference between model misfits is significant. They revealed that the two sets of inversions explain the data equivalently well. We would like to point out, however, that although the free-source inversion results do not necessarily fit the data better than to the fixed-source inversion, the former is still preferred to avoid mapping errors in the source into the velocity models since the source parameters were determined by a single station.

Fig. 4.6 represents the source parameter posterior distributions obtained in the free source inversion in comparison to the true values used to generate the MSS blind data. Since the source is a double couple, the two complimentary planes calculated from the true source moment tensor are also plotted for comparison. We found that our posterior distribution for

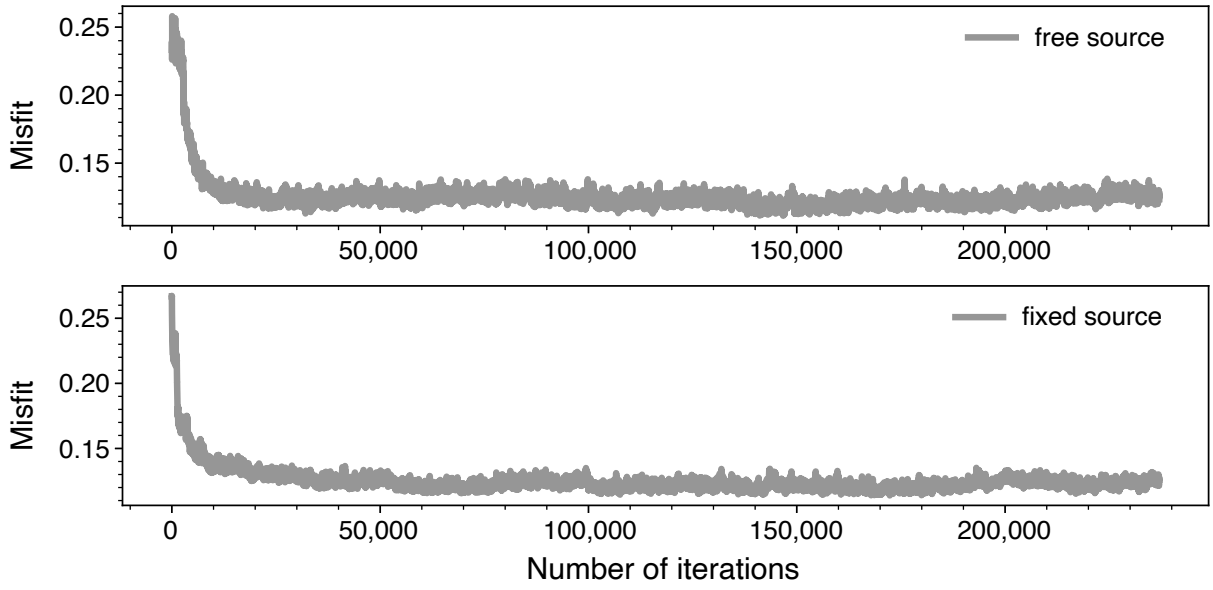

Figure 4.5: Waveform fitting misfits as a function of iteration number for free source MCMC sampling (top) v.s. fixed source MCMC sampling (bottom).

the strike includes and peaks near one of the two solutions calculated from the true source. Both possible values for the true dip are, however, outside the search range estimated based on the MQS results. The posteriors for the slip and focal depth both show a relatively uniform pattern, which include but do not prefer the true values. But the posterior distribution of the strike fits well if we regard the plane 2 as the true plane. The reader should be reminded that our method should, of course, not be considered as a way to jointly constrain the source parameters as well as the Martian structure. The source parameters were included to reduce the mapping of errors in the quake focal mechanism and depth into the velocity models.

4.3.3 Effects of Reference Crustal Thickness

The Moho depth in a Martian model can have significant influence on the synthetic waveforms, so we allowed it to vary in $\pm$ 5 km relative to the reference model using a linearized perturbation method as shown in Equation 3.2. However, this search range was still too

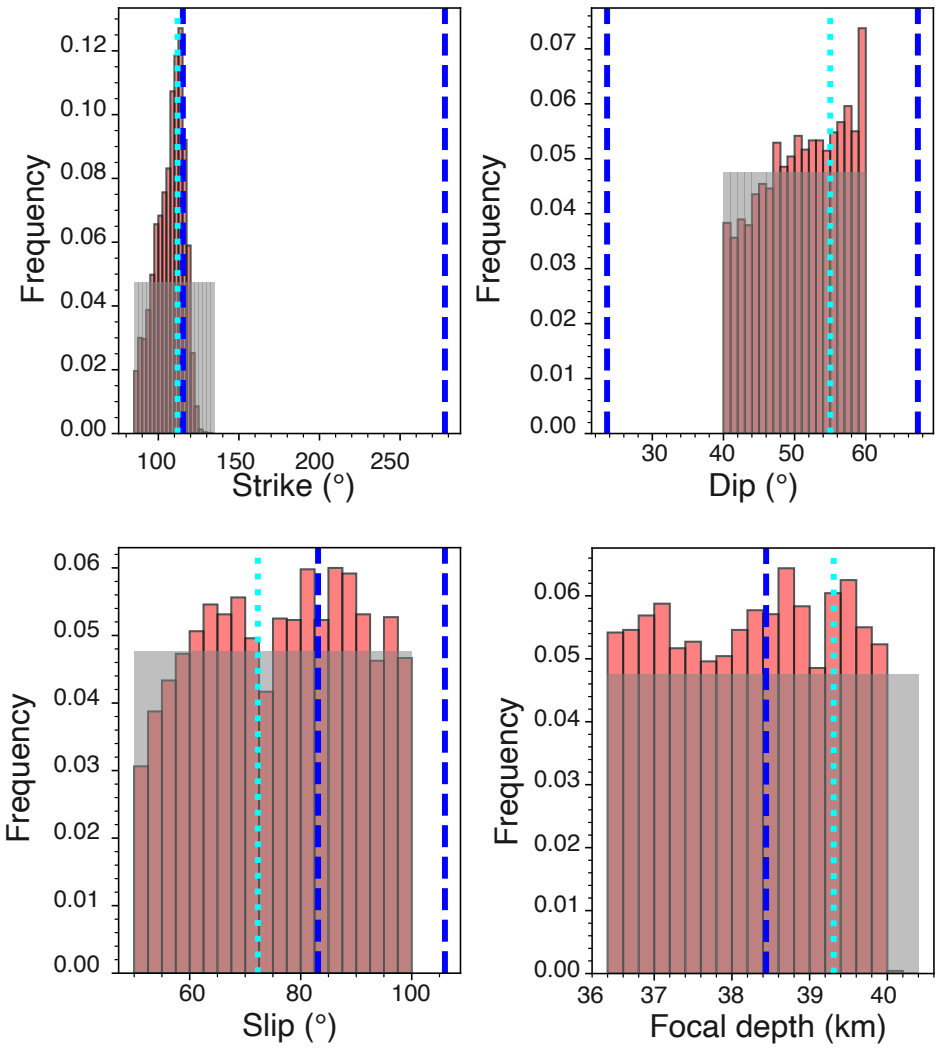

Figure 4.6: Posterior distributions of strike, dip, slip, and focal depth (red shaded area) for the inversion with free source parameters shown in the right panel of Fig. 4.3. The prior distributions used for each of those parameters are represented by the shaded grey areas. The true values used to generate the MSS blind test data are shown by the dark blue dashed lines, including the strike, dip and slip for both planes calculated from the true source moment tensor. The best fitting parameters obtained by the MCMC sampling are indicated by the dotted line.

limited to cover a wide enough set of possible Moho depths due to our yet poor prior knowledge of Martian interior. Consequently, we ran our inversions multiple times, using different reference models with different Moho depths. To generate these new reference models, we changed the crustal thickness of the Zheng et al. [2015] model and proceeded as explained in section 4.3.1.1: we adjusted the reference V_S in order to roughly match the synthetics with the observed blind test surface waves. In Fig. 4.7, we compare the results for model space searches done with a 50 km and a 75 km reference Moho depth. Note that while the 50 km reference Moho falls within the range of Moho depths along the source-receiver path that were used to calculate the blind test seismograms, the reference model with a 75 km Moho depth is outside of that range. Here, waveform envelopes were used as constraints to avoid cycle skipping.

An example of best fitting waveforms is shown in Fig. 4.8. We found that, on average, the inversions with a reference Moho depth at 50 km have a slightly lower misfit than the one with the Moho depth at 75 km. This may seem promising since the range of true Moho depth along the path did include 50 km and not 75 km depth. However, the difference in misfits did not appear to be significant and we could not simply exclude the second inversion due to its slightly higher misfit values. This is to be expected as fundamental mode surface waves alone cannot uniquely constrain both Moho depth and velocity due to the existence of trade-offs. By comparing the V_S posterior distribution to the true values used to generate the blind data, we found that the inversions with reference Moho depth at 50 km recover the true 1-D base model better. Not only does it find posterior Moho values closer to the true values, but we also see that starting from a Moho depth that is outside of the range of true values yields a set of V_S models that could be misinterpreted as constraining a high velocity lid if care is not taken. These observations highlight how important it will be to obtain prior, independent constraints on crustal structure (e.g. from receiver functions) in order for surface waveform inversions provide reliable velocity models.

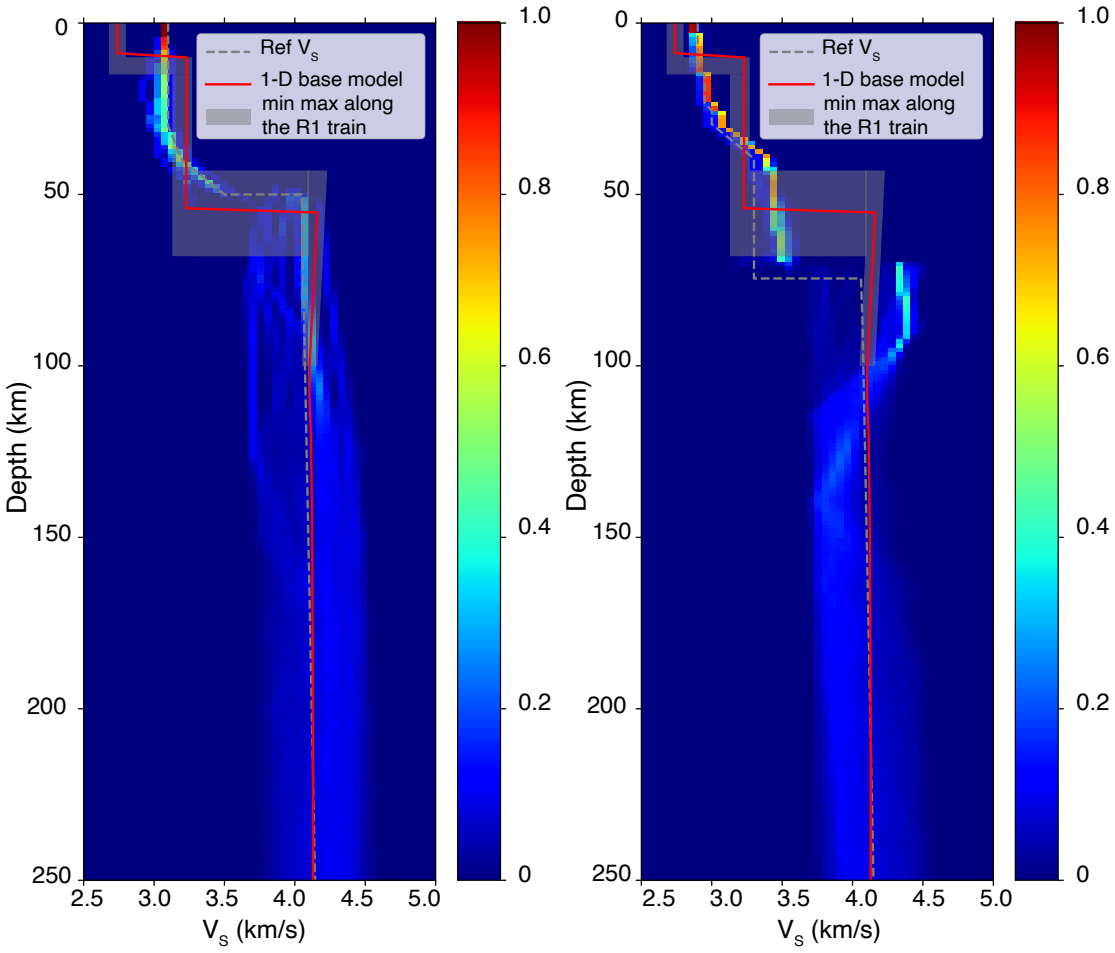

Figure 4.7: Ensemble of models resulting from inversions with waveform envelopes and starting models of different crustal thickness: 50 km (left) and 75 km(right). The color scale and different curves are described in Fig. 4.3.

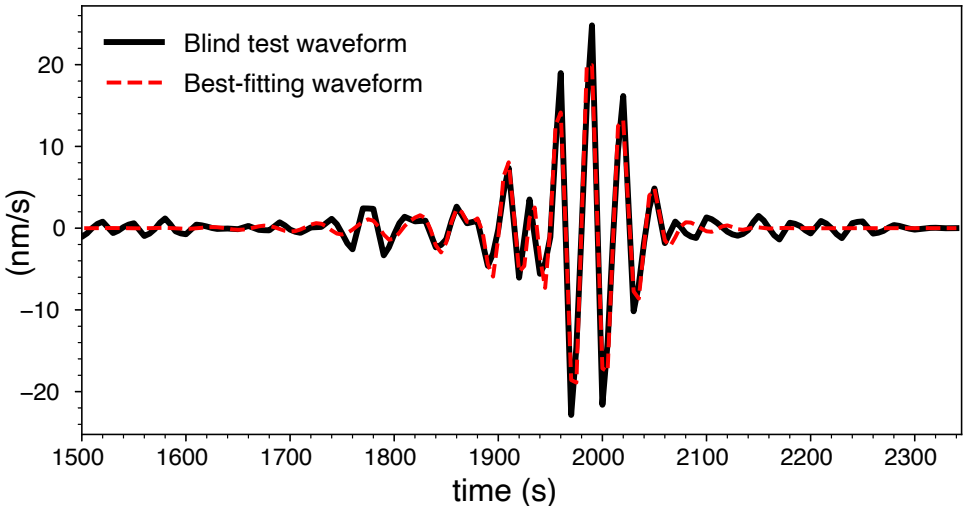

Figure 4.8: Best fitting waveforms for the test with Moho depth at 50 km

4.3.4 Effect of Envelopes and Group Velocities

Because the envelope fit can be strongly affected by the noise level, we also tested whether the inclusion of group velocity measurements instead of the envelope affects or improves the results. The misfit function in this case is given by Equation 4.3. We found that the V_S profiles (Fig. 4.9) do not strongly differ from those of Fig. 4.7, but the range of allowable V_S models is slightly larger with the group velocities than with the envelope.

Similar to Fig. 4.7, the mean misfit was slightly lower with the reference model that has a 50 km thick crust than with the 75 km thick thrust. But, again, the difference in average misfits was not significant, so neither of these two tests can exclude one crustal thickness. By comparing the inversion results with independent group velocity measurements included versus the inversion results with waveform envelopes in the previous section, we found these two strategies yield similar V_S posteriors. This is to be expected as the envelopes of waveforms mainly provide group velocity constraints on the V_S models, though group velocities may be preferable since the envelope can be affected by noise more strongly.

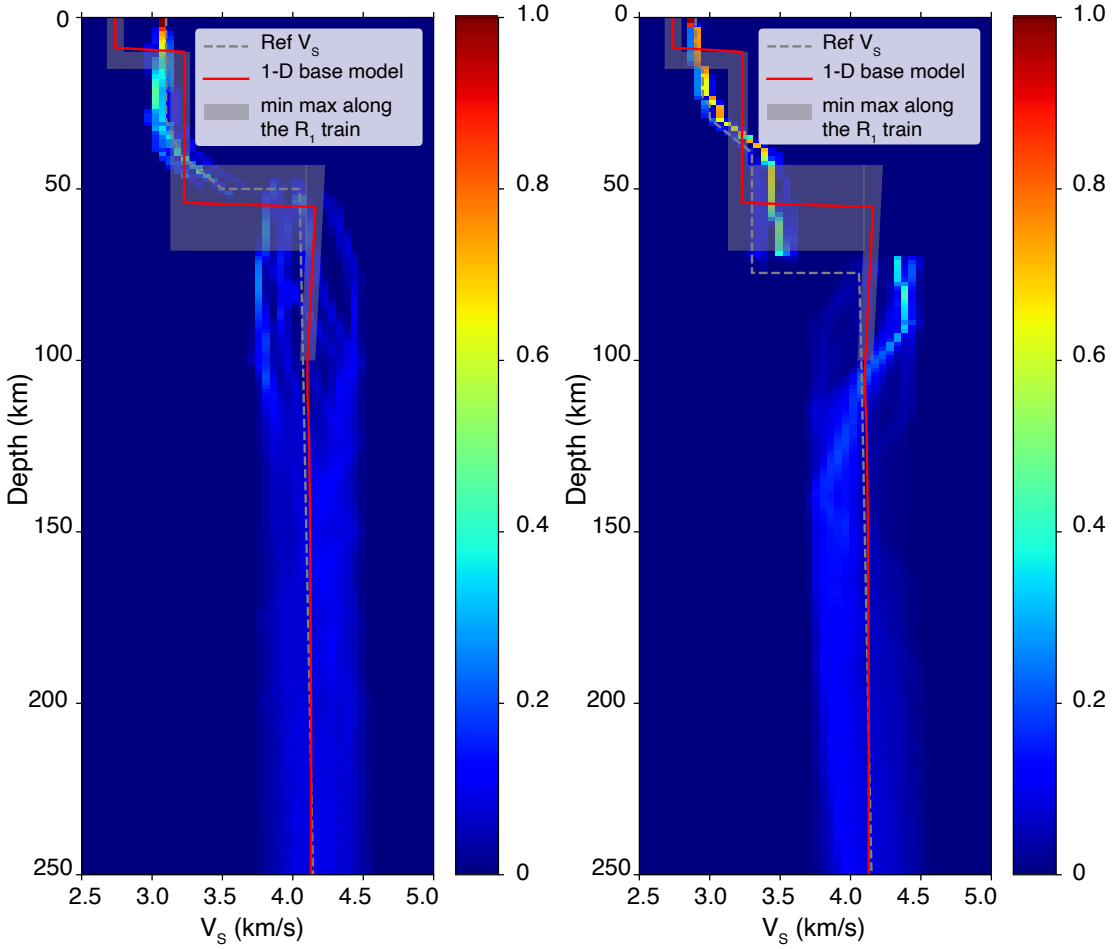

Figure 4.9: Ensemble of models resulting from inversions with group velocities and starting models of different crustal thickness: 50 km (left) and 75 km(right). The color scale and different curves are described in Fig. 4.3

.

We also obtained the posterior distributions of phase velocities from the ensembles of models for each test. The predictions for the 4 tests with free source parameters and for the true 1D base model are shown in Fig. 4.10. Note, however, that the phase velocities calculated from the 1-D base model should not, however, be treated as the true phase velocities since the 3-D crust effects on surface wave dispersion were not taken into account. Our inverted phase velocities are lower than the phase velocities of the 1-D base model. However, for tests with reference Moho depth at 50 km, the 2σ error bars contain the 1-D base model, while for tests with reference Moho depth at 75 km, their error bars barely contain the phase velocities predicted by the 1-D base model. Overall we found that the models that were obtained with a reference model whose Moho depth was included in the range of true Moho depths predict phase velocities that are closer to the 1-D base model predictions.

4.4 Additional Synthetic Test with Realistic Martian Noise

Since higher mode surface waves were not visible in the blind test waveforms, we created our own synthetic data set to test our method on a waveform with higher modes. We selected the noLVZ model of Zheng et al. [2015] to generate the synthetic waveform data due to its similarity to the MSS blind test 1-D base model. We calculated the vertical component synthetic waveforms with Mineos. Only the fundamental mode and the first 3 overtones were included for the purpose of this test.

In addition, we should point out that the forward modeling method used to generate the synthetic test data was the same as the forward modeling in the inversion, and a 1-D model was used to generate the synthetic data. This makes this synthetic test less challenging than the MSS blind test, for which the data were generated with a 3-D crust and a different algorithm than the one used for our forward modeling.

In order to generate data noise that represents a realistic overall noise level on Mars, we obtained noise amplitude information from the PPSD (Fig. 4.11). The phase information for

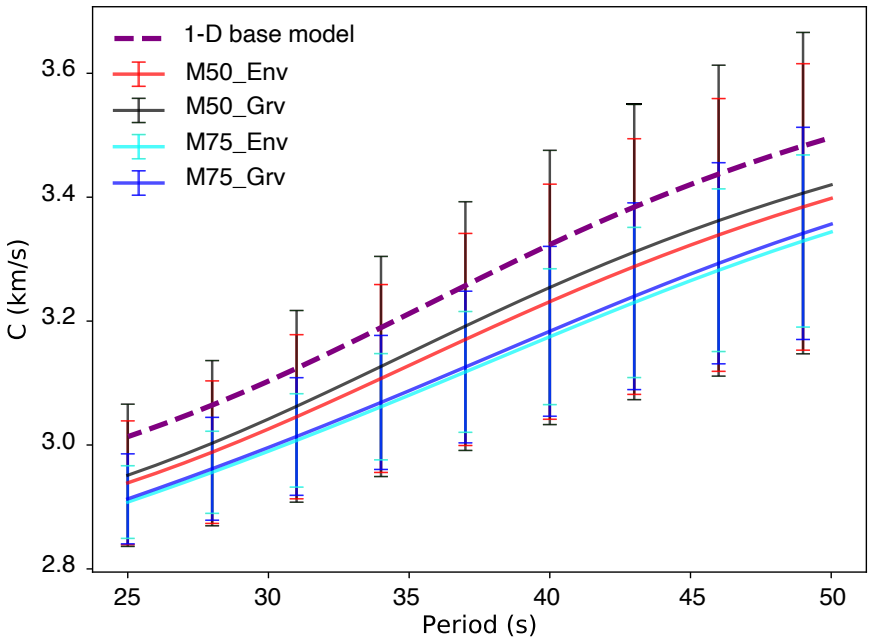

Figure 4.10: Measured phase velocity dispersion curves for the fundamental mode Rayleigh wave with two standard deviations obtained from the posterior distributions, and dispersion curve for the 1-D base model (purple dashed curve) used in the blind test. M50 and M75 represents the inversions with Moho depth at 50 km and 75 km, respectively. 'Env' stands for envelope and 'Grv' stands for group velocity.

.

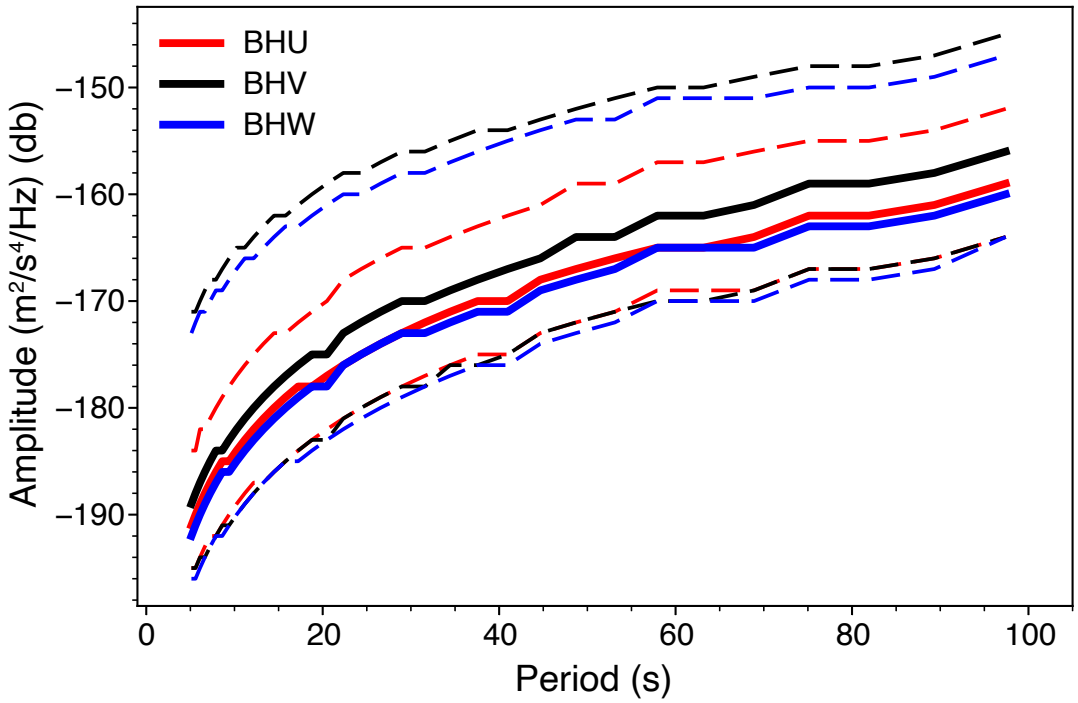

Figure 4.11: Probabilistic power spectral density (PPSD) measured during the "quiet" time (less windy) on Mars (18:00 – 23:00 LMST) in July 2019. The dashed lines mark the 10th and 90th percentiles. The PPSD was calculated using the method of McNamara and Buland [2004].

different periods were assigned randomly between $[0, 2\pi]$. Realistic Martian noise waveforms were calculated by inverse Fourier Transform of the amplitude and phase information, and were superimposed to the synthetic waveforms calculated by Mineos.

One way to generate waveforms with higher mode amplitudes larger than the ambient noise is by increasing the magnitude of the Marsquake. However, the likelihood to have a Marsquake larger than the quake used in the blind test is not high based on the observations we have from SEIS so far. Instead, we set the magnitude of the synthetic source at the same value as for the blind test ($M_w = 4.46$), and tweaked other parameters to find a scenario where the higher modes waveform is clear in the time domain and separates well from the

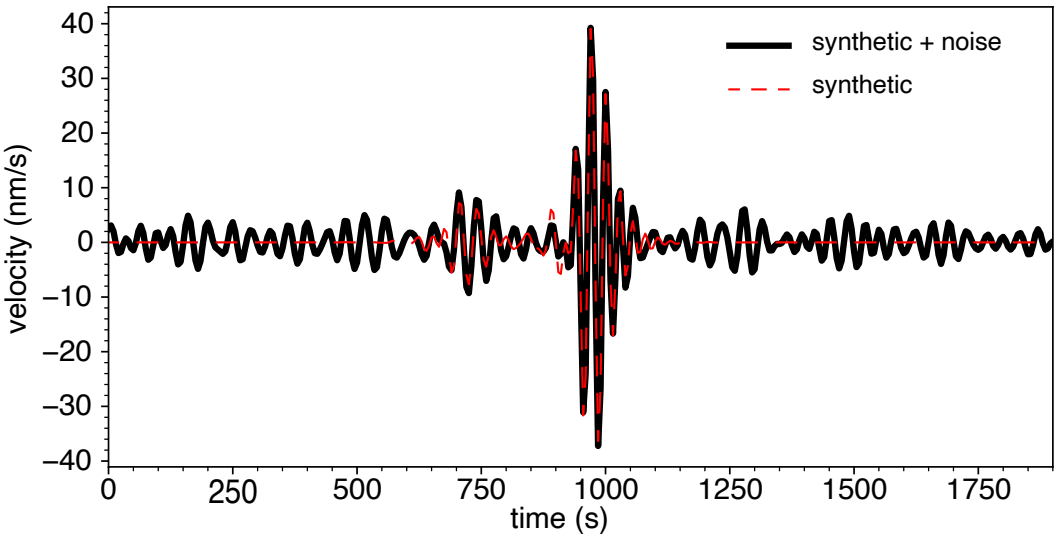

Figure 4.12: Vertical component waveform calculated using Zheng et al. [2015]'s model noLVZ and filtered at 25 s - 50 s. Realistic Martian noise was added to the synthetic waveform (thick black line)

.

fundamental mode. With these considerations in mind, we chose a focal depth of 40 km and an epicentral distance of 50 degrees.

The filtered synthetic data is shown in Figure 4.12. It was bandpass-filtered in the 25 s – 50 s period range and higher modes wave trains are visible between 650 s and 850 s, although the signal to noise ratio is on the low side. The goal of this synthetic test is to see whether our method can still resolve the higher modes and use them to constrain structure under a relatively realistic best-case scenario on Mars.

4.4.1 Results and Reliability Analysis

The procedures to invert this synthetic waveform is the same as for the blind test as described in details in the previous section. The reference model was created by randomly perturbing

the true model at a few depth nodes. We used waveform envelopes to avoid cycle skipping issues. Moho depth and source parameters were allowed to vary together with the velocity profile and the posterior noise level. The posterior V_S distribution is shown in Figure 4.13. We found that we can recover the true model well at most depths down to 400 km. The Markov Chains clearly converged toward the true model. We also noted that the posterior model distribution is narrower than for the blind test, likely due to the fact that the blind data set was generated with a 3-D model and ours was obtained with a 1-D model instead.

The posterior distribution of phase velocities for the multi-mode surface waves can be calculated using the posterior distribution of models. In theory, one can calculate an infinite number of modes from these models. However, in practice, not all of them will be resolved as higher modes tend to have weaker energies and low SNR in addition to overlapping in the time domain. A reliability analysis was thus performed to determine in which modes and at which periods the phase velocities were reliably measured with our technique. In practice, for each mode, we would only keep the measurements at periods with reliability scores higher than a defined threshold. Our reliability test considers the waveform fit and the intensities of each single mode in the time-frequency domain. Further details on this reliability analysis can be found in Xu and Beghein [2019]

The results of our reliability analysis for the fundamental mode and the first 3 overtones are given in Fig. 4.14. We found that the fundamental mode is reliably measured at all periods considered, which is identical to what is found for Earth since they have larger SNR and separate well from the higher modes. We also found, similar to Earth, that the higher modes are reliably measured at the shortest periods (<35 s in this case). Considering the sensitivity kernels for these first few higher modes (Fig. 4.1), this means that the data employed are sensitive to structure down to 300-400 km depth. In Fig. 4.15, we plotted the dispersion curves for the reliably measured modes in addition to the dispersion curves predicted by the true model. The measurements are displayed with two standard deviations. We found that in all cases, the dispersion values for the true model are included within the

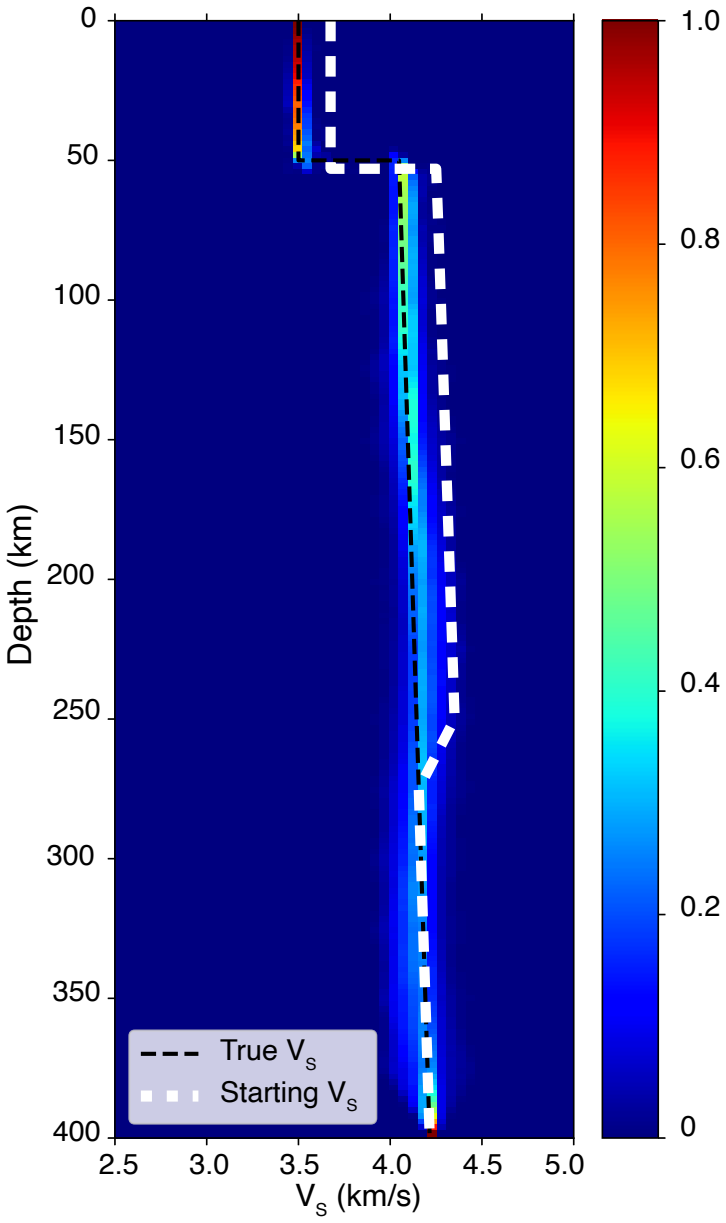

Figure 4.13: Ensemble of V_S solutions obtained from the MCMC sampling. The thin black dashed line represents the true model and the thick white line is for the starting model. The color scale represents the likelihood of a given model parameter.

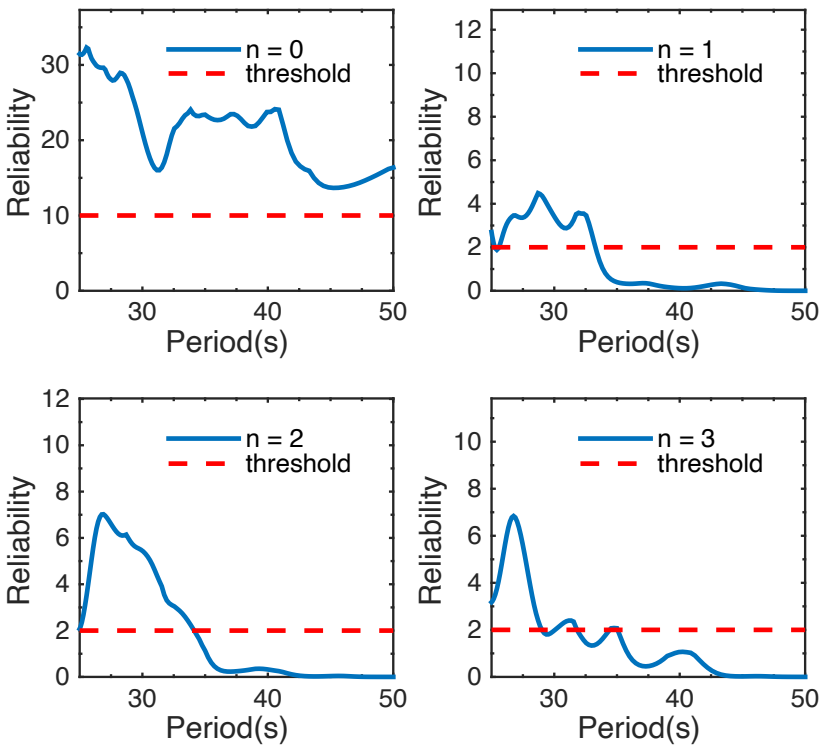

Figure 4.14: Reliability scores for the fundamental mode (n = 0) and first 3 overtones (n = 1, 2, or 3) as a function of periods. The horizontal red dashed lines indicate the empirical thresholds we defined for each mode. Only periods with reliability scores higher than the thresholds will be kept.

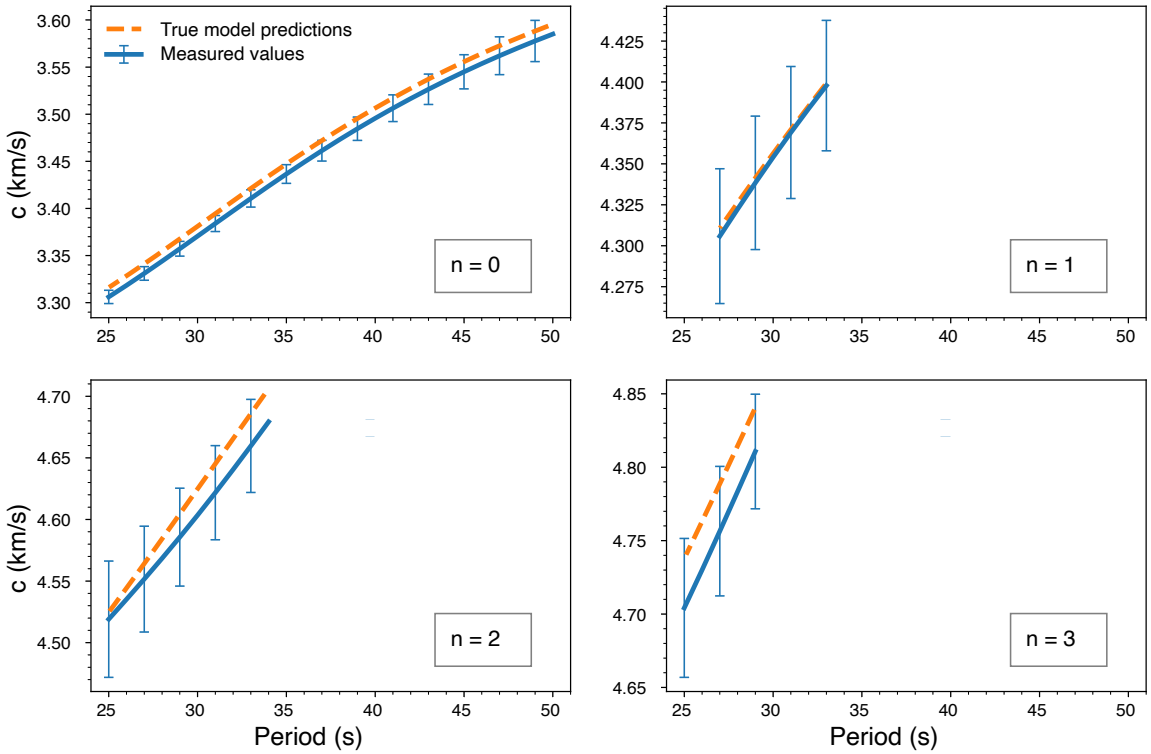

Figure 4.15: Measured phase velocity dispersion curves for the fundamental mode Rayleigh wave (n = 0) and the first 3 overtones (n = 1, 2, 3) with two standard deviations as error bars. The dispersion curves from the 1-D true model (dashed curve) were plotted for comparison.

2σ uncertainties estimated with our method.

In Fig. 4.16, we showed the posterior distributions of the source parameters and Moho depth. Even though the initial model is relatively close to the true model, especially in terms of the Moho depth, we cannot reliably use the posterior distributions of the source parameters as direct estimations of the true source. We interpret this as the outcome of strong source-structure trade-offs in this inversion problem.

Before concluding, we should remind the reader that our results do strongly depend on having a good reference model. Further analysis of the resolvability of Mars structure with higher modes under different conditions will be performed in a later study.

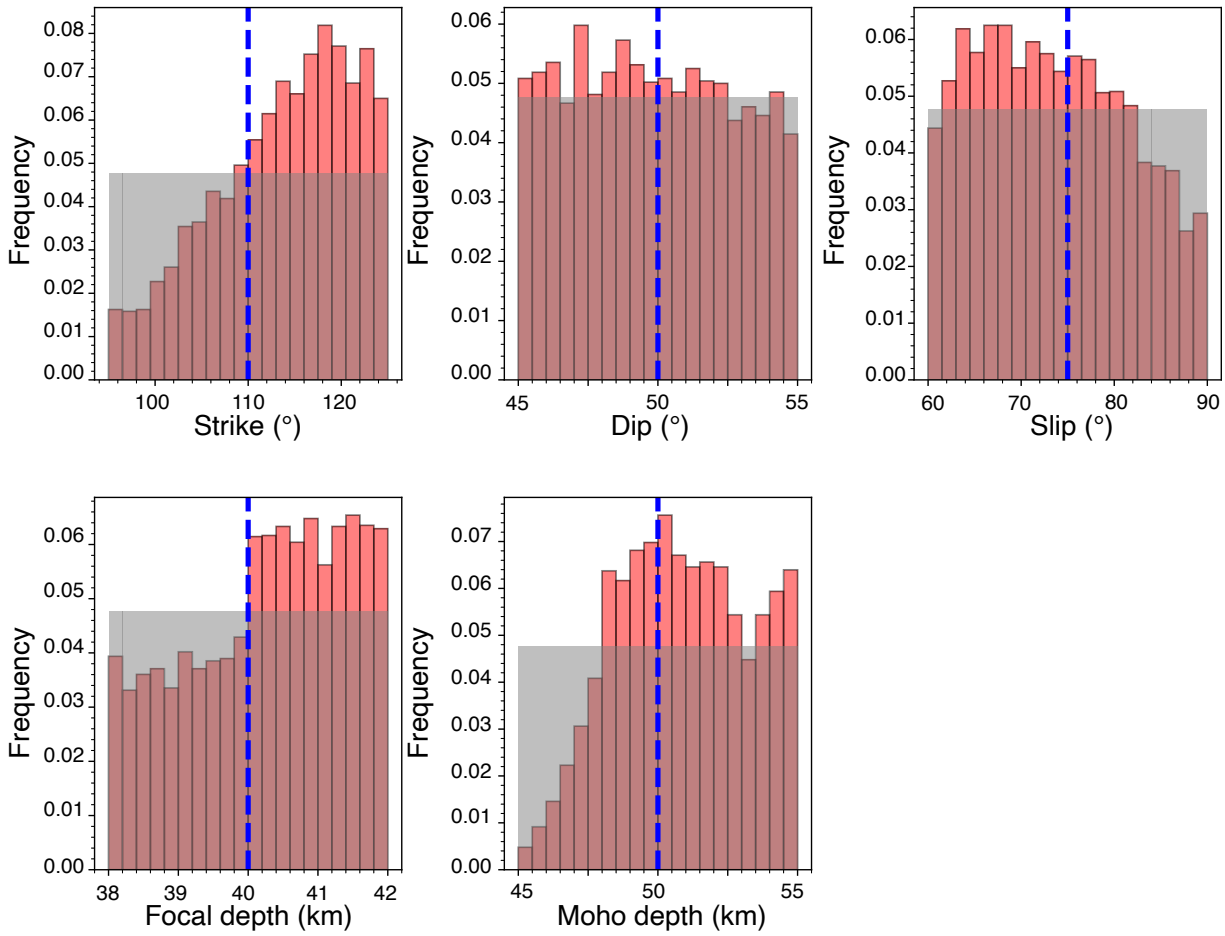

Figure 4.16: Similar as Fig. 4.6 but is for the synthetic test. (Red) The posterior distributions of strike, dip, slip, focal depth as well as Moho depth. The prior distributions used for each of those parameters are represented by the shaded grey areas. The true values used to generate the synthetic waveform are shown by the blue dashed lines.

4.5 Conclusions

In this chapter, we presented a method to invert multi-mode surface-wave waveforms and measure dispersion curves based on a single station-event pair. While surface waves have not yet been observed with InSight, this method and the modifications we brought to the original technique will be important for all future seismological exploration of other planetary bodies. We showed the feasibility of our method using the MSS blind data set in the first example, and our own synthetic data in a second example. We modified our original algorithm to help account for the large uncertainties in the source parameters as well as the lack of a good Martian reference model. Source parameters were included in the inversion together with the parameters describing the velocity profile in order to reduce the risk of mapping errors in the source into the models. We also added constraints from the waveform envelope to prevent cycle skipping. We showed tests for different reference models and we also compared the use of group velocities instead of envelopes.

Because the higher modes were not visible on the blind data, only the fundamental mode Rayleigh waves were inverted. We found that including the waveform envelope or group velocities did not affect the results strongly and both are good choices to prevent cycle skipping. Neither method was able to determine which reference model led to the recovery of the input 1-D base model as strong trade-offs between Moho depth and velocity structure exist. As long as the reference model has a Moho depth that is not too far from the true value, our method could find a suite of velocity models that included the true model and could measure phase velocities such that their error bars included the predictions from the true 1-D model. However, the inversions with reference Moho depths that were off the true value yielded apparent features in the V_S models that could be erroneously interpreted if care is not taken. This highlights how essential it will be of having good prior constraints on the Moho depth before inverting surface-wave waveforms to constrain velocity structure on Mars.

In our second example, we applied the same method to synthetic data showing higher modes in the period range 25s - 50s and that included realistic Martian noise levels. The higher mode wave trains in our test waveform was visible in the time domain, but very noisy. Nevertheless, by including higher modes in the inversion we were able to recover the V_S structure well down to 400 km depth at true average Martian noise level, despite the low SNR in the synthetic waveform. We further obtained the phase velocity dispersion curves for multiple modes and implemented a reliability analysis to assess which were confidently measured. Phase velocities at periods with high reliability scores generally fit the true phase velocities well. This demonstrates the feasibility of our method on higher modes measurements, though we want to stress the importance of having a good reference interior model to obtain reliable interior models with our waveform modeling approach.

CHAPTER 5

Summary and Conclusion

In this work, we proposed a novel transdimensional MCMC approach to invert for 1-D path-averaged structure and the corresponding dispersion curves with both fundamental and higher modes Rayleigh waves. A conventional surface wave inversion typically includes three stages [e.g. Yoshizawa and Kennett, 2002; Visser, 2008]: obtaining phase velocity measurements, combining them into phase velocity maps and finally an inversion to obtain a 3-D shear velocity model. Since our method can constrain posterior distributions of 1-D V_S models between station and source directly, we employed a two-stage approach instead: after obtaining 1-D path-averaged V_S profiles, we combined and inverted them to obtain a 3-D V_S model. One major advantage of the two-stage approach is that it requires one fewer linearized inversion and thus suffers less from the information loss and the bias-variance trade-offs during the inversions from the raw data to the final 3-D model.

In Chapter 2, we introduced the rj-MCMC technique to solve the nonlinear problem of measuring fundamental and higher mode Rayleigh wave phase velocity dispersion using waveform modeling. The posterior distribution of the 1-D V_S profiles can also be obtained in the MCMC sampling step. The use of higher mode surface waves in seismic tomography is very valuable as it increases the vertical resolution of tomographic models in the upper mantle and transition zone. The synthetic seismograms are generated with a linearized approximation in order to achieve faster computational convergence. The amplitudes of perturbation relative to the reference model are thus somewhat limited to reduce the errors introduced by such approximations. The rj-MCMC method used here has the following

advantages over linearized inversion techniques:

1. It offers a more comprehensive description of the model space by providing an ensemble of solutions which represent the posterior distributions of model parameters. The common non-uniqueness issue of the inverse problem can be better handled this way.

2. It also offers a convenient way to accurately assess the uncertainties of each model parameter. The uncertainty information is important when we use the 1-D profiles in latter stages of the inversion, and when we interpret the results.

3. The algorithm can decide how much data noise is needed to fit the data without overfitting them. The posterior noise distributions can also be used as an indicator of the quality of the waveform fit within each frequency-time window.

In the case of phase velocity measurements, we also propose a reliability analysis following Yoshizawa and Kennett [2002] to assess which higher modes were reliably separated. The effectiveness of our method was demonstrated with both a synthetic test and real data tests.

In Chapter 3, we applied the proposed method to Antarctica and obtained a 3-D azimuthally anisotropic V_S model together with multi-mode phase velocity maps. Those phase velocity maps can be used as the input for the third step of the aforementioned three-stage surface wave tomography. It is also possible to combine the phase velocity maps with other types of seismic observations, such as receiver functions or ambient noise measurements, to better constrain the shallower depths. The inversion of phase velocity maps will be discussed in future work. In this work we focused on the interpretation of the 3-D V_S model. Major conclusions from this 3-D anisotropic V_S model for Antarctica include:

1. The 2Ψ anisotropy terms are determined to be significant only in the upper 300 km.

2. EANT is associated with positive V_S anomalies in the upper 150 - 250 km, while WANT is underlain by negative V_S anomalies in the upper $\sim$200 km. Both observations are consistent with previous regional studies in Antarctica.

3. The integrated azimuthal anisotropy results from the 3-D model show good agreement with SKS splitting results in WANT. While the SKS splitting results don't match the APMs in WANT, around MBL we observe good alignments between fast axes of azimuthal anisotropy and APMs in our 3-D model at depths near LAB.

4. The fast axes in EANT start to align well with APM at about 100 km, which is rather shallow compared to the deep LAB depth of the craton. We argue that the change of fast axes takes place in the lithosphere rather than around the LAB, which may indicate the existence of a second layer in the lithosphere of the EANT craton.

In Chapter 4, we further discussed the feasibility of applying the proposed method to Mars, by taking advantage of the newly available seismic data on Mars from the Insight Mission. We first discussed the challenges stemming from using a single station to characterize both structure and the source and from the absence of a Mars reference model. We then updated our MCMC sampling algorithm by: (1) including source parameters as free parameters, (2) including the crust-mantle boundary as another free parameter, (3) increasing the V_S searching range to [-10%, +10%] relative to the reference model, and (4) adding constraints from the waveform envelope or group velocities to prevent cycle skipping. These changes were made in order to better account for the large uncertainties in the source parameters and Mars structure. Because surface waves have not yet been observed with InSight, we instead tested our method with two different synthetic dataset. For the first test we used the Mars Structure Service blind test data, for which higher modes were not visible. We thus only inverted the fundamental mode Rayleigh waves. We found strong trade-offs between the Moho depth and the velocity structure: if the reference Moho depth is far away from the true value, our method may still fit the data well, but then the resulting 1-D V_S profiles and the dispersion measurements will be off the true values. In the second test, we generated our own synthetic data with both fundamental mode and higher modes visible, and then added noises to the synthetic data by using the realistic noise levels collected from Mars. Although the higher modes segments are very noisy, we were still able to recover the V_S structure well

down to 400 km. Phase velocities at periods with high reliability scores generally fit the true phase velocities well, especially after we considered the estimated uncertainties from MCMC sampling. The tests we made with Mars will also be important for all future seismological exploration of other planetary bodies.

Bibliography

Abt, D. L., Fischer, K. M., French, S. W., Ford, H. A., Yuan, H., and Romanowicz, B. (2010). North american lithospheric discontinuity structure imaged by ps and sp receiver functions. *Journal of Geophysical Research: Solid Earth*, 115(B9).

Accardo, N. J., Wiens, D. A., Hernandez, S., Aster, R. C., Nyblade, A., Huerta, A., Anandakrishnan, S., Wilson, T., Heeszel, D. S., and Dalziel, I. W. (2014). Upper mantle seismic anisotropy beneath the west antarctic rift system and surrounding region from shear wave splitting analysis. *Geophysical Journal International*, 198(1):414–429.

Alex Brisbourne, G. S. (2016). Ukanet: Uk antarctic network.

An, M., Wiens, D. A., Zhao, Y., Feng, M., Nyblade, A., Kanao, M., Li, Y., Maggi, A., and Lévêque, J.-J. (2015a). Temperature, lithosphere-asthenosphere boundary, and heat flux beneath the antarctic plate inferred from seismic velocities. *Journal of Geophysical Research: Solid Earth*, 120(12):8720–8742.

An, M., Wiens, D. A., Zhao, Y., Feng, M., Nyblade, A. A., Kanao, M., Li, Y., Maggi, A., and Lévêque, J.-J. (2015b). S-velocity model and inferred moho topography beneath the antarctic plate from rayleigh waves. *Journal of Geophysical Research: Solid Earth*, 120(1):359–383.

Anderson, D. L. (1962). Love Wave Dispersion in Heterogeneous Anisotropic Media. *Geophysics*, 27:445–454.

Anderson, J. B. (1999). *Antarctic marine geology*. Cambridge University Press.

Anderson, O. L., Schreiber, E., Liebermann, R. C., and Soga, N. (1968). Some elastic constant data on minerals relevant to geophysics. *Reviews of Geophysics*, 6(4):491–524.

Auer, L., Boschi, L., Becker, T. W., Nissen-Meyer, T., and Giardini, D. (2014). Savani: A variable resolution whole-mantle model of anisotropic shear velocity variations based on multiple data sets. *Journal of Geophysical Research: Solid Earth*, 119(4):3006 – 3034.

Backus, G. E. (1988). Bayesian inference in geomagnetism. *Geophysical Journal International*, 92(1):125–142.

Banerdt, W. B., Smrekar, S. E., Banfield, D., Giardini, D., Golombek, M., Johnson, C. L., Lognonné, P., Spiga, A., Spohn, T., Perrin, C., Stähler, S. C., Antonangeli, D., Asmar, S., Beghein, C., Bowles, N., Bozdag, E., Chi, P., Christensen, U., Clinton, J., Collins, G. S., Daubar, I., Dehant, V., Drilleau, M., Fillingim, M., Folkner, W., Garcia, R. F., Garvin, J., Grant, J., Grott, M., Grygorczuk, J., Hudson, T., Irving, J. C. E., Kargl, G., Kawamura, T., Kedar, S., King, S., Knapmeyer-Endrun, B., Knapmeyer, M., Lemmon, M., Lorenz, R., Maki, J. N., Margerin, L., McLennan, S. M., Michaut, C., Mimoun, D., Mittelholz, A., Mocquet, A., Morgan, P., Mueller, N. T., Murdoch, N., Nagihara, S., Newman, C., Nimmo, F., Panning, M., Pike, W. T., Plesa, A.-C., Rodriguez, S., Rodriguez-Manfredi, J. A., Russell, C. T., Schmerr, N., Siegler, M., Stanley, S., Stutzmann, E., Teanby, N., Tromp, J., Driel, M. v., Warner, N., Weber, R., and Wieczorek, M. (2020). Initial results from the InSight mission on Mars. *Nature Geoscience*, pages 1–7.

Barklage, M., Wiens, D. A., Nyblade, A., and Anandakrishnan, S. (2009). Upper mantle seismic anisotropy of south victoria land and the ross sea coast, antarctica from sks and skks splitting analysis. *Geophysical Journal International*, 178(2):729–741.

Barruol, G. and Hoffmann, R. (1999). Upper mantle anisotropy beneath the geoscope stations. *Journal of Geophysical Research: Solid Earth*, 104(B5):10757–10773.

Bartzsch, S., Lebedev, S., and Meier, T. (2011). Resolving the lithosphere–asthenosphere boundary with seismic rayleigh waves. *Geophysical Journal International*, 186(3):1152–1164.

Bayer, B., Müller, C., Eaton, D. W., and Jokat, W. (2007). Seismic anisotropy beneath dronning maud land, antarctica, revealed by shear wave splitting. *Geophysical Journal International*, 171(1):339–351.

Bayes, T. and Price, n. (1763). Lii. an essay towards solving a problem in the doctrine of chances. by the late rev. mr. bayes, f. r. s. communicated by mr. price, in a letter to john canton, a. m. f. r. s. *Philosophical Transactions of the Royal Society of London*, 53:370–418.

Becker, T. W., Kellogg, J. B., Ekström, G., and O'Connell, R. J. (2003). Comparison of azimuthal seismic anisotropy from surface waves and finite strain from global mantle-circulation models. *Geophysical Journal International*, 155(2):696 – 714.

Beghein, C. (2010). Radial anisotropy and prior petrological constraints: A comparative study. *Journal of Geophysical Research*, 115(B03303).

Beghein, C., Resovsky, J., and van der Hilst, R. D. (2008). The signal of mantle anisotropy in the coupling of normal modes. *Geophysical Journal of the Royal Astronomical Society*, 175(3):1209 – 1234.

Beghein, C. and Trampert, J. (2006). Radial anisotropy in seismic reference models of the mantle. *Journal of Geophysical Research*, 111(B02303).

Beghein, C., Yuan, K., Xing, Z., and Schmerr, N. (2014). Changes in Seismic Anisotropy Shed Light on the Nature of the Gutenberg Discontinuity. *Science*, 343(6176):1237 – 1240.

Beucler, E., Stutzmann, E., and Montagner, J.-P. (2003). Surface wave higher-mode phase velocity measurements using a roller-coaster-type algorithm. *Geophysical Journal International*, 155(1):289–307.

Bevington, P. R., Robinson, D. K., Blair, J. M., Mallinckrodt, A. J., and McKay, S. (1993). Data reduction and error analysis for the physical sciences. *Computers in Physics*, 7(4):415–416.

Bodin, T. and Sambridge, M. (2009). Seismic tomography with the reversible jump algorithm. *Geophysical Journal International*, 178(3):1411–1436.

Bodin, T., Sambridge, M., Tkalčić, H., Arroucau, P., Gallagher, K., and Rawlinson, N. (2012). Transdimensional inversion of receiver functions and surface wave dispersion. *Journal of Geophysical Research: Solid Earth*, 117(B2).

Böse, M., Clinton, J., Ceylan, S., Euchner, F., Driel, M. v., Khan, A., Giardini, D., Lognonné, P., and Banerdt, W. (2017). A probabilistic framework for single-station location of seismicity on Earth and Mars. *Physics of the Earth and Planetary Interiors*, 262:48–65.

Cara, M. (1973). Filtering of dispersed wavetrains. *Geophysical Journal International*, 33(1):65–80.

Cara, M. (1978). Regional variations of higher rayleigh-mode phase velocities: a spatial-filtering method. *Geophysical Journal International*, 54(2):439–460.

Cara, M. (1979). Lateral variations of s velocity in the upper mantle from higher rayleigh modes. *Geophysical Journal International*, 57(3):649–670.

Cara, M. and Lévêque, J. (1987). Waveform inversion using secondary observables. *Geophysical Research Letters*, 14(10):1046–1049.

Chevrot, S. and Zhao, L. (2007). Multiscale finite-frequency rayleigh wave tomography of the kaapvaal craton. *Geophysical Journal International*, 169(1):201–215.

Crampin, S. (1964). Higher modes of seismic surface waves: preliminary observations. *Geophysical Journal International*, 9(1):37–57.

Dahlen, F. (1968). The Normal Modes of a Rotating, Elliptical Earth. *Geophysical Journal of the Royal Astronomical Society*, 16(4):329 – 367.

Dahlen, F. and Tromp, J. (2021). *Theoretical global seismology*. Princeton university press.

Dalziel, I. W. (1992). Antarctica; a tale of two supercontinents? *Annual Review of Earth and Planetary Sciences*, 20(1):501–526.

Danesi, S. and Morelli, A. (2001). Structure of the upper mantle under the antarctic plate from surface wave tomography. *Geophysical Research Letters*, 28(23):4395–4398.

Debayle, E. (1999). Sv-wave azimuthal anisotropy in the australian upper mantle: preliminary results from automated rayleigh waveform inversion. *Geophysical Journal International*, 137(3):747–754.

Debayle, E., Dubuffet, F., and Durand, S. (2016). An automatically updated s-wave model of the upper mantle and the depth extent of azimuthal anisotropy. *Geophysical Research Letters*, 43(2):674–682.

Debayle, E. and Ricard, Y. (2013). Seismic observations of large-scale deformation at the bottom of fast-moving plates. *Earth and Planetary Science Letters*, 376:165–177.

Deschamps, F., Lebedev, S., Meier, T., and Trampert, J. (2008). Azimuthal anisotropy of Rayleigh-wave phase velocities in the east-central United States. *Geophysical Journal International*, 173(3):827–843.

Dewart, G. and Toksöz, M. N. (1965). Crustal structure in east antarctica from surface wave dispersion. *Geophysical Journal International*, 10(2):127–139.

Drilleau, M., Beucler, E., Lognonné, P., Panning, M., Knapmeyer-Endrun, Banerdt, W., Beghein, C., Ceylan, S., van Driel, M., Joshi, R., Kawamura, T., Khan, A., Menina, S., Rivoldini, A., Samuel, H., Stähler, S., Xu, H., Bonnin, M., Clinton, J., Giardini, D., Kenda, B., Lekic, V., Mocquet, A., Murdoch, N., Schimmel, M., Smrekar, S., Stutzmann, E., Tauzin, B., and Tharimena, S. (2020). Mss/1: single-station and single-event marsquake inversion. *Journal of Geophysical Research - Earth and Space Science*.

Dziewonski, A., Bloch, S., and Landisman, M. (1969). A technique for the analysis of transient seismic signals. *Bulletin of the seismological Society of America*, 59(1):427–444.

Dziewonski, A. M. and Anderson, D. L. (1981). Preliminary reference earth model. *Physics of the earth and planetary interiors*, 25(4):297–356.

Dziewonski, A. M., Chou, T.-A., and Woodhouse, J. H. (1981). Determination of earthquake source parameters from waveform data for studies of global and regional seismicity. *Journal of Geophysical Research: Solid Earth*, 86(B4):2825–2852.

Ekström, G. and Dziewonski, A. M. (1998). The unique anisotropy of the Pacific upper mantle. *Nature*, 394:168 – 172.

Ekström, G., Nettles, M., and Dziewoński, A. M. (2012). The global CMT project 2004–2010: Centroid-moment tensors for 13,017 earthquakes. *Physics of the Earth and Planetary Interiors*, 200-201:1–9.

Emry, E., Nyblade, A. A., Julià, J., Anandakrishnan, S., Aster, R., Wiens, D. A., Huerta, A. D., and Wilson, T. J. (2015). The mantle transition zone beneath w est a ntarctica: Seismic evidence for hydration and thermal upwellings. *Geochemistry, Geophysics, Geosystems*, 16(1):40–58.

Evison, F., Ingham, C., Orr, R., and le Fort, J. (1960). Thickness of the earth's crust in antarctica and the surrounding oceans. *Geophys. J.R. Astron. Soc.*, 3(3):289–306.

Ferreira, A. M., Faccenda, M., Sturgeon, W., Chang, S.-J., and Schardong, L. (2019). Ubiquitous lower-mantle anisotropy beneath subduction zones. *Nature Geoscience*, pages 1 – 8.

Ford, H. A., Long, M. D., and Wirth, E. A. (2016). Midlithospheric discontinuities and complex anisotropic layering in the mantle lithosphere beneath the Wyoming and Superior Provinces. *Journal of Geophysical Research: Solid Earth*, 121(9):6675–6697.

Fouch, M. J. and Fischer, K. M. (1996). Mantle anisotropy beneath northwest Pacific subduction zones. *Journal of Geophysical Research: Solid Earth*, 101(B7):15987.

Geyer, C. J. and Møller, J. (1994). Simulation procedures and likelihood inference for spatial point processes. *Scandinavian Journal of Statistics*, 21(4):359–373.

Giardini, D., Lognonné, P., Banerdt, W. B., Pike, W. T., Christensen, U., Ceylan, S., Clinton, J. F., van Driel, M., Stähler, S. C., Böse, M., Garcia, R. F., Khan, A., Panning, M., Perrin, C., Banfield, D., Beucler, E., Charalambous, C., Euchner, F., Horleston, A., Jacob, A., Kawamura, T., Kedar, S., Mainsant, G., Scholz, J.-R., Smrekar, S. E., Spiga, A., Agard, C., Antonangeli, D., Barkaoui, S., Barrett, E., Combes, P., Conejero, V., Daubar, I., Drilleau, M., Ferrier, C., Gabsi, T., Gudkova, T., Hurst, K., Karakostas, F., King, S., Knapmeyer, M., Knapmeyer-Endrun, B., Llorca-Cejudo, R., Lucas, A., Luno, L., Margerin, L., McClean, J. B., Mimoun, D., Murdoch, N., Nimmo, F., Nonon, M., Pardo, C., Rivoldini, A., Manfredi, J. A. R., Samuel, H., Schimmel, M., Stott, A. E., Stutzmann, E., Teanby, N., Warren, T., Weber, R. C., Wieczorek, M., and Yana, C. (2020). The seismicity of Mars. *Nature Geoscience*, 13(3):205–212.

Granot, R., Cande, S., Stock, J., Davey, F., and Clayton, R. (2010). Postspreading rifting in the adare basin, antarctica: regional tectonic consequences. *Geochemistry, Geophysics, Geosystems*, 11(8).

Gripp, A. E. and Gordon, R. G. (2002). Young tracks of hotspots and current plate velocities. *Geophysical Journal International*, 150(2):321–361.

Gudkova, T. and Zharkov, V. (2004). Mars: Interior structure and excitation of free oscillations. *Physics of the Earth and Planetary Interiors*, 142:1–22.

Gung, Y., Panning, M. P., and Romanowicz, B. (2003). Global anisotropy and the thickness of continents. *Nature*, 422(6933):707 – 711.

Hansen, P. C. (1998). *Rank-deficient and discrete ill-posed problems: numerical aspects of linear inversion*. SIAM.

Hansen, S. (2012). Transantarctic mountains northern network.

Hansen, S. E., Graw, J. H., Kenyon, L. M., Nyblade, A. A., Wiens, D. A., Aster, R. C., Huerta, A. D., Anandakrishnan, S., and Wilson, T. (2014). Imaging the antarctic mantle using adaptively parameterized p-wave tomography: Evidence for heterogeneous structure beneath west antarctica. *Earth and Planetary Science Letters*, 408:66–78.

Hansen, S. E., Julia, J., Nyblade, A. A., Pyle, M. L., Wiens, D. A., and Anandakrishnan, S. (2009). Using s wave receiver functions to estimate crustal structure beneath ice sheets: An application to the transantarctic mountains and east antarctic craton. *Geochemistry, Geophysics, Geosystems*, 10(8).

Hansen, S. E., Nyblade, A. A., Heeszel, D. S., Wiens, D. A., Shore, P., and Kanao, M. (2010). Crustal structure of the gamburtsev mountains, east antarctica, from s-wave receiver functions and rayleigh wave phase velocities. *Earth and Planetary Science Letters*, 300(3-4):395–401.

Heeszel, D. S., Wiens, D. A., Anandakrishnan, S., Aster, R. C., Dalziel, I. W., Huerta, A. D., Nyblade, A. A., Wilson, T. J., and Winberry, J. P. (2016). Upper mantle structure of central and west antarctica from array analysis of rayleigh wave phase velocities. *Journal of Geophysical Research: Solid Earth*, 121(3):1758–1775.

Heeszel, D. S., Wiens, D. A., Nyblade, A. A., Hansen, S. E., Kanao, M., An, M., and Zhao, Y. (2013). Rayleigh wave constraints on the structure and tectonic history of the gamburtsev subglacial mountains, east antarctica. *Journal of Geophysical Research: Solid Earth*, 118(5):2138–2153.

Hernandez, S., Wiens, D., Anandakrishnan, S., Aster, R., Huerta, A., Nyblade, A., and Wilson, T. (2009). Seismic anisotropy of the antarctic upper mantle from shear wave

splitting analysis of polenet and agap seismograms. In *AGU Fall Meeting Abstracts*, volume 2009, pages U51C–0043.

Huang, Q., Schmerr, N., Waszek, L., and Beghein, C. (2019). Constraints on Seismic Anisotropy in the Mantle Transition Zone From Long-Period SS Precursors. *Journal of Geophysical Research Solid Earth*, 124(7):6779–6800.

Jeans, J. H. (1923). The propagation of earthquake waves. *Proceedings of the Royal Society of London. Series A, Containing Papers of a Mathematical and Physical Character*, 102(718):554–574.

Karato, S.-i., Jung, H., Katayama, I., Skemer, P., and Skemer, P. (2008). Geodynamic Significance of Seismic Anisotropy of the Upper Mantle: New Insights from Laboratory Studies. *Annual Review of Earth and Planetary Sciences*, 36(1):59 – 95.

Karato, S.-i. and Wu, P. (1993). Rheology of the Upper Mantle - a Synthesis. *Science*, 260(5109):771 – 778.

Kovach, R. and Press, F. (1961). Surface wave dispersion and crustal structure in antarctica and the surrounding oceans. *Annals of Geophysics*, 14:211–224.

Laske, G., Masters, G., Ma, Z., and Pasyanos, M. (2013). Update on crust1. 0—a 1-degree global model of earth's crust. In *Geophys. res. abstr*, volume 15, page 2658.

Laske, G. and Widmer-Schnidrig, R. (2015). 1.04 - theory and observations: Normal mode and surface wave observations. In Schubert, G., editor, *Treatise on Geophysics (Second Edition)*, pages 117–167. Elsevier, Oxford, second edition edition.

Lebedev, S., Boonen, J., and Trampert, J. (2009). Seismic structure of precambrian lithosphere: new constraints from broad-band surface-wave dispersion. *Lithos*, 109(1-2):96–111.

Lebedev, S., Meier, T., Deschamps, F., and Trampert, J. (2008). Stratified seismic anisotropy reveals past and present deformation beneath the East-central United States. *Earth and Planetary Science Letters*, 274(3-4):489 – 498.

Lebedev, S. and Nolet, G. (2003). Upper mantle beneath southeast asia from s velocity tomography. *Journal of Geophysical Research: Solid Earth*, 108(B1).

Lebedev, S., Nolet, G., Meier, T., and Van Der Hilst, R. D. (2005). Automated multimode inversion of surface and s waveforms. *Geophysical Journal International*, 162(3):951–964.

Lerner-Lam, A. L. and Jordan, T. H. (1983). Earth structure from fundamental and higher-mode waveform analysis. *Geophysical Journal International*, 75(3):759–797.

Li, X.-D. and Romanowicz, B. (1995). Comparison of global waveform inversions with and without considering cross-branch modal coupling. *Geophysical Journal International*, 121(3):695–709.

Li, X.-D. and Romanowicz, B. (1996). Global mantle shear velocity model developed using nonlinear asymptotic coupling theory. *Journal of Geophysical Research: Solid Earth*, 101(B10):22245–22272.

Lloyd, A., Wiens, D., Zhu, H., Tromp, J., Nyblade, A., Aster, R., Hansen, S., Dalziel, I., Wilson, T., Ivins, E., et al. (2020). Seismic structure of the antarctic upper mantle imaged with adjoint tomography. *Journal of Geophysical Research: Solid Earth*, 125(3).

Lloyd, A. J., Wiens, D. A., Nyblade, A. A., Anandakrishnan, S., Aster, R. C., Huerta, A. D., Wilson, T. J., Dalziel, I. W., Shore, P. J., and Zhao, D. (2015). A seismic transect across west antarctica: Evidence for mantle thermal anomalies beneath the bentley subglacial trench and the marie byrd land dome. *Journal of Geophysical Research: Solid Earth*, 120(12):8439–8460.

Lognonné, P., Banerdt, W., Pike, W., Giardini, D., Christensen, U., Garcia, R., Kawamura, T., Kedar, S., Knapmeyer-Endrun, B., Margerin, L., Nimmo, F., Panning, M., Tauzin, B., Scholz, J.-R., Antonangeli, D., Barkaoui, S., Beucler, E., Bissig, F., Brinkman, N., Calvet, M., Ceylan, S., Charalambous, C., Davis, P., Driel, M. v., Drilleau, M., Fayon, L., Joshi, R., Kenda, B., Khan, A., Knapmeyer, M., Lekic, V., McClean, J., Mimoun, D., Murdoch, N., Pan, L., Perrin, C., Pinot, B., Pou, L., Menina, S., Rodriguez, S., Schmelzbach, C., Schmerr, N., Sollberger, D., Spiga, A., Stähler, S., Stott, A., Stutzmann, E., Tharimena, S., Widmer-Schnidrig, R., Andersson, F., Ansan, V., Beghein, C., Böse, M., Bozdag, E., Clinton, J., Daubar, I., Delage, P., Fuji, N., Golombek, M., Grott, M., Horleston, A., Hurst, K., Irving, J., Jacob, A., Knollenberg, J., Krasner, S., Krause, C., Lorenz, R., Michaut, C., Myhill, R., Nissen-Meyer, T., Pierick, J., Plesa, A.-C., Quantin-Nataf, C., Robertsson, J., Rochas, L., Schimmel, M., Smrekar, S., Spohn, T., Teanby, N., Tromp, J., Vallade, J., Verdier, N., Vrettos, C., Weber, R., Banfield, D., Barrett, E., Bierwirth, M., Calcutt, S., Compaire, N., Johnson, C., Mance, D., Euchner, F., Kerjean, L., Mainsant, G., Mocquet, A., Rodriguez Manfredi, J., Pont, G., Laudet, P., Nebut, T., de Raucourt, S., Robert, O., Russell, C., Sylvestre-Baron, A., Tillier, S., Warren, T., Wieczorek, M., Yana, C., and Zweifel, P. (2020). Constraints on the shallow elastic and anelastic structure of Mars from InSight seismic data. *Nature Geoscience*.

Lognonné, P., Banerdt, W. B., Giardini, D., Pike, W. T., Christensen, U., Laudet, P., de Raucourt, S., Zweifel, P., Calcutt, S., Bierwirth, M., Hurst, K. J., Ijpelaan, F., Umland, J. W., Llorca-Cejudo, R., Larson, S. A., Garcia, R. F., Kedar, S., Knapmeyer-Endrun, B., Mimoun, D., Mocquet, A., Panning, M. P., Weber, R. C., Sylvestre-Baron, A., Pont, G., Verdier, N., Kerjean, L., Facto, L. J., Gharakanian, V., Feldman, J. E., Hoffman, T. L., Klein, D. B., Klein, K., Onufer, N. P., Paredes-Garcia, J., Petkov, M. P., Willis, J. R., Smrekar, S. E., Drilleau, M., Gabsi, T., Nebut, T., Robert, O., Tillier, S., Moreau, C., Parise, M., Aveni, G., Ben Charef, S., Bennour, Y., Camus, T., Dandonneau, P. A., Desfoux, C., Lecomte, B., Pot, O., Revuz, P., Mance, D., tenPierick, J., Bowles, N. E.,

Charalambous, C., Delahunty, A. K., Hurley, J., Irshad, R., Liu, H., Mukherjee, A. G., Standley, I. M., Stott, A. E., Temple, J., Warren, T., Eberhardt, M., Kramer, A., Kühne, W., Miettinen, E.-P., Monecke, M., Aicardi, C., André, M., Baroukh, J., Borrien, A., Bouisset, A., Boutte, P., Brethomé, K., Brysbaert, C., Carlier, T., Deleuze, M., Desmarres, J. M., Dilhan, D., Doucet, C., Faye, D., Faye-Refalo, N., Gonzalez, R., Imbert, C., Larigauderie, C., Locatelli, E., Luno, L., Meyer, J.-R., Mialhe, F., Mouret, J. M., Nonon, M., Pahn, Y., Paillet, A., Pasquier, P., Perez, G., Perez, R., Perrin, L., Pouilloux, B., Rosak, A., Savin de Larclause, I., Sicre, J., Sodki, M., Toulemont, N., Vella, B., Yana, C., Alibay, F., Avalos, O. M., Balzer, M. A., Bhandari, P., Blanco, E., Bone, B. D., Bousman, J. C., Bruneau, P., Calef, F. J., Calvet, R. J., D'Agostino, S. A., de los Santos, G., Deen, R. G., Denise, R. W., Ervin, J., Ferraro, N. W., Gengl, H. E., Grinblat, F., Hernandez, D., Hetzel, M., Johnson, M. E., Khachikyan, L., Lin, J. Y., Madzunkov, S. M., Marshall, S. L., Mikellides, I. G., Miller, E. A., Raff, W., Singer, J. E., Sunday, C. M., Villalvazo, J. F., Wallace, M. C., Banfield, D., Rodriguez-Manfredi, J. A., Russell, C. T., Trebi-Ollennu, A., Maki, J. N., Beucler, E., Böse, M., Bonjour, C., Berenguer, J. L., Ceylan, S., Clinton, J., Conejero, V., Daubar, I., Dehant, V., Delage, P., Euchner, F., Estève, I., Fayon, L., Ferraioli, L., Johnson, C. L., Gagnepain-Beyneix, J., Golombek, M., Khan, A., Kawamura, T., Kenda, B., Labrot, P., Murdoch, N., Pardo, C., Perrin, C., Pou, L., Sauron, A., Savoie, D., Stähler, S., Stutzmann, E., Teanby, N. A., Tromp, J., van Driel, M., Wieczorek, M., Widmer-Schnidrig, R., and Wookey, J. (2019). SEIS: Insight's Seismic Experiment for Internal Structure of Mars. *Space Science Reviews*, 215(1).

Long, M. D. and van der Hilst, R. D. (2005). Upper mantle anisotropy beneath Japan from shear wave splitting. *Physics of the Earth and Planetary Interiors*, 151(3-4):206–222.

Lynner, C. and Long, M. D. (2015). Heterogeneous seismic anisotropy in the transition zone and uppermost lower mantle: evidence from South America, Izu-Bonin and Japan. *Geophysical Journal of the Royal Astronomical Society*, 201(3):1545 – 1552.

Lynner, C., Lynner, C., and Long, M. D. (2014). Lowermost mantle anisotropy and deformation along the boundary of the African LLSVP. *Geophysical Research Letters*, 41:3447–3454.

Maggi, A., Debayle, E., Priestley, K., and Barruol, G. (2006). Azimuthal anisotropy of the pacific region. *Earth and Planetary Science Letters*, 250(1-2):53–71.

Malinverno, A. (2002). Parsimonious Bayesian Markov Chain Monte Carlo inversion in a nonlinear geophysical problem. *Geophysical Journal of the Royal Astronomical Society*, 151(3):675–688.

Marone, F., Gung, Y., and Romanowicz, B. (2007). Three-dimensional radial anisotropic structure of the North American upper mantle from inversion of surface waveform data. *Geophysical Journal of the Royal Astronomical Society*, 171(1):206 – 222.

Masters, G., Woodhouse, J., and Freeman, G. (2011). Mineos v1.0.2 [software].

McNamara, D. E. and Buland, R. P. (2004). Ambient Noise Levels in the Continental United States. *Bulletin of the Seismological Society of America*, 94(4):1517–1527.

Meier, U., Trampert, J., and Curtis, A. (2009). Global variations of temperature and water content in the mantle transition zone from higher mode surface waves. *Earth and Planetary Science Letters*, 282(1–4):91 – 101.

Menke, W. (2018). *Geophysical data analysis: Discrete inverse theory*. Academic press.

Montagner, J.-P., Griot-Pommera, D.-A., and Lavé, J. (2000). How to relate body wave and surface wave anisotropy? *Journal of Geophysical Research: Solid Earth*, 105(B8):19015–19027.

Montagner, J.-P. and Jobert, N. (1988). Vectorial tomography ii. Application to the Indian Ocean. *Geophysical Journal of the Royal Astronomical Society*, 94(2):309–344.

Montagner, J.-P. and Nataf, H. (1986). A Simple Method for Inverting the Azimuthal Anisotropy of Surface-Waves. *Journal of Geophysical Research*, 91(B1):511 – 520.

Montagner, J. P., Romanowicz, B., and Karczewski, J.-F. (1994). A first step toward an oceanic geophysical observatory. *Eos, Transactions American Geophysical Union*, 75(13):150–154.

Moulik, P. and Ekström, G. (2014). An anisotropic shear velocity model of the Earth's mantle using normal modes, body waves, surface waves and long-period waveforms. *Geophysical Journal of the Royal Astronomical Society*, 199(3):1713 – 1738.

Müller, C. (2001). Upper mantle seismic anisotropy beneath antarctica and the scotia sea region. *Geophysical Journal International*, 147(1):105–122.

Nimmo, F. and Faul, U. H. (2013). Dissipation at tidal and seismic frequencies in a melt-free, anhydrous Mars. *Journal of Geophysical Research: Planets*, 118:2558–2569.

Nolet, G. (1975). Higher rayleigh modes in western europe. *Geophysical Research Letters*, 2(2):60–62.

Nolet, G. (1990). Partitioned waveform inversion and two-dimensional structure under the network of autonomously recording seismographs. *Journal of Geophysical Research: Solid Earth*, 95(B6):8499–8512.

O'Donnell, J., Brisbourne, A. M., Stuart, G., Dunham, C., Yang, Y., Nield, G., Whitehouse, P., Nyblade, A., Wiens, D., Anandakrishnan, S., et al. (2019). Mapping crustal shear wave velocity structure and radial anisotropy beneath west antarctica using seismic ambient noise. *Geochemistry, Geophysics, Geosystems*, 20(11):5014–5037.

Paige, C. C. and Saunders, M. A. (1982). Lsqr: An algorithm for sparse linear equations and sparse least squares. *ACM Transactions on Mathematical Software (TOMS)*, 8(1):43–71.

Panning, M. and Romanowicz, B. (2006). A three-dimensional radially anisotropic model of shear velocity in the whole mantle. *Geophysical Journal of the Royal Astronomical Society*, 167(1):361 – 379.

Panning, M. P., Beucler, É., Drilleau, M., Mocquet, A., Lognonné, P., and Banerdt, W. B. (2015). Verifying single-station seismic approaches using earth-based data: Preparation for data return from the insight mission to mars. *Icarus*, 248:230–242.

Panning, M. P., Lognonné, P., Banerdt, W. B., Garcia, R., Golombek, M. P., Kedar, S., Knapmeyer-Endrun, B., Mocquet, A., Teanby, N. A., Tromp, J., Weber, R., Beucler, E., Blanchette-Guertin, J.-F., Bozdağ, E., Drilleau, M., Gudkova, T., Hempel, S., Khan, A., Lekić, V., Murdoch, N., Plesa, A.-C., Rivoldini, A., Schmerr, N., Ruan, Y., Verhoeven, O., Gao, C., Christensen, U., Clinton, J. F., Dehant, V., Giardini, D., Mimoun, D., Pike, W. T., Smrekar, S., Wieczorek, M., Knapmeyer, M., and Wookey, J. (2017). Planned products of the Mars Structure Service for the InSight mission to Mars. *Space Science Reviews*, 211:611–650.

Pondrelli, S. and Azzara, R. (1998). Upper mantle anisotropy in victoria land (antarctica). In *Geodynamics of Lithosphere & Earth's Mantle*, pages 433–442. Springer.

Press, F. and Gilbert, D. (1959). Extent of the antarctic continent. *Science*, 129(3347):462–463.

Reading, A. M. and Heintz, M. (2008). Seismic anisotropy of east antarctica from shear-wave splitting: Spatially varying contributions from lithospheric structural fabric and mantle flow? *Earth and Planetary Science Letters*, 268(3-4):433–443.

Ritsema, J., Deuss, a. A., Van Heijst, H., and Woodhouse, J. (2011). S40rts: a degree-40 shear-velocity model for the mantle from new rayleigh wave dispersion, teleseismic traveltime and normal-mode splitting function measurements. *Geophysical Journal International*, 184(3):1223–1236.

Ritsema, J. and van Heijst, H. (2000a). New seismic model of the upper mantle beneath africa. *Geology*, 28(1):63–66.

Ritsema, J. and van Heijst, H.-J. (2000b). Seismic imaging of structural heterogeneity in earth's mantle: evidence for large-scale mantle flow. *Science Progress (1933-)*, pages 243–259.

Ritzwoller, M. H., Shapiro, N. M., Levshin, A. L., and Leahy, G. M. (2001). Crustal and upper mantle structure beneath antarctica and surrounding oceans. *Journal of Geophysical Research: Solid Earth*, 106(B12):30645–30670.

Roult, G. and Romanowicz, B. (1984). Very long-period data from the geoscope network: preliminary results on great circle averages of fundamental and higher rayleigh and love modes. *Bulletin of the Seismological Society of America*, 74(6):2221–2243.

Roult, G., Rouland, D., and Montagner, J. (1994). Antarctica ii: Upper-mantle structure from velocities and anisotropy. *Physics of the Earth and Planetary Interiors*, 84(1-4):33–57.

Sambridge, M. (1999a). Geophysical inversion with a neighbourhood algorithm—i. searching a parameter space. *Geophysical journal international*, 138(2):479–494.

Sambridge, M. (1999b). Geophysical inversion with a neighbourhood algorithm—ii. appraising the ensemble. *Geophysical Journal International*, 138(3):727–746.

Shen, W., Wiens, D. A., Anandakrishnan, S., Aster, R. C., Gerstoft, P., Bromirski, P. D., Hansen, S. E., Dalziel, I. W., Heeszel, D. S., Huerta, A. D., et al. (2018). The crust and upper mantle structure of central and west antarctica from bayesian inversion of rayleigh wave and receiver functions. *Journal of Geophysical Research: Solid Earth*, 123(9):7824–7849.

Sieminski, A., Debayle, E., and Lévêque, J.-J. (2003). Seismic evidence for deep low-velocity anomalies in the transition zone beneath west antarctica. *Earth and Planetary Science Letters*, 216(4):645–661.

Silver, P. G. (1996). Seismic anisotropy beneath the continents: Probing the depths of geology. *Annual Review of Earth and Planetary Sciences*, 24.

Silver, P. G. and Chan, W. W. (1988). Implications for continental structure and evolution from seismic anisotropy. *Nature*, 335(6185):34–39.

Smith, D. B., Ritzwoller, M. H., and Shapiro, N. M. (2004). Stratification of anisotropy in the Pacific upper mantle. *Journal of Geophysical Research*, 109(B11):243 – 22.

Smrekar, S. E., Lognonné, P., Spohn, T., Banerdt, W. B., Breuer, D., Christensen, U., Dehant, V., Drilleau, M., Folkner, W., Fuji, N., Garcia, R. F., Giardini, D., Golombek, M., Grott, M., Gudkova, T., Johnson, C., Khan, A., Langlais, B., Mittelholz, A., Mocquet, A., Myhill, R., Panning, M., Perrin, C., Pike, T., Plesa, A.-C., Rivoldini, A., Samuel, H., Stähler, S. C., Driel, M. v., Hoolst, T. V., Verhoeven, O., Weber, R., and Wieczorek, M. (2019). Pre-mission InSights on the Interior of Mars. *Space Science Reviews*, 215(1):3.

Sohl, F. and Spohn, T. (1997). The interior structure of Mars: Implications from SNC meteorites. *Journal of Geophysical Research: Planets*, 102:1613–1635.

Stähler, S. C. and Sigloch, K. (2016). Fully probabilistic seismic source inversion-part 2: modelling errors and station covariances. *Solid Earth*, 7(6):1521–1536.

Stutzmann, E. and Montagner, J.-P. (1993). An inverse technique for retrieving higher mode phase velocity and mantle structure. *Geophysical Journal International*, 113(3):669–683.

Tozer, B., Sandwell, D. T., Smith, W. H., Olson, C., Beale, J., and Wessel, P. (2019). Global bathymetry and topography at 15 arc sec: Srtm15+. *Earth and Space Science*, 6(10):1847–1864.

Trampert, J. and van Heijst, H. J. (2002). Global azimuthal anisotropy in the transition zone. *Science*, 296(5571):1297–1299.

Trampert, J. and Woodhouse, J. H. (2003). Global anisotropic phase velocity maps for fundamental mode surface waves between 40 and 150 s. *Geophysical Journal International*, 154(1):154–165.

Valentine, A. and Woodhouse, J. (2010). Reducing errors in seismic tomography: combined inversion for sources and structure. *Geophysical Journal of the Royal Astronomical Society*, 180(2):847 – 857.

Valentine, A. P. and Trampert, J. (2012). Assessing the uncertainties on seismic source parameters: Towards realistic error estimates for centroid-moment-tensor determinations. *Physics of the Earth and Planetary Interiors*, 210:36–49.

van Driel, M., Ceylan, S., Clinton, J. F., Giardini, D., Alemany, H., Allam, A., Ambrois, D., Balestra, J., Banerdt, B., Becker, D., BÃ¶se, M., Boxberg, M. S., Brinkman, N., Casademont, T., ChÃšze, J., Daubar, I., Deschamps, A., Dethof, F., Ditz, M., Drilleau, M., Essing, D., Euchner, F., Fernando, B., Garcia, R., Garth, T., Godwin, H., Golombek, M. P., Grunert, K., Hadziioannou, C., Haindl, C., Hammer, C., Hochfeld, I., Hosseini, K., Hu, H., Kedar, S., Kenda, B., Khan, A., Kilchling, T., Knapmeyer-Endrun, B., Lamert, A., Li, J., LognonnÃ©, P., Mader, S., Marten, L., Mehrkens, F., Mercerat, D., Mimoun, D., Möller, T., Murdoch, N., Neumann, P., Neurath, R., Paffrath, M., Panning, M. P., Peix, F., Perrin, L., Rolland, L., Schimmel, M., SchrÃ¶er, C., Spiga, A., Stähler, S. C., Steinmann, R., Stutzmann, E., Szenicer, A., Trumpik, N., Tsekhmistrenko, M., Twardzik, C., Weber, R., Jarklowski, P. W., Zhang, S., and Zheng, Y. (2019). Preparing for InSight: Evaluation of the Blind Test for Martian Seismicity. *Seismological Research Letters*, pages 1 – 17.

van Heijst, H. and Woodhouse, J. (1999a). Global high-resolution phase velocity distributions

of overtone and fundamental-mode surface waves determined by mode branch stripping. *Geophysical Journal International*, 137(3):601–620.

van Heijst, H. J. and Woodhouse, J. (1997a). Measuring surface-wave overtone phase velocities using a mode-branch stripping technique. *Geophysical Journal International*, 131(2):209–230.

van Heijst, H. J. and Woodhouse, J. (1997b). Measuring surface-wave overtone phase velocities using a mode-branch stripping technique. *Geophysical Journal International*, 131(2):209–230.

van Heijst, H. J. and Woodhouse, J. (1999b). Global high-resolution phase velocity distributions of overtone and fundamental-mode surface waves determined by mode branch stripping. *Geophysical Journal International*, 137(3):601–620.

Visser, K. (2008). *Monte Carlo search techniques applied to the measurement of higher mode phase velocities and anisotropic surface wave tomography. Geologica Ultraiectina (285).* Departement Aardwetenschappen. OCLC: 6893359236.

Visser, K., Lebedev, S., Trampert, J., and Kennett, B. (2007). Global Love wave overtone measurements. *Geophysical Research Letters*, 34(3).

Volk, O., White, R. S., Pilia, S., Green, R. G., Maclennan, J., and Rawlinson, N. (2021). Oceanic crustal flow in Iceland observed using seismic anisotropy. *Nature Geoscience*, 14(3):168–173.

Wiens, D. and Nyblade, A. (2007a). A broadband seismic experiment to image the lithosphere beneath the gamburtsev mountains, east antarctica.

Wiens, D. and Nyblade, A. (2007b). Ipy polenet-antarctica: Investigating links between geodynamics and ice sheets.

Woodhouse, J. (1980). The coupling and attenuation of nearly resonant multiplets in the earth's free oscillation spectrum. *Geophysical Journal of the Royal Astronomical Society*, 61(2):261 – 283.

Xu, H. and Beghein, C. (2019). Measuring higher mode surface wave dispersion using a transdimensional Bayesian approach. *Geophysical Journal International*, 218(1):333–353.

Xu, H., Beghein, C., Panning, M., Drilleau, M., Lognonné, P., van Driel, M., Ceylan, S., Böse, M., Brinkman, N., Clinton, J., et al. (2021). Measuring fundamental and higher mode surface wave dispersion on mars from seismic waveforms. *Earth and Space Science*, 8(2):e2020EA001263.

Yao, H., Beghein, C., and van der Hilst, R. D. (2008). Surface wave array tomography in SE Tibet from ambient seismic noise and two-station analysis - II. Crustal and upper-mantle structure. *Geophysical Journal of the Royal Astronomical Society*, 173(1):205 – 219.

Yoshizawa, K. (2014). Radially anisotropic 3-d shear wave structure of the australian lithosphere and asthenosphere from multi-mode surface waves. *Physics of the Earth and Planetary Interiors*, 235:33–48.

Yoshizawa, K. and Ekström, G. (2010). Automated multimode phase speed measurements for high-resolution regional-scale tomography: application to North America. *Geophysical Journal International*, 183(3):1538–1558.

Yoshizawa, K. and Kennett, B. (2002). Non-linear waveform inversion for surface waves with a neighbourhood algorithm—application to multimode dispersion measurements. *Geophysical Journal International*, 149(1):118–133.

Yoshizawa, K. and Kennett, B. (2004). Multimode surface wave tomography for the australian region using a three-stage approach incorporating finite frequency effects. *Journal of Geophysical Research: Solid Earth*, 109(B2).

Yoshizawa, K. and Kennett, B. (2015). The lithosphere-asthenosphere transition and radial anisotropy beneath the australian continent. *Geophysical research letters*, 42(10):3839–3846.

Yuan, H., French, S., Cupillard, P., and Romanowicz, B. (2014). Lithospheric expression of geological units in central and eastern north america from full waveform tomography. *Earth and Planetary Science Letters*, 402:176–186.

Yuan, H. and Romanowicz, B. (2010). Lithospheric layering in the north american craton. *Nature*, 466(7310):1063–1068.

Yuan, K. and Beghein, C. (2013). Seismic anisotropy changes across upper mantle phase transitions. *Earth and Planetary Science Letters*, 374:132–144.

Yuan, K. and Beghein, C. (2014). Three-dimensional variations in love and rayleigh wave azimuthal anisotropy for the upper 800 km of the mantle. *Journal of Geophysical Research: Solid Earth*, 119(4):3232–3255.

Zheng, Y., Nimmo, F., and Lay, T. (2015). Seismological implications of a lithospheric low seismic velocity zone in Mars. *Physics of the Earth and Planetary Interiors*, 240:132–141.